Durham E-Theses

NMR studies of some solid silver and tin compounds

Amornsakchai, Pornsawan

How to cite:

Amornsakchai, Pornsawan (2004) *NMR studies of some solid silver and tin compounds*, Durham theses, Durham University. Available at Durham E-Theses Online: http://etheses.dur.ac.uk/3163/

NMR STUDIES OF SOME SOLID SILVER AND TIN COMPOUNDS

by

Pornsawan Amornsakchai

Ustinov College

University of Durham

A thesis submitted in partial fulfilment of the requirements for the degree of

Doctor of Philosophy

Department of Chemistry

University of Durham

2004

NMR STUDIES OF SOME SOLID SILVER AND TIN COMPOUNDS

Pornsawan Amornsakchai
Submitted for the degree of Doctor of Philosophy, 2004

Abstract

A solid-state NMR study of a range of tin- and silver-containing compounds has been carried out in order to obtain information on the chemical shifts, coupling constants and relaxation times. The results are discussed in relation to the crystal structures, where known, and some crystallographic information obtained in cases with no previously-known structures.

For tin-containing compounds, solid-state ^{119}Sn and ^{31}P NMR comprise the majority of this work. Nevertheless, ^{13}C NMR studies have been also carried out to assist the structure determination. Six Sn(II) compounds have been examined, including three which also contain phosphorus. Spinning sideband analysis has been achieved for ^{119}Sn (in some cases ^{31}P), giving information on the shielding tensors. Satellite peaks observed on the ^{119}Sn NMR spectra of $SnHPO_3$ and $SnHPO_4$ reveal that the spectra contain information about indirect Sn,Sn coupling. Since surprisingly large values of 2600 ± 200 Hz and 4150 ± 200 Hz are found for $SnHPO_3$ and $SnHPO_4$, respectively, the calculated relative intensities of the satellites and the results of a single Hahn echo experiment have been discussed in detail.

The relatively isolated $(^1H, ^{31}P)$ spin pair in solid $SnHPO_3$ have been extensively investigated in this work, though the systems are rather complicated. The ^1H and ^{31}P spectra display an intensity distribution of the spinning sidebands, which is the characteristic of an interplay of shielding, dipolar and indirect coupling tensors dominated, by the strong dipolar interactions. A single Hahn echo experiment was employed to reveal indirect spin-spin coupling $(^1J_{PH})$. Strong oscillatory polarization transfer by dipolar interaction occurs during short contact times on moderately fast magic-angle spinning and the P,H distances were extracted (including for $SnHPO_4$). Rather complicated ^1H NMR spectra under ^{31}P continuous-wave decoupling arises from a second-order recoupling of the heteronuclear dipolar-coupling tensor and the shielding tensor of ^{31}P, leading to line-splittings and broadenings in the $\{^{31}P\}^1H$ spectra. Additionally, measurement of ^1H and ^{31}P relaxation times has been undertaken, producing results which were expected to follow the behaviour characteristic of an isolated two-spin system, but anomalies were observed.

Various nuclei, such as ^{13}C, ^{15}N, ^{31}P and ^{109}Ag, in silver-containing compounds have been studied, and provide information on indirect spin-spin interactions, $^1J(^{109}Ag^{14}N)$ and $^1J(^{109}Ag^{15}N)$. The ^{109}Ag NMR spectra for $[Ag(NH_3)_2]_2X$ where X = SO_4, SeO_4, NO_3 show spinning sideband manifolds, which are typical for systems with moderately large shielding anisotropy. Other silver compounds namely $[Ag(R)_2]NO_3$ where R = pyridine, collidine, 2-picoline, quinoline and AgY where Y = HPO_4 and PO_4, have been investigated to give as much complementary information about the chemical shifts as possible.

Memorandum

The research presented in this thesis has been carried out at the Department of Chemistry of the University of Durham between March 2001 and March 2004. It is the original work of the author unless otherwise stated. None of this work has been submitted for any other degree.

Acknowledgements

To mum and dad

Abbreviations, symbols and notation

The following acronyms and symbols have been used in this thesis. In general, these are in standard notation and are included here for reference purposes. Standard symbols comply with IUPAC conventions[1].

B_0	static magnetic field of an NMR spectrometer
B_1	RF magnetic field associated with v_1
β	Euler angle
θ	angle between a given vector and B_0
ζ	shielding anisotropy
CP	cross-polarisation
CSA	chemical shift anisotropy
CW	continuous wave
δ_X	chemical shift (of nucleus X)
D	dipolar coupling constant
D'	effective dipolar coupling constant
D^C	nuclear receptivity relative to that of the carbon-13 nucleus
D^p	nuclear receptivity relative to that of the proton (hydrogen-1 nucleus)
η	asymmetry
FID	free induction decay
FT	fourier transform
γ	gyromagnetic ratio
h	Planck's constant = 6.626×10^{-34} J s. ($\hbar = h/2\pi$)
H	Hamiltonian
HX	proton-X nucleus probe
J	indirect scalar (spin-spin) coupling
Kel-F	$(CF_2CFCl)_n$

---

[1] R.K. Harris, J. Kowalewski, S.C.D. Menezes, Pure Appl. Chem. 12 (1997) 2489.

M_0	magnetisation at equilibrium state
MAS	magic-angle spinning
ν	frequency
NMR	nuclear magnetic resonance
ppm	part per million
r	internuclear distance
ramped-CP	ramped-amplitude cross-polarisation
RF	radio frequency
σ	shielding tensor
SIMPSON	a general simulation program for solid-state NMR spectroscopy
SSB97	an iterative program for spinning sideband analyses
STARS	spectrum analysis of rotating solids
T_1	spin-lattice relaxation time
$T_{1\rho}$	spin-lattice relaxation time in rotating frame
T_2	spin-spin relaxation time
τ	time between RF pulses
TPPM	two-pulse phase modulation
Vespel	fluorine free polymer

Contents

CHAPTER 1

INTRODUCTION

The nuclear magnetic resonance phenomenon was first recorded in 1945 by Purcell *et al.* [1] and by Bloch *et al.* [2]. Purcell and his colleagues observed their first NMR signal from the protons in solid paraffin wax, whist Bloch and his colleagues obtained a signal from the protons in liquid water. Useful chemical applications became possible after the discovery of the chemical shift effect in 1949 [3,4]. Since its discovery, NMR has developed considerably and has become an important technique for the elucidation of molecular structure in the solution state. In the past, progress in solid-state NMR was hampered by technical and conceptual difficulties. Today, however, it is acceptable that solids are (almost) as amenable to NMR as solutions by combining three techniques, namely magic-angle spinning (MAS), cross-polarisation (CP) and efficient proton decoupling [5-8], as will be discussed in the following Chapter. Furthermore, solid-state NMR is becoming increasingly important, since it is used in the elucidation of structure and dynamics of many solid inorganic, organic and organometallic compounds and materials.

The main work presented in this thesis is the study of a range of tin- and silver-containing solid compounds using high-resolution solid-state NMR techniques. Each series of compounds will be introduced in the corresponding Chapters. The aims of the work are to examine the solid-state structures, to obtain NMR parameters (including anisotropies) and to understand the behaviour in coupled two-spin ($^{31}P,^{1}H$) systems.

In the following chapter, a brief overview of the basic principles of NMR spectroscopy as it applies to the solid-state is given, while Chapter 3 briefly describes the experimental considerations. Chapter 4 reports some of the results for the tin-containing compounds. Chapter 5 investigates the coupled two-spin ^{31}P, ^{1}H systems, providing an indirect spin-spin coupling and also the P,H internuclear distances. Chapter 6 reports the application

of high-resolution solid-state NMR to some silver-containing compounds and Chapter 7 describes the complications in the relaxation behaviour of the coupled two-spin ^{31}P, ^{1}H systems.

1.1   References

[1]   E.M. Purcell, H.C. Torrey, R.V. Pound, Phys. Rev. **69** (1946) 37.

[2]   F. Bloch, W.W. Hansen, M.E. Packard, Phys. Rev. **69** (1946) 127.

[3]   W.G. Proctor, F.C. Yu, Phys. Rev. **77** (1950) 717.

[4]   W.C. Dickinson, Phys. Rev. **77** (1950) 736.

[5]   I.J. Lowe, Phys. Rev. Lett. **2** (1959) 285.

[6]   A. Pines, M.G. Gibby, J.S. Waugh, J. Chem. Phys. **59** (1973) 569.

[7]   S.R. Hartmann, E.L. Hahn, Phys. Rev. **128** (1962) 2042.

[8]   J. Schaefer, E.O. Stejskal, J. Am. Chem. Soc. **98** (1976) 1031.

CHAPTER 2

BASIC PRINCIPLES OF SOLID-STATE NMR

This chapter will describe some of the basic ideas that are generally applicable to solid-state NMR. The theory of solid-state NMR is now well-known and can be found in Refs [1-3], and so only a short overview is appropriate here. A few more specific points are discussed in later chapters.

2.1   Nuclear interactions

Initially, it is essential to have an understanding of the nature of NMR interactions. The nuclear spin Hamiltonian consists of a sum of terms that describe physically different interactions of the nuclear spin.   The interactions may be divided into *external* and *internal* spin interactions and may be written as:

$$H_{total} = H_{ext} + H_{int}$$

$$= (H_z + H_{RF}) + (H_D + H_{CS} + H_J + H_Q) \tag{2.1}$$

The *external* spin interactions are those with the external magnetic field B_0 and the time-dependent radio frequency field B_1, which are essentially under the control of the experimentalist. The remaining terms in Equation 2.1 namely, dipolar, shielding, indirect (scalar) coupling and quadrupolar coupling, are the *internal* spin interactions, which represent the interactions of nuclear spins with their surroundings and are independent of the experimental conditions. Brief attention to each internal interaction will now be given as follows:

The *dipole-dipole coupling* or *dipolar coupling* is the direct magnetic interaction between two nuclei through space, which the total interaction is the summation of homo- and heteronuclear interactions. The dipolar interaction is potentially useful for molecular structure determination, since it depends upon the internuclear distance. The dipolar interaction for a pair of non-equivalent nuclei, isolated spins I and S is given by

$$D_{IS} = \left(\mu_0 / 4\pi \right) \gamma_I \gamma_S \hbar / 2\pi r_{IS}^3 \qquad\qquad (2.2)$$

where r_{IS} denotes the internuclear distance. It is important to note that the dipolar interaction leads to an orientation-dependent splitting, in which the doublet splitting is $D_{IS}(3\cos^2\theta - 1)$ where θ is the angle describing the orientation of r_{IS} with respect to B_0. A typical heteronuclear dipolar powder pattern for an isolated spin-pair is shown in Figure 2-1, which consists of the superposition of two subspectra ($m_s = \pm 1/2$).
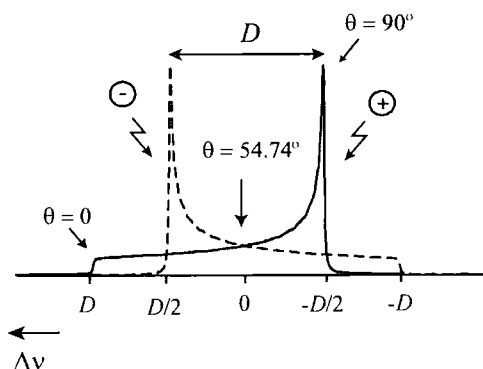
Figure 2-1 Powder pattern showing dipolar coupling (D) for the I spin of an IS system. The subspectrum marked with '+' is associated with S spin state of $+1/2$, whereas the subspectrum with '-' is associated with S spin state of $-1/2$.

The *indirect spin-spin coupling*, J describes the coupling of nuclear spins via the electrons present in the molecular system surrounding them. This interaction (tens to hundreds of Hz) is quite small compared to the dipolar interaction (tens of kHz).

The source of *shielding* of nuclear spins arises from the interaction of the orbital motion of surrounding electrons with the external magnetic field. The magnitude and direction of the interaction will thus be dependent on molecular orientation in B_0. This implies that the interaction is a tensor quantity (see below).

Additionally, a nucleus with $I > \frac{1}{2}$ has a 'quadrupole moment', which interacts with electric field gradients at the nucleus. This interaction is called *quadrupolar coupling* Note that this interaction will not be considered further since it is not relevant to the work presented in this thesis.

All of these internal interactions are second-rank tensors (expressed in terms of 3 × 3 matrices) and, to a first-order approximation, have the same orientation dependence of the form $3\cos^2\theta - 1$, θ being the angle between B_0 and a local molecule-fixed direction. In the general case, molecular motion is usually very limited in solids; hence the NMR spectrum of a solid is influenced by all of these internal interactions simultaneously, producing a complicated spectrum. This is in contrast to the solution state, where the molecules are free to rotate rapidly, so that the total interaction is reduced to the isotropic chemical shift and isotropic indirect coupling, i.e. dipolar and quadrupolar interactions are cancelled out by motional averaging, resulting in high-resolution spectra being obtained.

In a powder sample containing many tiny crystallites, the NMR spectrum is a superposition of contributions from each crystallite, which are randomly orientated with respect to the external magnetic field. Each orientation has a different NMR transition frequency, resulting in the observation of a powder pattern for a static sample, as shown in Figure 2-2 for the case of shielding, i.e. the shielding constant (σ) will vary with the orientation of the molecule (see Figure 2-2 (b) and (c)) unless the electronic environment is highly symmetric (see Figure 2-2 (a)). Thus the shielding interaction affects the width and the shape of this pattern.
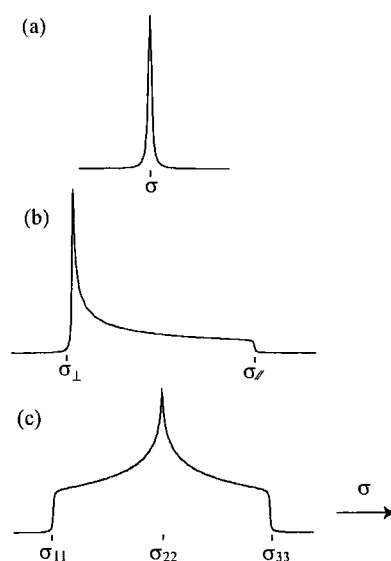
Figure 2-2 Schematic powder patterns caused by shielding anisotropy for a site with (a) cubic symmetry (b) axial symmetry and (c) lower symmetry.

In order to obtain a well-resolved spectrum, a combination of techniques, namely magic-angle spinning (MAS), efficient ^1H decoupling, and cross-polarisations (CP), are frequently used. Each of these techniques will now be considered briefly.

2.2 Magic-angle spinning and high-power decoupling

High-resolution NMR spectra of solids may be obtained by rapidly rotating the sample about an axis at the "magic angle", $\beta = 54.74°$ with respect to the static magnetic field (see Figure 2-3). This technique is known as magic-angle spinning (MAS) [4,5]. The average value of $3\cos^2 \theta - 1$ is zero since this term is proportional to $(3\cos^2 \beta - 1)$. The average angle of θ given by

$$\langle 3\cos^2 \theta - 1 \rangle = \frac{1}{2}(3\cos^2 \beta - 1)(3\cos^2 \chi - 1)$$

(2.3)

where χ is fixed for a rigid solid, and it takes all possible values for a powder sample. θ is all possible angles for a powder. The angle β is at the control of the experimentalist.

Consequently, with MAS all anisotropy effects involving the geometric factor $3\cos^2\theta - 1$, such as the shielding anisotropy and the dipolar interaction, are removed from the spectra and each powder pattern will collapse to a single line at a frequency determined by isotropic chemical shift. Also, rotational sidebands with multiples of the spin rate will be obtained if a spin rate is less than the shielding anisotropy (in frequency units).
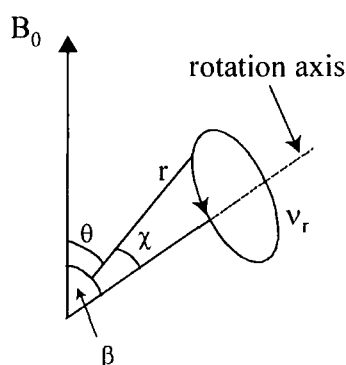
Figure 2-3 Magic-angle spinning of a rotor with a spin rate of v_r. r is the internuclear vector.

Use of MAS alone cannot remove the dipolar interaction effectively since this interaction can be several tens of kHz (e.g. carbon-proton dipolar interaction); such an approach would require higher spin rate than are available today (2004). Thus, high-power decoupling is often required to remove the heteronuclear dipolar interaction properly.

Decoupling is achieved by applying a strong RF field to non-observed spins (e.g. proton). Normally, this is done continuously and is known as 'CW decoupling'. The RF irradiation causes the non-observed spins to change their spin states (e.g. α and β states for proton) rapidly compared with the heteronuclear dipolar interaction, and thus 'decouples' them from the observed spin. CW decoupling works well at low magnetic fields and modest spin rates. However, often CW decoupling becomes inefficient at high magnetic field when the MAS frequency exceeds the proton-proton interaction, leading to an increase in resonance offset effect, and resulting in residual linewidths. Fast spin rates at high magnetic fields are required to reduce the sideband intensities due to the size of

chemical shift anisotropy (e.g. CSA for a carbonyl carbon is in order of 30 kHz at 18.8 T).

A multiple-pulse heteronuclear decoupling scheme, TPPM (two-pulse phase modulation) is now widely used instead of CW decoupling. This pulse sequence has been proved to be more efficient than CW decoupling in the regime of high magnetic fields and fast spin rates (see this pulse sequence in Chapter 3), in which increases an enhancement in resolution and in sensitivity compared to CW.

2.3   Cross-polarisation

Cross-polarisation (CP) [6] is a powerful technique for acquiring spectra of rare spin systems, e.g. ^{13}C, in organic solids. CP allows enhancement of the signal by transferring magnetisation from the protons to the observed spins. Another benefit of using this technique is the reduction in the recycle delay between radio frequency pulses since the recycle delay depends on the relaxation time (T_1) of the abundant spin (usually ^1H) rather than that of the observed spins (which is generally longer).

Cross-polarisation is achieved in a double-resonance experiment. A 90° pulse is applied to the proton channel and this magnetisation is then spin-locked. At this point B_{1S} is turned on and magnetisation is transferred from the protons to the dilute spins if the Hartmann-Hahn matching condition [7], $\gamma_H B_{1H} = \gamma_S B_{1S}$, is satisfied. The enhancement is proportional to the ratio $|\gamma_H / \gamma_S|$.

CP, however, is not limited to dilute spin systems like ^{13}C. It can be applied to abundant spin systems, like ^{31}P. Very recently, the application of CP to low-γ nuclei has been reviewed by Sebald [8].

CP experiments are usually combined with MAS. At low spin rates, the CP is very efficient and the matching profile is rather broad. The matching profile represents the cross-polarisation efficiency, which is the intensity of the observed signal as a function of RF field strength for a fixed mixing time. Under static conditions, the CP matching profile consists of a broad unstructured peak centred at $v_H = v_S$ with the width comparable to homogeneous proton linewidth, where v_H, v_S are RF field strengths applied to proton and S spins respectively. With increasing spin rate, when the MAS frequency exceeds the proton-proton interaction, it significantly influences the CP process [9,10]. This is because the matching profile breaks down into a series of sidebands separated by rotor frequency [11,12], $v_I = v_S + nv_r$ where v_r is the spin rate. When this occurs, the matching at the centre becomes inefficient (as the matching profile shows 'dip' at the centre); on the other hand, efficient CP can be obtained by matching on a sideband. The most efficient transfer is found at the $n = \pm 1$ and $n = \pm 2$ sidebands. However, the accuracy of the matching is much more critical due to the narrower matching profiles obtained at higher spin rates. Fortunately, a pulse sequence incorporating a variable or ramped amplitude cross-polarisation pulse sequence [13,14] has been suggested for circumventing this problem. Use of this pulse sequence extends the range of matching conditions and allows for deviation from an exact Hartmann-Hahn matching during an experiment.

2.4   Spinning-sideband analysis

One of the advantages of solid-state NMR is that the principal components of shielding tensors can be obtained, whereas in solution-state they are averaged by molecular tumbling to the isotropic value. The shielding tensors provide potential information about the bonding and structure, especially regarding the local chemical environment of the nucleus.

At moderate spin rates (less than the static bandwidth), spinning sidebands will be observed, with lines that are separated from the isotropic shift by multiples of the rotor spinning frequency. The spinning sidebands can be analysed to yield the values for the

shielding tensor elements. For analysis of the spinning sidebands, to obtain values for anisotropy and asymmetry via the principal shielding tensor components, an iterative program for spinning sideband analyses (SSB97) [15] written in-house was used.

The conventions regarding the shielding tensor information used in this thesis are based on Haeberlen [16]. The three-tensor elements are labelled in the following form:

$$|\sigma_{33} - \sigma_{iso}| \geq |\sigma_{11} - \sigma_{iso}| \geq |\sigma_{22} - \sigma_{iso}| \quad (2.4)$$

where σ_{iso} is the isotropic chemical shift and is given as:

$$\sigma_{iso} = \frac{1}{3}(\sigma_{11} + \sigma_{22} + \sigma_{33}) \quad (2.5)$$

More positive shielding values correspond to lower resonance frequencies (i.e., $\sigma - \sigma_{ref} = -\delta$). The shielding anisotropy has two different definitions, defined as in Equations (2.6) and (2.7), respectively.

$$\Delta\sigma = \sigma_{33} - (\sigma_{11} + \sigma_{22})/2 \quad (2.6)$$

$$\zeta = \sigma_{33} - \sigma_{iso} \quad (2.7)$$

Obviously, they are related by $\Delta\sigma = 3\zeta/2$. Note that the shielding anisotropy can be either positive or negative, depending on whether $\sigma_{33} > \sigma_{22} > \sigma_{11}$ or vice versa.

The shielding asymmetry, η, is defined as

$$\eta = \frac{\sigma_{22} - \sigma_{11}}{\sigma_{33} - \sigma_{iso}} = \frac{(\sigma_{22} - \sigma_{11})}{\zeta} \quad (2.8)$$

This clearly implies $0 \leq \eta \leq 1$. When $\eta = 0$, it means that the nucleus has axial symmetry ($\sigma_{11} = \sigma_{22}$), which can occur for both positive and negative cases of anisotropy. A schematic powder pattern for the case of axial symmetry is shown in Figure 2-2 (b) whereas Figure 2-2 (c) presents a general asymmetric case.

2.5   Interplay of shielding, direct and indirect coupling tensors

When slow spinning is combined with heteronuclear indirect coupling (e.g. in SnHPO$_3$), the spinning sideband manifolds are more complex because of the interplay of shielding (σ), dipolar coupling (D) and indirect coupling (J) tensors [17,18]. The simplest case occurs when σ and J are axially symmetric and when their principal axes are along the relevant internuclear distance and are thus coaxial with D. Then, the anisotropy in J has exactly the same form as D. Since the anisotropy in J cannot be distinguished from D, an effective parameter D' may be defined

$$D' = D - \frac{\Delta J}{3} \tag{2.9}$$

where D is the dipolar coupling constant (in frequency units), and $\Delta J = J_{\parallel} - J_{\perp}$ is the anisotropy in J.

Following Ref. 1, the transition of the I nucleus (in reduced form) in an IS ($I_I = I_S = 1/2$) system is given by

$$v_I = v_I^{iso} - \frac{1}{2} v_I^0 \zeta_I^{eff} \left(3\cos^2 \theta - 1 \right) - J_{IS} m_S \tag{2.10}$$

where $v_I^0 = \gamma_I B_0 / 2\pi$ is the I Larmor frequency in the absence of shielding, m_S is the appropriate spin component quantum number for the S spin, J_{IS} is the isotropic (I,S) coupling constant, θ is the angle between r_{IS} and B_0, and ζ_I^{eff} is an effective tensor anisotropy given by

$$\zeta_I^{\mathit{eff}} = \zeta_I - \frac{2D' m_S}{v_I^0}$$
(2.11)

Thus this means that one static powder subspectrum ($m_S = -1/2$) is 'stretched' whereas in the other ($m_S = 1/2$) is 'squeezed'. Note that ζ_I and γ_I are assumed to be positive. Figure 2-4 presents the powder pattern when IS system is influenced by both dipolar interaction and shielding anisotropy.
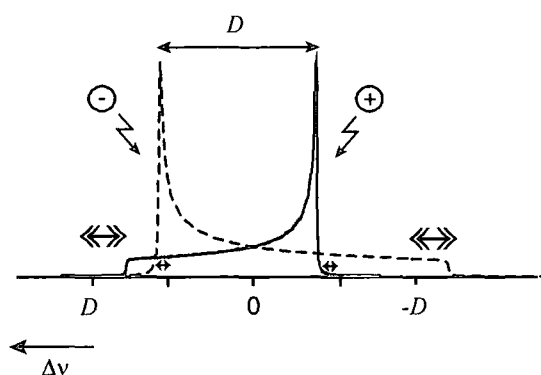
Figure 2-4 Powder pattern for the I spin of an IS system influenced by both (I,S) dipolar interactions and axially symmetric shielding anisotropy (with $\sigma_\parallel > \sigma_\perp$). The subspectra marked with '+' and '-' have the same significance as in Figure 2-1. The small separation marked by single and double-headed arrows are of magnitudes $v_I^0 \zeta_I / 2$ and $v_I^0 \zeta_I$, respectively. It is assumed that the symmetry axis of shielding is in the internuclear direction.

Under slow MAS conditions, the influence of the angle-dependent term $3\cos^2 \theta - 1$ is translated into the distribution of intensities among the relevant spinning sidebands. For one spinning-sideband manifold, the effects of shielding anisotropy and dipolar interaction are additive (stretched sub-spectra), whereas for the other the tensors tend to compensate (squeezed sub-spectra). The isotropic indirect coupling serves to differentiate between the manifolds and thus two values ζ_I^{eff} can be obtained by the analysis of spinning sidebands. This allows ζ_I and D' to be derived independently.

2.6   Spin echoes in coupled systems

It is worth considering a spin-echo sequence here since it will be important in later chapters.

By using a spin-echo pulse sequence, inhomogeneities in the static magnetic field and chemical shift differences can be refocused [2,19]. In the basic spin-echo sequence (Figure 2-5 (a)), an initial 90° pulse turns M_0 into the y direction (Figure 2-6 (b)). The magnetisation vectors move ahead of the mean whilst others lag behind during the time period τ (Figure 2-6 (c)). A $180°_y$ pulse is then applied after time τ, which has the effect of rotating the faster moving vectors and the slower ones along y, in other words reflecting them in the yz plane. They continue to move in the same direction, and after a refocus time equal to τ they are again in phase in the yz plane. This pulse sequence can be modified by applying successive $180°_y$ pulses (Figure 2-5 (b)), resulting in a series of echoes of decaying intensity. This sequence is known as the Carr-Purcell-Meiboom-Gill (CPMG) [20,21].
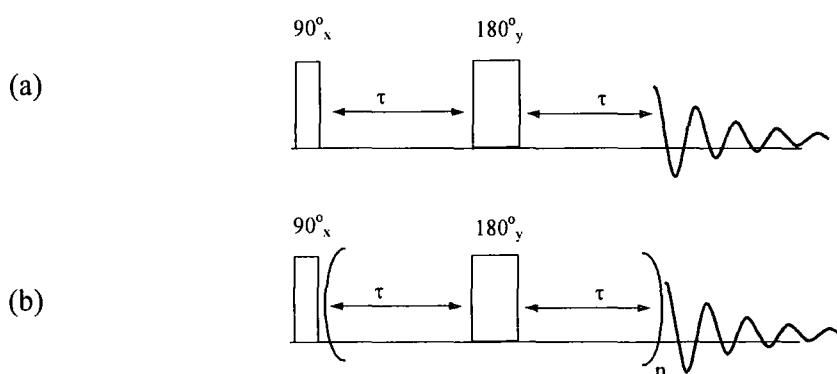
Figure 2-5 Spin-echo sequences (a) A basic spin-echo and (b) Carr-Purcell-Meiboom-Gill (CPMG) sequence. In CPMG, data points will be acquired between pulses.
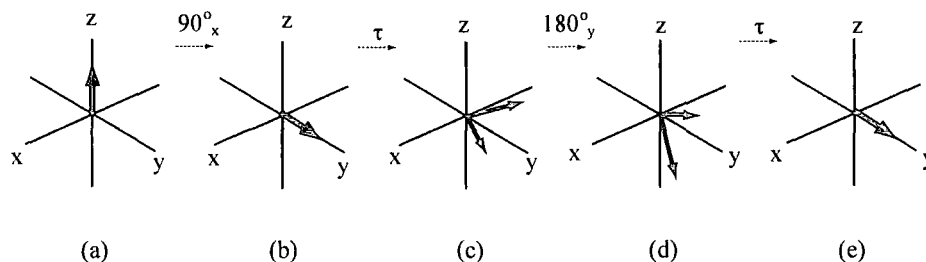
Figure 2-6 The spin-echo refocuses magnetisation vectors dephased by field imhomogeneity or by chemical shift differences.

The spin-echo experiment provides a useful means for observing spin-spin couplings. For a heteronuclear AX system, the net magnetisation of A (observed nuclei) can be considered as composed of two separate magnetisations, $M_A^{X\alpha}$ and $M_A^{X\beta}$, for A nuclei with their X neighbours in the α and β states respectively. The heteronuclear coupling will be refocused in exactly the same way as chemical shifts (see above). Figure 2-7 shows the schematic illustration of A magnetisation vectors during a spin-echo pulse sequence. Note that in Figure 2-7 J_{AX} is positive, so that $M_A^{X\beta}$ will precess faster than $M_A^{X\alpha}$. Any direct effect of the pulses on the X spin has been ignored.
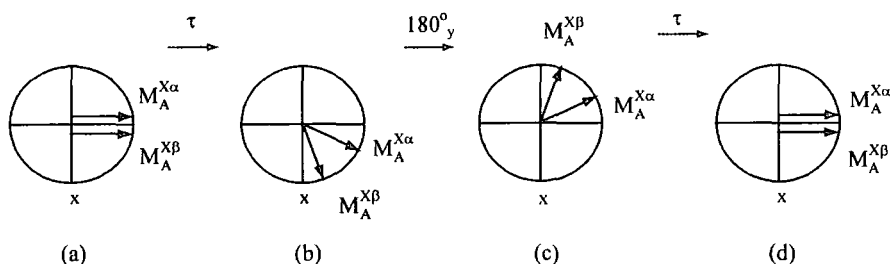
Figure 2-7 The evolution in the x/y plane of the A magnetisation vectors of a heteronuclear AX spin system during a spin-echo pulse sequence.

On the contrary, if a homonuclear AX system is considered, with the pulses affecting A and X equally, a different situation will be obtained (Figure 2-8). The 180° pulse on the X spins inverts the populations of the X-spin levels, and thus has the effect of changing the labels of the Xα and Xβ states. Consequently $M_A^{X\alpha}$ and $M_A^{X\beta}$ are interchanged, and this would normally occur at the same time as the 180° rotation of these magnetisations

about the y direction (Figure 2-8 (c)). Thus refocusing does not occur after time τ later, as in Figure 2-8 (d), because the faster vector is now still ahead of the slower one. This relates to the phase angle generated at time 2τ, $\phi = 4\pi J_{AX}\tau$.
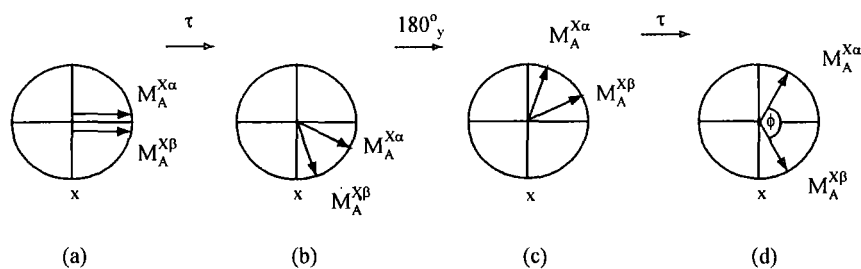
Figure 2-8 The evolution in the x/y plane of the A magnetisation vectors of a homonuclear AX spin system during a spin-echo pulse sequence.

When the signal is sampled at the maximum of the echo, the net magnetisation is given by

$$M_A(2\tau) = M_A^0 \cos 2\pi J_{AX}\tau \qquad (2.12)$$

This implies that the echo height will vary cosinusoidally with τ. A series of measurements of echo heights yields data that contain a modulation from the relevant coupling, therefore an A spectrum obtained from Fourier transformation shows two A lines of the AX spin system.

Applying 180° pulses simultaneously to both A and X spins, 90°(A) – τ – 180°(A)/180°(X) – τ –, allows evolution under heteronuclear J couplings to be observed.

2.7 References

[1]   M. Mehring, Principles of High Resolution NMR in Solids, 2nd ed., Springer-Verlag, Berlin, 1983.

[2]   R.K. Harris, Nuclear Magnetic Resonance Spectroscopy, Longman, London, 1987.

[3]   M.J. Duer, Solid-state NMR Spectroscopy Principles and Applications, Blackwell Science, Oxford, 2002.

[4]   E.R. Andrew, A. Bradbury, R.G. Eades, Nature 182 (1958) 1659.

[5]   I.J. Lowe, Phys. Rev. Lett. 2 (1959) 285.

[6]   A. Pines, M.G. Gibby, J.S. Waugh, J. Chem. Phys. 59 (1973) 569.

[7]   S.R. Hartmann, E.L. Hahn, Phys. Rev. 128 (1962) 2042.

[8]   A. Sebald, NMR Basic Principles and Progress. 31 (1994) 91.

[9]   E.O. Stejskal, J. Schaefer, J.S. Waugh, J. Magn. Reson. 28 (1977) 105.

[10]   M. Sardashti, G.E. Maciel, J. Magn. Reson. 72 (1987) 467.

[11]   B.H. Meier, Chem. Phys. Lett. 188 (1992) 201.

[12]   S. Ding, C.A. McDowell, C. Ye, J. Magn. Reson. A 109 (1994) 6.

[13]   G. Metz, X. Wu, S.O. Smith, J. Magn. Reson. A 110 (1994) 219.

[14]   G. Metz, M. Ziliox, S.O. Smith, Solid State Nucl. Magn. Reson. 7 (1996) 155.

[15]   J.R. Ascenso, L.H. Merwin, H. Bai, in-house sideband fitting program, University of Durham.

[16]   U. Haeberlen, High-resolution NMR in solids: Selective Averaging, 1976.

[17]   R.K. Harris, K.J. Packer, A.M. Thayer, J. Magn. Reson. 62 (1985) 284.

[18]   R.K. Harris, A.C. Olivieri, in Encyclopedia of NMR, Vol. 9, pp 141, Wiley, London, 2002.

[19]   E.L. Hahn, Phys. Rev. 80 (1950) 580.

[20]   S. Meiboom, D. Gill, Rev. Sci. Instr. 29 (1958) 688.

[21]   H.Y. Carr, E.M. Purcell, Phys. Rev. 94 (1954) 630.

CHAPTER 3

EXPERIMENTAL DESCRIPTIONS

The general experimental procedures will be described in this chapter.

3.1   Spectrometers and probes

Three solid-state NMR spectrometers were used for the work presented here, namely a Chemagnetics CMX200, a Varian UnityPlus 300, and a Varian InfinityPlus 500. Additional information is often obtained when working at different field strengths, e.g. a potential increase on resolution of spectra at higher field. In the other hand, working at higher field generally requires higher spin rates to remove the spinning sidebands since the shielding anisotropies are increased with increasing magnetic field.

The similarities and differences between the three spectrometers are described below.

The Chemagnetics CMX 200 has a 4.7 T Oxford instrument magnet and operates at a proton resonance frequency of 200.13 MHz. Chemagnetics probes with a Pencil rotor design were employed. The HX probes have been mainly employed for MAS experiments in this work, the rotor diameters being 4 and 7.5 mm.

The Varian UnityPlus 300 is equipped with a 7.05 T Oxford instrument magnet, operating at 299.8 MHz for protons. The probes were supplied by Doty Scientific. Most of the Sn-119 spectra (except for SnC_2O_4) were obtained from this spectrometer, the rotor diameters used being 4 mm. Most of the Ag-109 spectra were acquired from the 300 MHz spectrometer on the 5 mm probe, while a 7 mm MAS probe was used for most of the C-13 spectra of the silver-containing compounds (except for $[Ag(quin)_2]NO_3$ which was observed using 7.5 mm probe).

For the Varian InfinityPlus 500, a magnet of 11.7 T is manufactured by Oxford Instruments. The proton resonance frequency is 499.70 MHz. This system uses the Varian (Chemagnetics) HX probes, and the Chemagnetics "spinsight" software controls the system. A 7.5 mm double-resonance HX MAS probe (equipped with an external tuning box for frequencies below ^{15}N) was employed to observe the Ag-109 spectra. Using the low gamma tuning box extends the tuning range down to 12 MHz. Hence, the 'tune' and 'match' process can be directly adjusted using this box. Spinning up to 22 kHz can be obtained by using a small rotor diameter (3.2 mm) HX probe. Thin-walled rotors (zirconia) with short caps were used with this probe to achieve the maximum signal-to-noise ratio. Most of the variable contact time experiments described in Chapter 5 were undertaken on the 3.2 mm probe.

As shown above, HX probes have been mainly employed for MAS experiments in this work. Such probes operate on two channels, one of which needs to be tuned to the proton resonance frequency, whereas the other one will be tuned to frequency ranging from ^{31}P frequency to ^{15}N frequency, adjusted by changing the capacitors.

The rotors used in the three spectrometers were made from zirconia with drive tips in Kel-F (7 and 7.5 mm), Vespel (4 and 5 mm) and Torlon (3.2 mm), and Teflon end caps.

3.2 Nuclei of interest and chemical shift references

Table 3-1 gives the frequencies and chemical shift references of the standard samples used. Referencing was done by replacement and the chemical shifts adjusted as follows:

Table 3-1 Standard references

Nucleus	Frequency / MHz	Secondary standard	δ/ ppm	Primary standard at 0 ppm
^{1}H	200.13^a	Polydimethylsiloxane (PDMSO)	0.0	TMS
^{31}P	81.02^a	Brushite (CaHPO$_4\cdot$ 2H$_2$O)	1.2	85 % H$_3$PO$_4$
^{119}Sn	74.56^a	Tetracyclohexyltin (C$_6$H$_{11}$)$_4$Sn	-97.4	Me$_4$Sn
^{13}C	50.33^a	Adamantane (C$_{10}$H$_{16}$)	38.4^c	TMS
^{77}Se	57.27^b	Ammonium selenate ((NH$_4$)$_2$SeO$_4$)	1040.2	(CH$_3$)$_2$Se
^{15}N	30.40^b	Ammonium nitrate (NH$_4$NO$_3$)	-5.1^d	CH$_3$NO$_3$
^{109}Ag	13.97^b	-	0.0	AgNO$_3$

^{a} At magnetic field of 4.7 T
^{b} At magnetic field of 7.05 T
^{c} High frequency resonance
^{d} Nitrate peak

3.3   Magic-angle setting

The magic-angle should always be set properly before MAS experiments. Although small mis-sets do not usually significantly influence linewidths, the proper setting is very important when the observed nuclei have a large shielding anisotropy (most heavy metal nuclei such as ^{119}Sn, ^{207}Pb and ^{199}Hg). This is because the shielding anisotropy cannot be completely removed when the rotor is spinning off 54.74°, resulting in the fact that a scaled powder pattern will be observed.

Setting the magic-angle is simply done by monitoring ^{79}Br (from KBr) FID signals and maximizing the duration of the rotary echo train in the FID. If the angle is well-set, the echoes should last for at least 10 ms.

3.4   Recycle delay setting

The recycle delay is the time between the end of the data acquisition from one FID and the start of the next period of RF excitation. During this delay, the magnetisation of the sample returns towards the equilibrium state. The sample is returned to its equilibrium state with a rate of $1/T_1$ where T_1 is the spin-lattice relaxation time (of the observed nuclei for direct polarisation operation but of protons when cross polarisation from ^{1}H is used). T_1 is sample dependent, and it is important to choose the optimum delay before starting the experiment. If the delay is too long, it will waste spectrometer time. On the other hand, a delay which is too short can result in the loss of signal due to saturation.

Full relaxation requires a recycle delay of $5 \times T_1$. However, for a fixed experiment time (number of transients × recycle delay) the best signal-to-noise ratio is obtained at ~ 1.2 × T_1 not at $5 \times T_1$ [1]. This delay can only be used for experiments for which quantitative signal intensities are not important (e.g. cross-polarisation experiments). This optimal delay can be estimated by 'arraying' the recycle delay. The optimum recycle delay gives ~ 70 % of the full intensity.

3.5   Basic acquisition pulse sequences

A number of pulse sequences have been used during the course of the work described in this thesis. The more common pulse sequences used are described in following sections, unless otherwise stated in later Chapters.

3.5.1   Single-pulse excitation (SPE)

The single-pulse excitation experiment is the simplest pulse sequence, which combines a 90° pulse and proton decoupling. The pulse sequence is shown in Figure 3-1. The duration of the 90° pulse is probe- and to some extent sample-dependent. They were generally set at ca. 5 μs for 7 and 7.5 mm probes and 4-5 μs for 4 and 3.2 mm probes.

Efficient proton decoupling is necessary when there are strong X-H heteronuclear dipolar interactions present. Continuous wave (CW) decoupling is the most common way to decouple protons in solid-state NMR. However, two-pulse phase modulation (TPPM) [2] was used to decouple phosphorus for $SnHPO_3$. The expanded region of this pulse sequence is shown in Figure 3-1. TPPM consists of the application of RF pulses of length τ_p, alternating between two phases separated by an angle ϕ. Since τ_p and ϕ are dependent on the MAS frequency and the system under study, both parameters need to be optimised before using the TPPM sequence in this work.
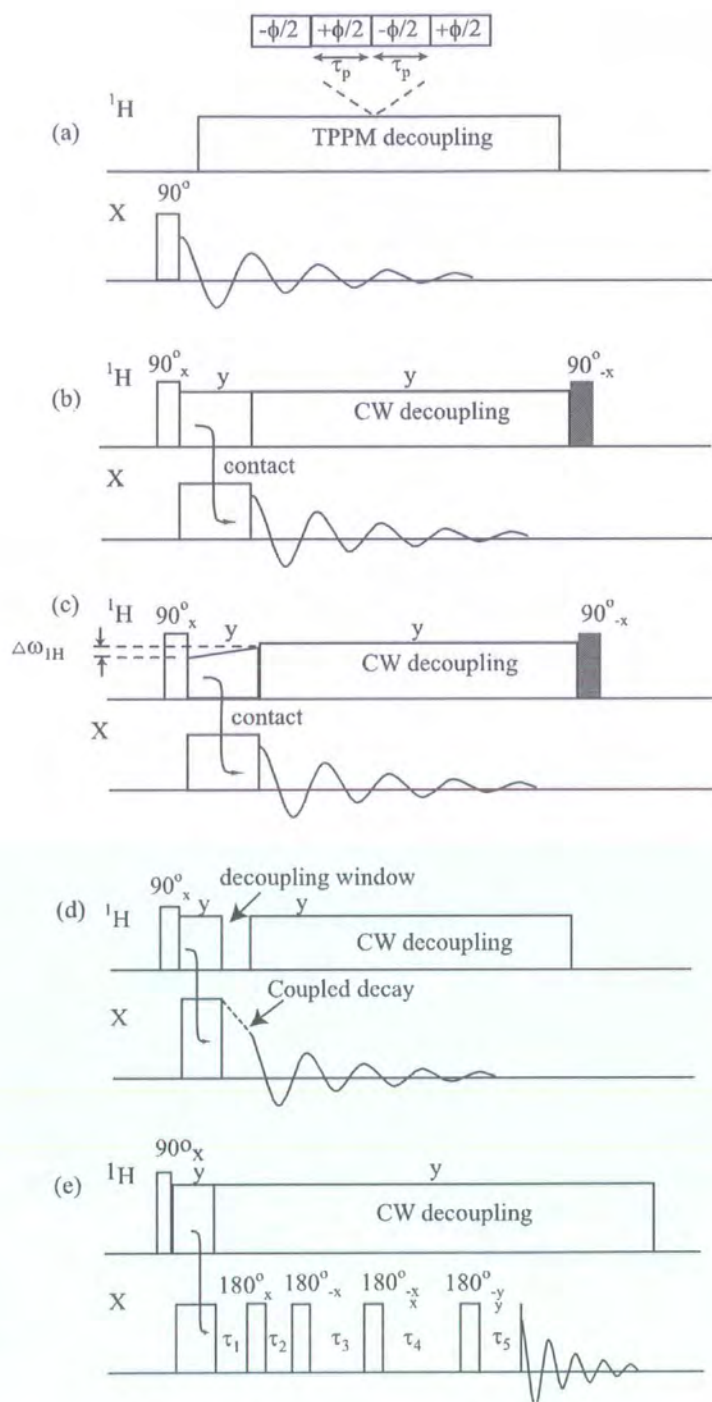
Figure 3-1 Pulse sequence: (a) SPE with CW decoupling; (b) CP; (c) ramped-CP; (d) dipolar dephasing (NQS); (e) TOSS.

3.5.2   Cross-polarisation and Ramped-Amplitude Cross-Polarisation

As described in Chapter 2, cross-polarisation (CP) is used to enhance the magnetisation of dilute spins from abundant spin, e.g. protons. Figure 3-1 shows the pulse sequence. This sequence, together with a "flip back" pulse on the ^{1}H channel after the acquisition time, was used to obtain ^{13}C and ^{15}N spectra for the silver-containing compounds.

The Hartmann-Hahn condition, $\gamma_H B_{1H} = \gamma_S B_{1S}$, is achieved by varying the RF power of either the H channel or the X channel using a suitable standard compound. The matching condition was considered to occur when the signal was maximised. Since the RF field strength is related to the 90° pulse duration, it is necessary to set the 90° pulse on both channels properly by varying the pulse duration for any given power until the maximum signal is obtained. Note that it is important to know what the limit of the RF power is for the probe used.

For each compound (e.g. for a ^{13}C spectrum), the optimum contact time can be found by varying the contact time, which gives the maximum signal. It is worth noting that for nitrogen-containing compounds it is not easy to optimise the contact time directly because the ^{15}N intensity is probably too low. However, the optimum contact time can be determined by considering the signal behaviour for carbon as a function of contact time. This is because in a CP experiment the proton source for ^{1}H to ^{13}C is effectively the same as that for ^{1}H to ^{15}N. It has been found in practice that it is better to use longer contact times for ^{15}N than for ^{13}C. This is only feasible when $T_{1\rho}{}^{(H)}$ (spin-lattice relaxation time in rotating frame) is significantly longer than the optimum contact time for ^{13}C. This is probably because ^{15}N and ^{1}H dipolar interaction is on average weaker than ^{13}C and ^{1}H dipolar coupling (e.g. $\gamma_N < \gamma_C$).

As mentioned above, the flip-back is extra pulse consisting of a 90° pulse of opposite phase from the first one (i.e. 90°$_{-x}$ if the first one is 90°$_x$) [3]. The flip-back pulse has the effect of returning proton magnetisation that remains spin-locked at the end of acquisition to the z-direction. So, the optimum recycle delay can be reduced using the flip-back pulse since less spin-lattice relaxation is required. Flip-back is only effective when $T_{1\rho}{}^{(H)}$

> contact time + acquisition time. In addition, it is important to choose the acquisition time with care since very short acquisition time can cut off FID; on the other hand, very long acquisition time simply adds noise (and also heats the probe).

Most of tin-119 spectra were obtained using ramped-amplitude cross-polarisation on the 300 MHz spectrometer. The pulse sequence for ramped-CP is shown in Figure 3-1. In the conventional Hartmann-Hahn matching, the RF field strengths on the two nuclei are kept constant ($v_{1H} = v_{1Sn}$) during the contact time whereas, in ramped-CP, the proton RF field strength is changed linearly over the ramp size Δv_{1H} while the tin amplitude is kept constant. A 90° pulse on the proton channel was set to 3 μs (equivalent to 83 kHz). The proton RF field strength over the ramp was varied in a range of 62–83 kHz, which covered the −1 sideband (see Chapter 2): spin rates were in a range of 11–15 kHz.

3.5.3   Dipolar dephasing (Non-quaternary suppression)

Figure 3-1 shows the pulse sequence of non-quaternary suppression (NQS), which is also known as dipolar dephasing. The difference from the CP pulse sequence lies in the insertion of a window in the proton decoupling before acquisition of the FID. The duration of this window for ^{13}C observation is typically 40 μs. During this period, ^{13}C signal dephases under the influence of dipolar couplings to the protons. The rate of signal loss is dependent on the magnitude of C,H dipolar interaction. Carbons with directly attached protons generally dephase rapidly, whereas non-protonated carbons dephase more slowly. Methyl groups are usually observed in NQS spectrum because rapid rotation greatly diminishes the effective dipolar interaction. Hence, this pulse sequence assists assignment of carbon signals.

3.5.4 Total sideband suppression (TOSS)

In order to obtain a spectrum free of spinning sidebands, the technique called total sideband suppression (TOSS) is used [4]. The pulse sequence is show in Figure 3-1. This sequence applies a series of 180° pulses at carefully determined delays before acquisition of the FID. Usually four 180° pulses are used, with phase cycling to compensate for pulse imperfections.

The TOSS pulse sequence makes phase alternation of the mth-order spinning sideband, resulting in cancellation of the mth-order spinning sideband at the end of the pulse sequence. TOSS is most useful when there is a small number of spinning sidebands, as is usually the case for ^{13}C. This technique, however, is not well-suited for the case of many spinning sidebands (e.g. ^{119}Sn and ^{109}Ag spectra) since small residual phase-distorted spinning sidebands are always observed.

3.6 Sample sources

The following samples were studied during the course of this work and the sources of the compounds are given accordingly.

3.6.1 Tin-containing compounds

$SnHPO_3$ and $SnHPO_4$ were prepared at University of Durham by the published methods [5,6]. CaSnEDTA was prepared by the method of Langer [7], and supplied by Dr. P. C. Waterfield, Unilever Research (Port Sunlight Laboratory). The other three compounds investigated were supplied commercially: $Sn_2P_2O_7$ by Nihon Kagaku, SnC_2O_4 by Sigma and $SnSO_4$ by Aldrich.

3.6.2 Silver-containing compounds

The series of silver-containing compounds were synthesized, purified and supplied by Prof. G. A. Bowmaker, Department of Chemistry, University of Auckland, New Zealand.

3.7   References

[1]   http://www.dur.ac.uk/solid.service/nmr.htm.

[2]   A.E. Bennett, C.M. Rienstra, M. Auger, K.V. Lakshmi, R.G. Griffin, J. Chem. Phys. **103** (1995) 6951.

[3]   J. Tegenfeldt, U. Haeberlen, J. Magn. Reson. **36** (1979) 453.

[4]   W.T. Dixon, J. Chem. Phys. **77** (1982) 1800.

[5]   R.C. McDonald, A.R. Erisks, Inorg. Chem. **19** (1980) 1237.

[6]   K. Jablczynski, W. Wieckowski, Z. Anorg. Allg. Chem. **152** (1926) 207.

[7]   H.G. Langer, Inorg. Nucl. Chem. **26** (1964) 767.

CHAPTER 4

SOLID-STATE NMR STUDIES OF TIN-CONTAINING COMPOUNDS

4.1 Introduction

The element tin possesses several isotopes of which three (^{115}Sn, ^{117}Sn, ^{119}Sn) are spin-1/2 and hence magnetically active (see Table 4-1). Most published tin NMR measurements refer to the ^{119}Sn nucleus due to its slightly higher magnetic moment than ^{117}Sn and appreciable natural abundance of 8.59 %. Its good sensitivity and large chemical shift range (ca. 2500 to –2500 ppm with respect to the signal for Me$_4$Sn) make Sn NMR valuable for structure determination [1-4].

Table 4-1 NMR properties of tin isotopes [5].

Isotope	Natural abundance / %	Magnetic moment (μ/μ_N)	Magnetogyric ratio (γ / 10^{-7}rad T^{-1} s^{-1})	Relative receptivity (D^C)
^{115}Sn	0.34	-1.5915	-8.013	0.711
^{117}Sn	7.68	-1.1338	-9.588	20.8
^{119}Sn	8.59	-1.8139	-10.0317	26.6

Shielding anisotropies are in general large for Sn, so that high-speed spinning is required (more than 10 kHz in the present study) to obtain acceptable spectra. It has been known for a long time that the combination of cross-polarisation (CP) and the magic-angle-spinning (MAS) becomes more difficult at high MAS rates because the cross-polarisation profile (Hartmann-Hahn matching condition [6]) breaks down. As a result, it is hard to obtain maximum signal intensity [7-9]. Therefore, ramped-amplitude cross-polarisation (ramped-CP) [10,11] has been used in the present work to circumvent this problem.

Of course, cross polarization is only feasible if the compound in question contains a suitable abundant-spin nuclide (usually ^{1}H), otherwise direct polarization (DP) methods must be used. The latter becomes very inefficient when ^{119}Sn spin-lattice relaxation times are long.

The primary reason for use of the MAS technique in solid-state NMR is to eliminate effects of orientation-dependent nuclear spin interactions. While rapid magic-angle spinning provides high-resolution spectra of solids, all information about the shielding is lost, other than the isotropic value. If the spin rate is large with respect to the shielding anisotropy, only a single peak will be obtained at the isotropic value. Lower spin rates result in a series of spinning sideband resonances, separated from the relevant centreband by multiples of the spinning frequencies. The distribution of intensities in these sideband manifolds contains information about the shielding anisotropy, which gives an opportunity to create correlations between anisotropies and the nature of the environment for the relevant nuclei. Therefore, it is of interest to extract the anisotropy data to gain better understanding of molecular structure. Spinning-sideband manifolds were analysed in this chapter using an in-house computer program [12], SSB97, based on the method of Maricq and Waugh [13]. This iterative program minimises the sum of differences squared between the experimental and calculated intensities to find the principal components of the shielding tensors and hence anisotropy and asymmetry. The accuracy of the results is heavily dependent on the number of spinning sidebands used and, in particular, the intensities of the outer sidebands, i.e. signal-to-noise of the spectrum. The better the signal-to-noise ratio, the more accurate the fitting will be [14,15]. It is, in any case, desirable to obtain at least two spectra to locate the centrebands, which are invariant in position to the spin rate, in contrast to the sidebands. The results of the shielding tensors are averaged because more than one spin rate are analysed.

Whilst ^{119}Sn spectra of many solid Sn(IV) compounds have been obtained [16-21], there are relatively a few reports of studies of Sn(II) systems [22-29]. Therefore, the main focus of this chapter is on presenting spectra and extracting the components of shielding tensors for six such solid compounds, namely tin phosphite ($SnHPO_3$), tin hydrogen phosphate ($SnHPO_4$), tin diphosphate ($Sn_2P_2O_7$), tin oxalate (SnC_2O_4), tin sulfate

(SnSO$_4$) and calcium tin ethylene diamine tetraacetate (CaSnEDTA). Of these, the diphosphate and CaSnEDTA do not have reported crystal structures. Solid-state NMR spectra have been recorded for ^{31}P and ^{119}Sn using single-pulse excitation with and without proton decoupling and ramped-amplitude cross polarization (ramped CP). Some ^{13}C spectra where relevant have been also studied.

In addition to the intrinsic NMR interest of this work, tin(II) compounds have some importance in biochemistry, so that this provides a further motivation. A number of microbiological studies have shown that solutions of the stannous ion will decrease bacterial growth. The data demonstrate that the stannous ion is a more active antibacterial agent than the fluoride ion alone. In vitro studies on the oral organism *Streptococcus mutans* have shown a Minimum Inhibitory Concentration (MIC) of 300 ppm of fluorine for sodium fluoride, while stannous fluoride inhibited growth at only 75 ppm of fluorine [30]. Thus stannous compounds can be considered among the constituents of toothpaste. Other researchers [31] have found that stannic fluoride at 390 ppm Sn has no effect on bacterial growth. We can conclude from these and other studies that the most effective antibacterial form of tin is the stannous ion, Sn(II), and not the stannic ion, Sn(IV). However, the stannous ion in aqueous solution is vulnerable to oxidation to stannic (hence bio-inactive) or via hydrolysis to stannous hydroxides or stannous oxide hydrates, which are insoluble and hence largely inactive as antibacterial agents. Therefore, in order to maximise the antibacterial effect of the stannous ion, careful attention must be taken to provide a source of stannous ions that is both soluble in aqueous media, hence bioavailable, but contained within a structure that sufficiently protects the Sn(II) against hydrolysis or oxidation.

Sn, Sn scalar coupling

Most MAS experiments do not reveal effects arising from isotropic J-coupling in the spectra because they are typically of dilute spin systems (^{13}C or ^{15}N) and are recorded under conditions of proton decoupling. Moreover, linewidths in MAS solid-state NMR obscure splittings arising from coupling constants less than $ca.$ 50 Hz in magnitude. Coupling effects are sometimes seen in ^{31}P spectra, but in this case the situation is relatively simple because of the 100% natural abundance of the nuclide.

Tin represents an unusual case, with ^{117}Sn and ^{119}Sn having similar magnetic properties. The observation of coupling effects is complicated by the dominating influence of spin-zero isotopes (totalling 83.39 %). This implies that coupling between spin-½ tin nuclei may result in satellite peaks around the ^{117}Sn or ^{119}Sn resonances. Moreover, such satellite peaks can, arise from either homonuclear (e.g. ^{119}Sn, ^{119}Sn) or heteronuclear (e.g. ^{119}Sn, ^{117}Sn) coupling. For homonuclear cases, even if there are two nuclei in identical crystal sites, complications may arise in the spectra. If two coupled ^{119}Sn nuclei (for example) have co-axial shielding tensors, they will be completely equivalent, and the spectrum of a static single crystal will be only a single resonance. This will be also observed for a microcrystalline sample under all MAS conditions. On the other hand, if the two spins are not fully equivalent (that is if they are related by symmetry but with shielding tensors that are not co-axial), then the chemical shifts for a static single crystal will generally be different and coupling will cause splittings in the spectrum. For MAS of a microcrystalline powder, when the spin rate is very fast (no spinning sidebands), the averaged chemical shifts will be the same and so coupling will not be effective and a single resonance will be observed. However, if the spin rate is slow, so that spinning sidebands occur, coupling will cause some splittings to appear, which will be spin-rate-dependent and second-order in nature [32,33]. Such satellite peaks will not be separated by $|J(\mathrm{Sn,Sn})|$ but by a value in excess of $2\,|J(\mathrm{Sn,Sn})|$. For tin spectra (in contrast to ^{31}P spectra) the satellite peaks are expected to be very small because of the dominance of a central peak from tin nuclei having only spin-zero neighbours.

4.2 Results and Discussions

The NMR experiments presented here were implemented on Varian InfinityPlus 500, Varian UnityPlus 300 and Chemagnetics CMX 200 spectrometers. The studies of ^{31}P were carried out on the CMX200 and InfinityPlus 500 systems (the latter used only for the static ^{31}P spectrum of $SnHPO_3$), whereas the ^{119}Sn and ^{13}C experiments were done on the Varian UnityPlus 300 spectrometer (except the ^{13}C experiment for SnC_2O_4, which was studied using the CMX200 instrument).

4.2.1 Analysis of shielding tensors

The following compounds were investigated:

Tin(II) phosphite, $SnHPO_3$

An isolated molecule of $SnHPO_3$ in principle contains Sn^{2+} cations and HPO_3^{2-} anions, though in practice there would be considerable covalency. The anion contains a direct P-H bond, constituting a two-spin system when spin-active isotopes of tin are ignored (see Chapter 5).

The general features of the tin(II) phosphite crystallographic data are as follows. The phosphite crystals are monoclinic of space group Ic [34]. The structure consists of sheets of SnO_3 and PO_3 trigonal pyramids fused together at their bases (see Figure 4-1). The PO_3 group has almost exact trigonal symmetry (in term of bond angles and distances; the O(1)-P-O(2), O(1)-P-O(3) and O(2)-P-O(3) angles are 111.5°, 112.3° and 114.7°, respectively; the P-O(1), -O(2) and –O(3) bond distances are 1.53, 1.51 and 1.52 Å, respectively). The SnO_3 pyramids are less symmetric. Each tin atom is coordinated by three separate PO_3 groups. Each oxygen atom bridges one tin and one phosphorus atom. Although the positions of the hydrogen atoms in this compound were not determined, they must be directly bonded to phosphorus, as is known for other phosphites [35]. Therefore, in this case, the hydrogen atom should lie at the top of the PO_3 pyramid at roughly tetrahedral angles with the oxygen atoms.
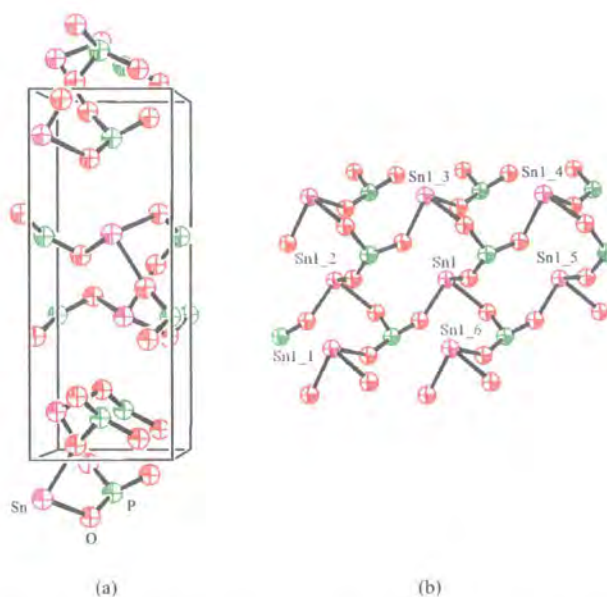
Figure 4-1 Crystal structure of $SnHPO_3$: (a) layers within a unit cell outline (b) the coordination of tin.

As mentioned above, the P-H bond in $SnHPO_3$ can be considered to form an isolated two-spin system by consideration of the distances of P,P, other P,H and H,H. All the distances are extracted from the structure of $MgHPO_3 \cdot 6H_2O$ [35] since it is not possible to locate the hydrogen atom in $SnHPO_3$ by X-ray studies. Table 4-2 summarises the distances and dipolar interactions. The large distances of both P,P and H,H give small dipolar coupling constants, suggesting that the P-H bond is rather isolated.

Table 4-2 Interatomic distances and dipolar coupling constants of $MgHPO_3 \cdot 6H_2O$ [35].

	Distance / Å	Dipolar coupling constant[b] / Hz
P-P[a]	5.957	93
P-H	1.474	15198
H-H	5.957	569

[a] P-P distance for SnHPO3 is 4.127 Å and dipolar coupling constant is 281 Hz.

[b] Dipolar coupling constant $= (\mu_0 / 4\pi)r^{-3}\gamma_1\gamma_2(\hbar / 2\pi)$

Figure 4-2 shows the proton-decoupled ^{31}P spectra with single-pulse-and-acquire operation, obtained at 81.01 MHz. There is only a single centreband at 1.4 ppm observed for ^{31}P. This reveals that only one type of phosphorus exists in the asymmetric unit, in agreement with the crystal structure.

All the spectra in Figure 4-2 have very good signal-to-noise ratios; therefore, the error for measuring the intensities should be small and thus a good fit with simulation is expected. The spinning sideband analysis results are summarised in Table 4-3. It is clear that the phosphorus nuclei have nearly axial symmetry, as expected, and the tensor components obtained from the three spinning sideband manifolds are equal (within experimental error). Note that it is difficult to distinguish between axially symmetric ($\eta = 0$) and near-axially symmetric systems ($\eta < 0.2$)
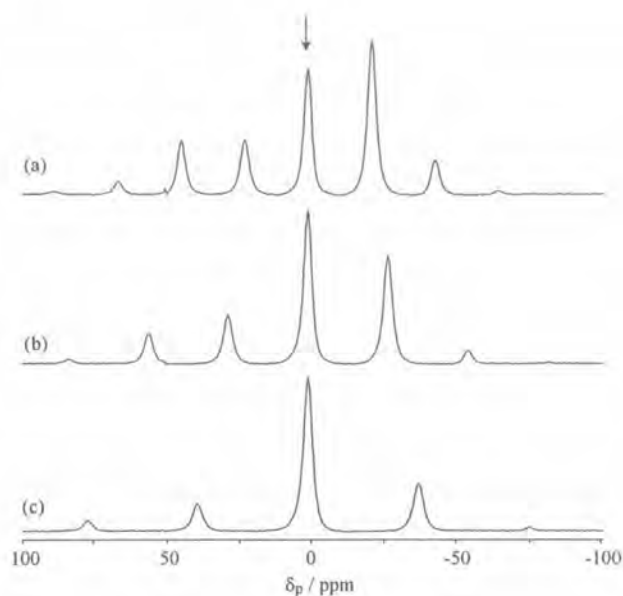
Figure 4-2 ^{31}P spectra of SnHPO$_3$ at different spin rates: (a) 1.8 kHz with 32 transients, (b) 2.2 kHz with 20 transients and (c) 3.1 kHz with 24 transients. The recycle delay is 300 s.

A Phosphorus-31 direct polarisation static spectrum with proton decoupling has been also recorded at 202.82 MHz. The anisotropy and asymmetry parameters have been derived using the STARS program [36]. The fit is illustrated in Figure 4-3. The results from this are ζ = -68.1 ± 0.5 ppm and η = 0.08 ± 0.01. The static lineshape fit is excellent, and the results are in good agreement with those from the spinning sideband analyses using SSB97 [12].
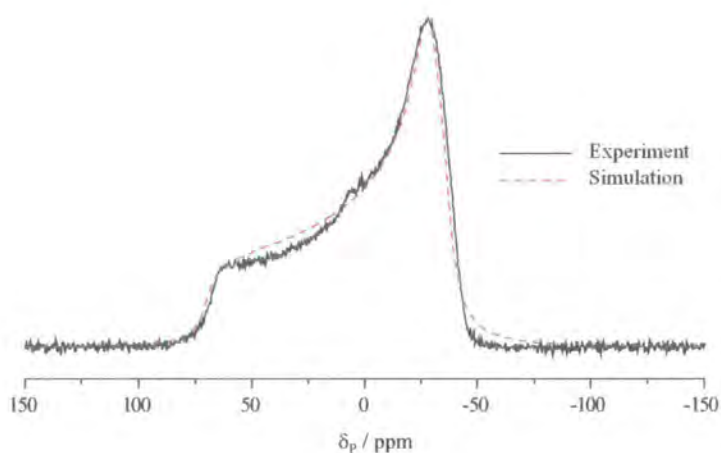
Figure 4-3 Comparison of the computed-fitted (using STARS) and experimental ^{31}P direct-polarisation spectra obtained at 202.28 MHz. Acquisition parameters were: recycle delay 300 s and number of transients 80. A 'line broadening' factor of 1600 Hz was applied to the simulated spectrum

Table 4-3 Results of spinning sideband analyses for ^{31}P spectra of SnHPO$_3$. The errors quoted are these given on a statistical basis the SSB97 computer program [12].

Spin rate / kHz	δ /ppm	Linewidth /Hz	σ_{11} - σ_{ref} /ppm	σ_{22} - σ_{ref} /ppm	σ_{33} - σ_{ref} /ppm	σ_{33} - σ_{iso} ζ /ppm	η
1.8	1.4	251	32 ± 2	32 ± 2	-69.1 ± 0.5	-67.7 ± 0.5	0.00 ± 0.06
2.2	1.4	256	32 ± 4	32 ± 4	-69.0 ± 0.6	-67.6 ± 0.6	0.00 ± 0.13
3.1	1.4	228	33 ± 4	33 ± 4	-69.6 ± 0.7	-68.2 ± 0.7	0.00 ± 0.12
average^a	1.4	245 ± 10	32 ± 1	32 ± 1	-69.2 ± 0.6	-67.8 ± 0.3	0.00 ± 0.05

^{a} The best combined estimate of the true value is given by $\overline{X}_{i,j,k} = \dfrac{\sum_i \left(X_i / \alpha_i^2 \right)}{\sum_i \left(1 / \alpha_i^2 \right)}$;

the standard error on the weighted mean is: $\dfrac{1}{\alpha_{\overline{X}_{i,j,k}}^2} = \dfrac{1}{\sum_i \alpha_{X_i}^2}$.

The proton-decoupled tin spectrum, obtained by using ramped-CP at 111.86 MHz, has a single centreband at −713.3 ppm, shown in Figure 4-4. The single centreband is indicated by the arrow. This implies that a single molecule exists in the asymmetric unit, again as expected from the crystal structure. The spinning sidebands in Figure 4-4 were analysed and the results are shown in Table 4-4. This indicates that tin nuclei are in a non-axially symmetric environment.
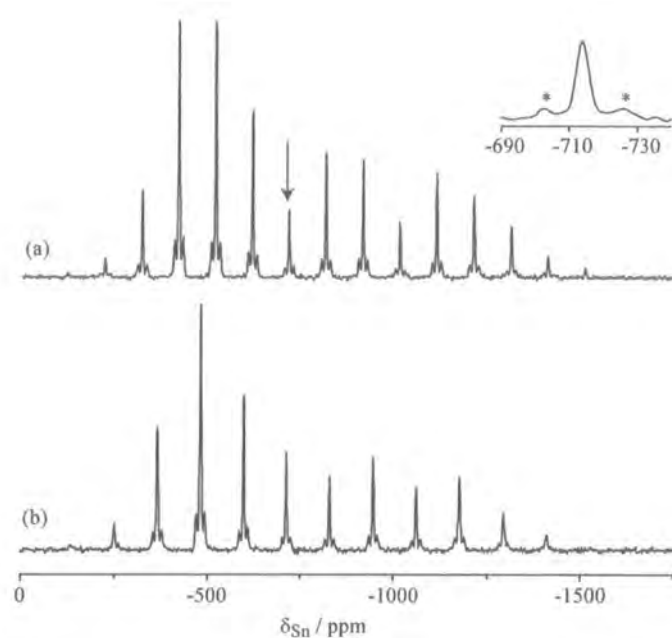
Figure 4-4 ^{119}Sn spectra of SnHPO$_3$ at different spin rates: (a) 11.0 kHz with 1156 transients, (b) 13.1 kHz with 1124 transients. For the key acquisition parameters of ^{119}Sn spectra, the contact time is 10 ms and the recycle delay is 60 s. The proton RF field strength over the ramp was in a range 62-83 kHz. The centreband is indicated by the arrow and the peaks marked with * in the expanded centreband region (top right) are the satellite peaks referred to the text.

Table 4-4 Shielding tensor data for SnHPO$_3$ from the ^{119}Sn experiment.

Spin rate /kHz	δ /ppm	Linewidth /Hz	$\sigma_{11} - \sigma_{ref}$ /ppm	$\sigma_{22} - \sigma_{ref}$ /ppm	$\sigma_{33} - \sigma_{ref}$ /ppm	ζ /ppm	η
11.0	-713.6	493	290 ± 5	423 ± 5	1427 ± 5	714 ± 5	0.19 ± 0.01
13.1	-713.3	499	291 ± 11	403 ± 11	1447 ± 6	734 ± 6	0.15 ± 0.03
average	-713.3 ± 0.2	496 ± 4	290 ± 5	420 ± 5	1435 ± 4	722 ± 4	0.19 ± 0.01

The NMR results are fully consistent with the structure above described, and also show that there is only one whole SnHPO$_3$ group present in the asymmetric unit.

The inset in Figure 4-4 shows the expanded centreband. Interestingly, there is one pair of satellite peaks present marked with * with apparent coupling constant, 2600 ± 200 Hz, which is a very large value. This splitting cannot be the result of coupling to ^{31}P and could be assigned to four-bond indirect coupling between the tin nuclei through oxygen atoms (see Figure 4-1). This coupling, which corresponds to ^{119}Sn-O-P-O-^{119}Sn or ^{117}Sn-O-P-O-^{119}Sn, is discussed in the sections 4.2.3 and 4.2.4.

Tin(II) hydrogen phosphate, SnHPO₄

The structures of tin(II) hydrogen phosphate and tin(II) phosphite are quite similar, since both which consist of infinite sheets [34]. The crystal structure of tin(II) hydrogen phosphate belongs to space group $P2_1/c$, and is presented in Figure 4-5. It shows that the sheets consist of SnO₃ groups fused with PO₄ groups, and they are closer together than those of SnHPO₃. SnO₃ trigonal pyramids and PO₄ tetrahedra are linked together at their corners. Each tin atom is coordinated by three phosphate groups. Two of the oxygen atoms of a PO₄ group are each coordinated with two tin atoms as well as the phosphorus atom. The remaining two oxygen atoms protrude into the spaces between sheets and are not closely coordinated to tin. These atoms are presumably involved in the hydrogen bonding which holds the sheets together. Although, it was not possible to determine the hydrogen position by X-ray studies, the hydrogen atom has been suggested to lie between sheets and to be involved in hydrogen bonding [34]. Thus, the distance between sheets is about an average distance for hydrogen-bonded phosphate groups, which is the closest interaction between the sheets.

(a)   (b)
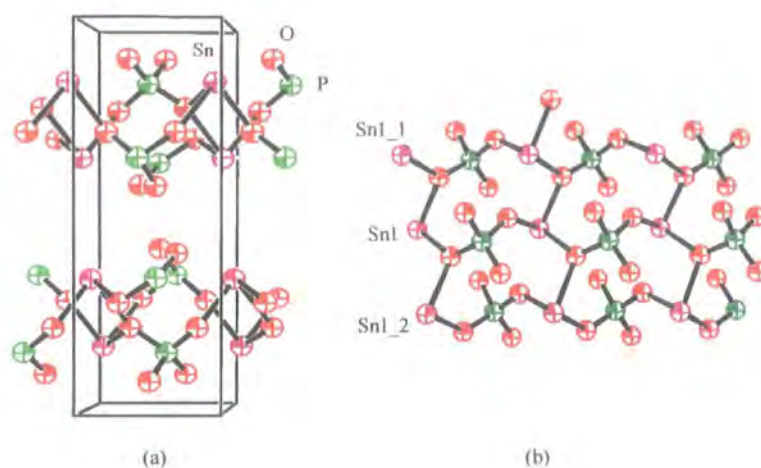
Figure 4-5 Crystal structure of SnHPO$_4$: (a) layers within a unit cell outline (b) the coordination of tin.

Figure 4-6 illustrates the proton-decoupled ^{31}P spectrum. The single centreband was found at -4.4 ppm. It indicates that there is only one phosphorus atom in the asymmetric unit, in agreement with the crystal structure. The spinning sideband analysis of Figure 4-6 has been performed and the results are displayed in Table 4-5. These show that the phosphorus nuclei are in a low symmetry environment.

There is an impurity in this compound, which leads to the peak at -0.3 ppm. This peak could arise from the existence of H$_3$PO$_4$, which was used in the synthesis of this compound. However, it was not possible to remove the impurity by rewashing this compound with ethanol and ether.
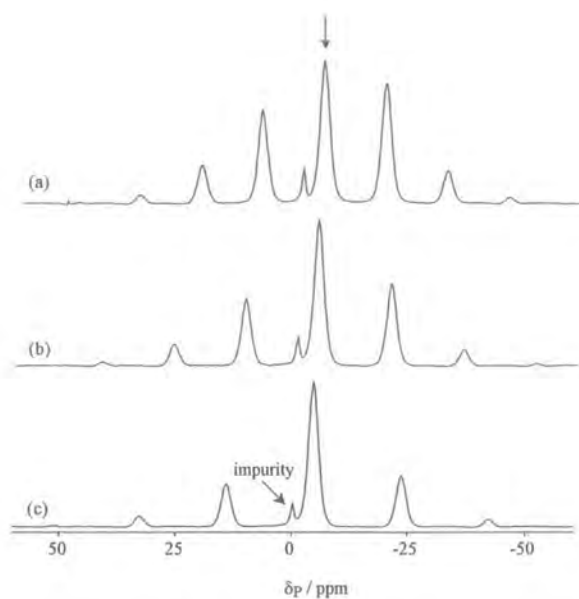
Figure 4-6 ^{31}P spectra of SnHPO$_4$ at different spin rates: (a) 1.1 kHz, (b) 1.3 kHz and (c) 1.5 kHz. Spectrometer operating conditions: The number of transients is 16; the recycle delay is 150 s.

Table 4-5 The ^{31}P shielding tensor data for SnHPO$_4$.

Spin rate / kHz	δ /ppm	Linewidth /Hz	σ_{11} - σ_{ref} /ppm	σ_{22} - σ_{ref} /ppm	σ_{33} - σ_{ref} /ppm	$\sigma_{33} - \sigma_{iso}$ ζ /ppm	η
1.1	-4.4	186	34.0 ± 0.4	8.3 ± 0.1	-28.4 ± 0.4	-33.0 ± 0.4	0.78 ± 0.00
1.3	-4.4	186	33.4 ± 0.5	8.7 ± 0.1	-28.2 ± 0.6	-32.8 ± 0.6	0.75 ± 0.01
1.5	-4.4	190	32.7 ± 0.8	8.6 ± 0.2	-27.4 ± 0.8	-32.0 ± 0.8	0.75 ± 0.01
average	-4.4	187 ± 3	33.6 ± 0.3	8.5 ± 0.1	-28.2 ± 0.3	-32.8 ± 0.3	0.75 ± 0.01
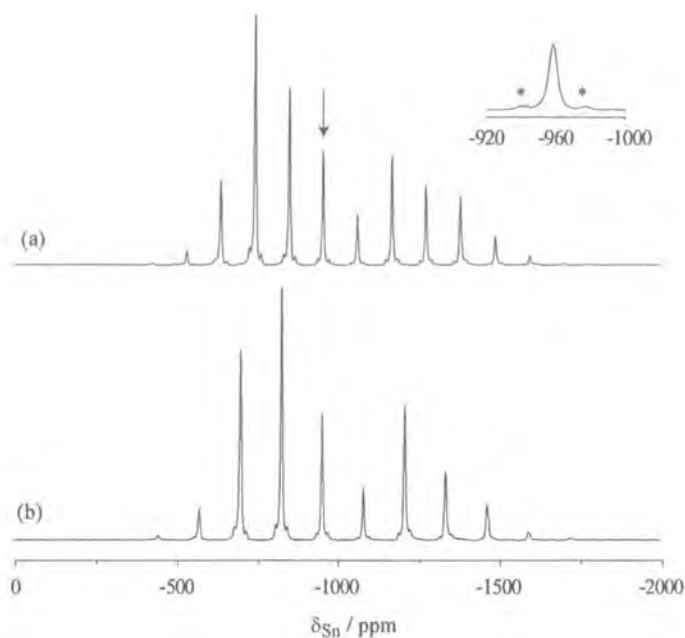
Figure 4-7 ^{119}Sn spectra of SnHPO$_4$ at different spin rates: (a) 11 kHz with 18308 transients, (b) 14 kHz with 20000 transients. For the key acquisition parameters of ^{119}Sn spectra, the contact time is 10 ms and the recycle delay is 1 s. The centreband is indicated by the arrow and the peaks marked with * are the satellite peaks on the centreband.

The proton-decoupled ^{119}Sn spectrum of this compound, is illustrated in Figure 4-7. A single centreband resonance is found at -959.8 ppm, indicating that only one tin atom is present in the asymmetric unit. Satellite peaks also appear in the tin spectrum, which can be seen easily at the positions of -939.4 and -975.9 ppm. The spinning-sideband intensities, including those of the $^{117/119}$Sn satellite peaks, have been analysed together to give information on the shielding tensors. The results are shown in Table 4-6. It is obvious that the anisotropy is relatively large and that the tin has a low symmetry environment.

The above NMR studies are fully consistent with the known crystal structure of tin(II) hydrogen phosphate.

Surprisingly, a very large indirect coupling constant has been found in this compound, 4151 ± 200 Hz, as shown in the expanded centreband in Figure 4-7. This result is discussed in section 4.2.4.

Table 4-6 Shielding tensor data for SnHPO$_4$ from the ^{119}Sn experiments.

Spin rate /kHz	δ /ppm	Linewidth /Hz	$\sigma_{11} - \sigma_{\text{ref}}$ /ppm	$\sigma_{22} - \sigma_{\text{ref}}$ /ppm	$\sigma_{33} - \sigma_{\text{ref}}$ /ppm	$\sigma_{33} - \sigma_{\text{iso}}$ ζ/ppm	η
11.0	-957.7	566	612 ± 9	704 ± 9	1554 ± 5	597 ± 5	0.15 ± 0.03
14.0	-959.8	547	600 ± 9	718 ± 8	1551 ± 7	594 ± 7	0.20 ± 0.03
average	-959.8 ± 1.5	556 ± 12	606 ± 6	712 ± 6	1553 ± 4	596 ± 4	0.18 ± 0.02

Tin(II) diphosphate, Sn$_2$P$_2$O$_7$

In general, an isolated molecule of tin(II) diphosphate consists of Sn^{2+} cations and P$_2$O$_7^{4-}$ anions, in which divalent tin may be bridged by phosphate groups. Note that Sn$_2$P$_2$O$_7$ is very stable at room temperature and exists up to 700°C; above this temperature, tin(II) will be oxidised to tin(IV) and produce SnP$_2$O$_7$ and SnO$_2$ [37]. Unfortunately, information concerning tin(II) diphosphate is limited and a crystal structure is not available. Therefore the structural information from NMR is very important.

The ^{31}P spectra obtained with a single-pulse experiment at 81.01 MHz for tin diphosphate are presented in Figure 4-8. The two peaks at -11.7 and -15.6 ppm observed in this compound show that the asymmetric unit contains two atoms of phosphorus. The peak at -4.4 ppm is not expected and presumably arises from an impurity. The tin(II) diphosphate was prepared from SnHPO$_4$ [37]. A comparison of this peak and its sidebands at a low spin rate (1.4 kHz) with the ^{31}P spectrum of SnHPO$_4$ at a spin rate of 1.5 kHz is displayed in Figure 4-8 (a). The peak position of the centreband for the Sn$_2$P$_2$O$_7$ impurity is nearly the same as that for SnHPO$_4$, although the sideband intensities are different. Nevertheless, this clearly indicates that the -4.4 ppm peak may be assigned to the existence of SnHPO$_4$ in the Sn$_2$P$_2$O$_7$ sample.
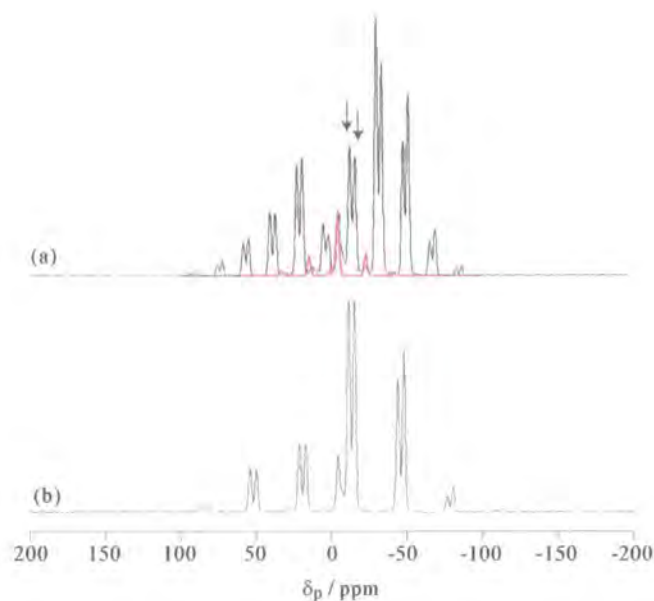
Figure 4-8 ^{31}P spectra of $Sn_2P_2O_7$ at different spin rates: (a) 1.4 kHz., (b) 2.6 kHz. (a) shows a comparison of the ^{31}P $Sn_2P_2O_7$ spectrum (straight black line) at a spin rate of 1.4 kHz and the ^{31}P $SnHPO_4$ spectrum (dashed red line) at a spin rate of 1.4 kHz. Spectrometer operating conditions: The recycle delay is 300 s; the number of transients is (a) 16, (b) 12.

A number of spinning sidebands are observed in Figure 4-8, and at the spinning speeds of 1.4 and 2.6 kHz they allow the shielding components to be extracted. The results are shown in Table 4-7. The deconvoluted intensity data were used to determine the principal components using SSB97. Since there is the impurity peak overlap in the centreband, it is likely that the data are not very accurate. This can be apparently seen by the fact that the differences in tensor components (especially at the isotropic shift of -15.6 ppm) between two spinning sideband manifolds are not equal (within experimental error). It is certain that the shielding tensors of the two different nuclei are not axially symmetry. It is, however, clear that the peak at $\delta_P = -11.7$ ppm has a somewhat smaller anisotropy than that of the $\delta_P = -15.6$ ppm resonance, though the situation regarding the asymmetry is less obvious.

Table 4-7 The shielding tensors of ^{31}P for $Sn_2P_2O_7$.

Spin rate /kHz	δ /ppm	Linewidth /Hz	$\sigma_{11} - \sigma_{ref}$ /ppm	$\sigma_{22} - \sigma_{ref}$ /ppm	$\sigma_{33} - \sigma_{ref}$ /ppm	$\sigma_{33} - \sigma_{iso}$ ζ /ppm	η
1.4	-11.6	200	56.7 ± 0.9	40.1 ±0.9	-62.1 ± 0.8	-73.7 ± 0.7	0.22 ± 0.02
	-15.4	174	68.1 ± 1.1	42.3 ±0.8	-64.2 ± 1.3	-79.6 ± 1.3	0.32 ± 0.02
2.6	-11.7	200	59.8 ± 1.2	38.4 ±1.1	63.1 ± 0.8	-74.8 ± 0.8	0.29 ± 0.03
	-15.7	171	60.9 ± 5.9	52.1 ±5.9	-65.8 ± 0.5	-81.6 ± 0.5	0.11 ± 0.14
average	-11.7 ± 0.1	200	57.8 ± 0.7	39.4 ±0.7	-62.6 ± 0.6	-74.2 ± 0.5	0.24 ± 0.02
	-15.6 ± 0.2	173 ± 2	67.8 ± 1.1	42.6 ±1.1	-65.6 ± 0.5	-81.3 ± 0.5	0.32 ± 0.08
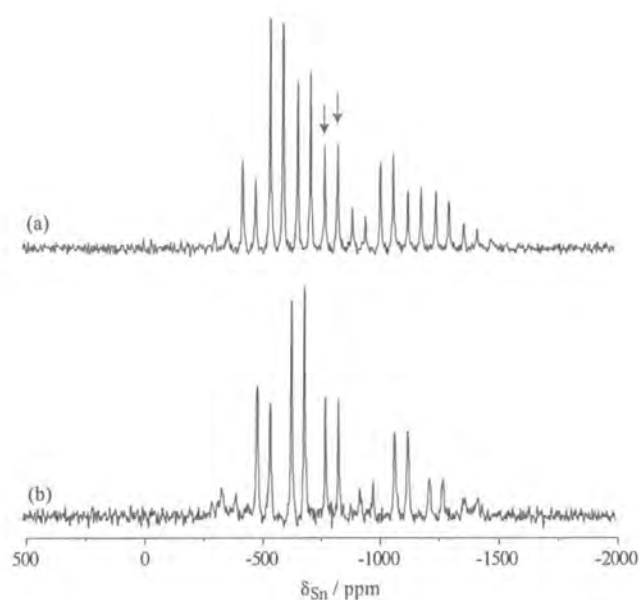
Figure 4-9 ^{119}Sn spectra of $Sn_2P_2O_7$ at different spin rates: (a) 13.3 kHz with 552 transients, (b) 16.3 kHz with 212 transients. The recycle delay is 300 s. The centrebands are indicated by arrows.

Figure 4-9 displays the tin-119 spectra, obtained by direct polarisation for this compound, which consists of a double peak at the centreband. The centrebands are at -781.2 and -836.2 ppm, found by varying the spin rates. This implies that the asymmetric unit contains two tin atoms. Spinning sideband analysis was carried out for spectra spinning at different speeds, and the averaged results and the reproducibility are given in Table 4-8. Due to the low signal-to-noise ratio of tin spectra from both spin rates, there are large experimental errors. Nevertheless, the anisotropy of the peak at -781.2 ppm is consistently slightly larger than that for the -836.2 ppm resonance. It is also revealed that both types of tin atoms are in an axial symmetry or nearly axial environment.

Table 4-8 The ^{119}Sn shielding tensors for $Sn_2P_2O_7$.

Spin rate /kHz	δ /ppm	Linewidth /Hz	$\sigma_{11} - \sigma_{ref}$ /ppm	$\sigma_{22} - \sigma_{ref}$ /ppm	$\sigma_{33} - \sigma_{ref}$ /ppm	$\sigma_{33} - \sigma_{iso}$ ζ /ppm	η
13.3	-780.7	525	430 ± 23	447 ± 23	1464 ± 8	684 ± 8	0.02 ± 0.06
	-835.8	539	463 ± 20	557 ± 20	1486 ± 8	651 ± 8	0.14 ± 0.06
16.3	-781.7	495	428 ± 27	428 ± 27	1488 ± 9	707 ± 9	0.00 ± 0.08
	-836.6	568	503 ± 25	503 ± 25	1504 ± 7	667 ± 7	0.00 ± 0.07
average	-781.2 ± 0.7	510 ± 21	429 ± 18	439 ± 18	1475 ± 6	694 ± 6	0.01 ± 0.05
	-836.2 ± 0.6	553 ± 20	479 ± 16	536 ± 16	1496 ± 5	660 ± 5	0.08 ± 0.05

Tin(II) oxalate, SnC_2O_4

The principal feature of tin(II) oxalate is that it contains divalent tin and oxalato groups. The oxalato groups are located on a symmetry centre [38]. Two tin atoms are bonded to the oxalato groups through one oxygen on each carbon atom. As a result, there are infinite chains $(SnC_2O_4)_n$. A schematic representation of the structure for SnC_2O_4 is shown in Figure 4-10.
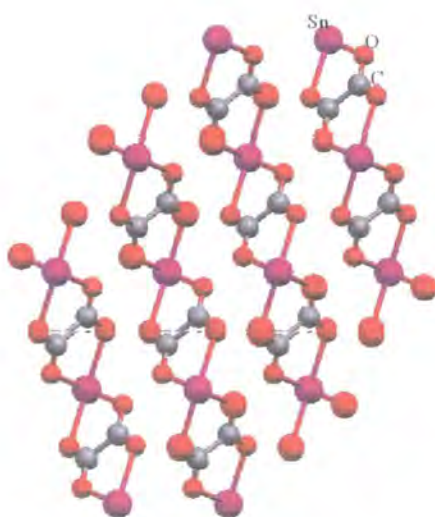
Figure 4-10 Crystal structure of SnC_2O_4.

Only one ^{119}Sn peak is observed by a single-pulse experiment at 74.56 MHz, as shown in Figure 4-11. The chemical shift of tin is -878.8 ppm. This reveals that only one tin exists in the asymmetric unit of SnC_2O_4 which is clearly consistent with the X-ray data. Analysis of the spinning sideband manifold of Figure 4-11 shows that tin has low but non-zero asymmetry. The results for the shielding tensor are summarised in Table 4-9.
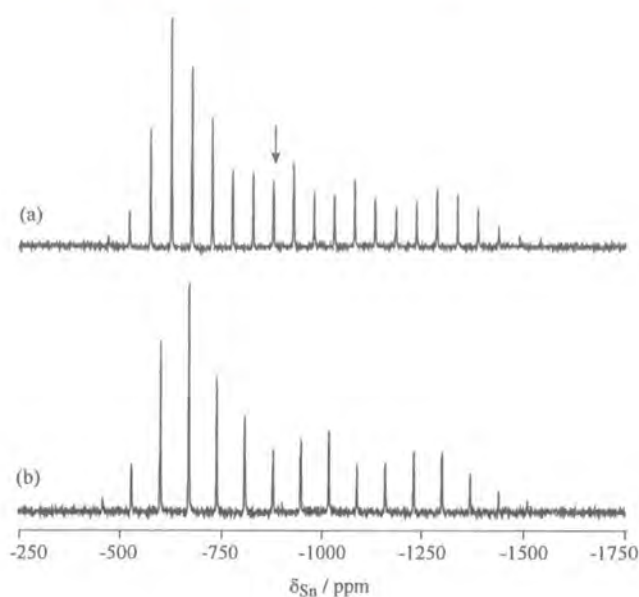
Figure 4-11 ^{119}Sn spectra of SnC_2O_4 at different spin rates: (a) 3.8 kHz with 72 transients, (b) 5.2 kHz with 48 transients. The recycle delay is 300 s. The centreband is indicated by the arrow.

Table 4-9 Shielding tensor data for SnC_2O_4 from ^{119}Sn spectra.

Spin rate /kHz	δ /ppm	Linewidth /Hz	$\sigma_{11} - \sigma_{ref}$ /ppm	$\sigma_{22} - \sigma_{ref}$ /ppm	$\sigma_{33} - \sigma_{ref}$ /ppm	$\sigma_{33} - \sigma_{iso}$ ζ /ppm	η
3.8	-878.7	205	530 ± 5	633 ± 5	1472 ± 6	594 ± 6	0.17 ± 0.01
5.2	-878.9	195	516 ± 5	643 ± 4	1476 ± 6	598 ± 6	0.21 ± 0.01
average	-878.8 ± 0.1	200 ± 7	523 ± 4	639 ± 4	1474 ± 4	596 ± 4	0.18 ± 0.01

The ^{13}C spectrum (Figure 4-12) was studied under the conditions of single pulse-and-acquire operation with very long recycle delay 300 s. A spectrum with poor signal-to-noise ratio was obtained. There are two reasons to explain this: (1) there are only non-protonated carbons in this compound, so it is not feasible to enhance the sensitivity from proton magnetisation via cross-polarisation ; (2) there is a background problem from the rotor (Teflon containing carbon). Nevertheless, after subtraction the background signal, a

very low intensity peak at 169 ppm is observed, which can be assigned to the oxalato group. This suggests that only one type of carbon exists in the asymmetric unit, in agreement with the crystal structure.
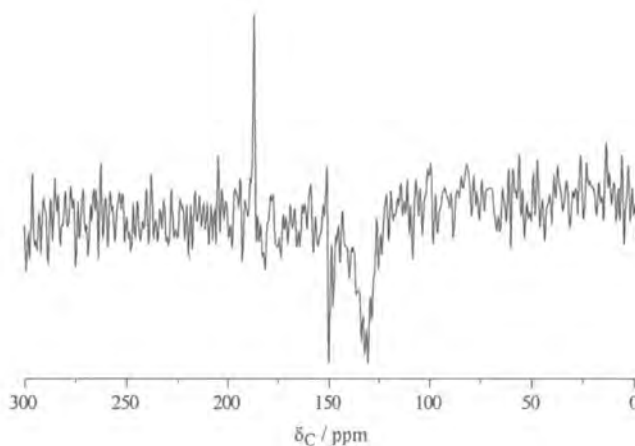
Figure 4-12 ^{13}C spectrum of SnC_2O_4 at 50.32 MHz A single pulse experiment was employed at a spin rate of 5 kHz. Spectrometer operating conditions: The number of transients is 252; the recycle delay is 300 s. A broad negative signal probably arises from the background signal after subtraction.

Calcium tin (II) ethylene diamine tetraacetate, CaSnEDTA

For this compound, ethylene diamine tetraacetate anions (EDTA^{4-}) form metal complexes of both tin(II) and calcium(II) cations. Note that the EDTA anion is $(^-CO_2CH_2)_2NCH_2CH_2N(CH_2CO_2^-)_2$. In solution-state ^{1}H NMR studies [39], it has been reported that the EDTA anions act mainly as penta- or hexadentate ligands towards metallic ions, forming ionic bonds with the four oxygens of the carboxylate groups rather than covalent bonds to the nitrogens. (The structure of CaSnEDTA has not yet been reported.)

In general, the ^{13}C spectrum for uncomplexed EDTA, H$_4$-EDTA [40], shows two peaks of equal intensity for carboxylate resonances and three different methylene peaks. The two separate carboxylate peaks are attributed to the zwitterionic nature of this species, in

which two nitrogen atoms have been protonated, leaving protonated and unprotonated carboxyl groups as shown below.
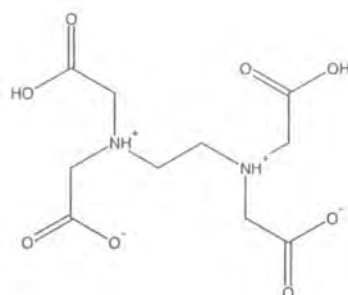
Additionally, investigation of the ^{13}C isotropic chemical shifts by solid-state NMR for EDTA-metal complexes has been reported [40,41]. The carbonyl resonances are found between 169 to 180 ppm, the acetate methylene resonances occur between 54 to 65 ppm and the ethylenic methylenes are between 45 to 54 ppm.
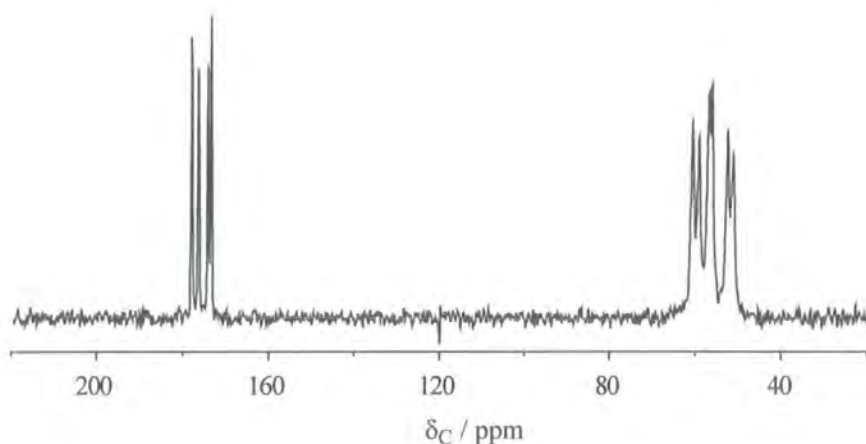
Figure 4-13 ^{13}C CP/MAS spectrum of CaSnEDTA at 75.4 MHz, obtained with spinning at 9.2 kHz. Acquisition parameters were: recycle delay 30 s, contact time 5 ms, and number of transients 320.

The proton-decoupled ^{13}C CP/MAS spectrum for CaSnEDTA at a spin rate of 9.2 kHz is presented in Figure 4-13. Four carboxyl resonances are observed at 174.0, 174.7, 176.9 and 178.6 ppm. Six methylene peaks are obtained; the central methylene groups probably

give rise to the peaks at 51.7 and 53.0 ppm, whereas the acetate methylene peaks are at 56.6, 57.3, 59.4 and 61.1 ppm. The values of the chemical shifts are consistent with those reported [40,41] from solid-state NMR for EDTA-metal complexes (e.g. Ca_2EDTA and $MgNa_2EDTA \cdot xH_2O$).

Although, no crystal structure has been reported for this compound, the multiple resonances in the ^{13}C spectrum reveal the presence of one complete EDTA anion (or two half-anions) in the crystallographic asymmetric unit. Alam and Assink [41] report that carbonyl ^{13}C shifts at 179–180 ppm characterise compounds with co-ordination by nitrogen to the metal, whereas shifts in the range 170–174 ppm are normal for systems without such co-ordination (although in these cases there is not full neutralisation of the acetate groups). Clearly solid SnCaEDTA gives intermediate values for the carboxyl chemical shifts, perhaps because of the overall structural environment.

The proton-decoupled ^{119}Sn spectra were recorded using ramped-CP at 111.76 MHz as exhibited in Figure 4-14. The tin has only one site at -683.3 ppm. The spectrum at a spin rate of 14.2 kHz has a relatively poor signal-to-noise ratio; consequently, the error in measuring the intensities is rather large and this has an effect on the derived tensor parameters. Iterative fitting of the sideband manifolds to obtain tensor components (Table 4-10) showed that the asymmetry parameter is 0.20 ± 0.02. Thus, the ^{119}Sn shielding tensor is not axially symmetric, though the asymmetry parameter is low and perhaps not statistically significant.
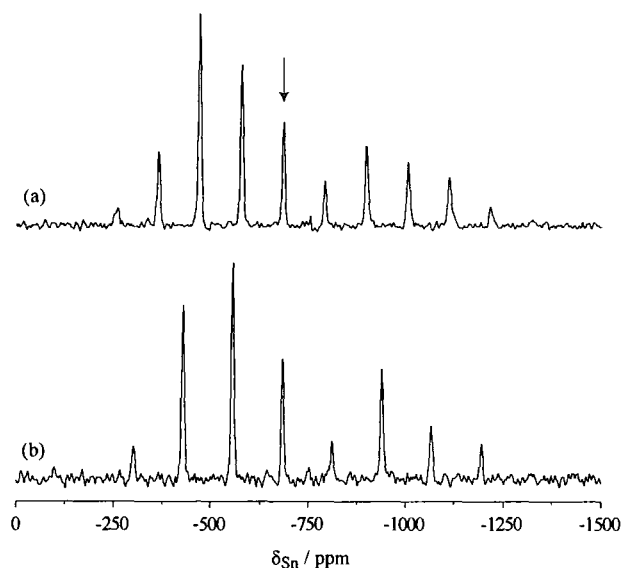
Figure 4-14 ^{119}Sn spectra of CaSnEDTA at different spin rates: (a) 11.9 kHz with 2000 transients, (b) 14.2 kHz with 668 transients. The key acquisition parameters of the ^{119}Sn spectra are: The contact time is 10 ms and the recycle delay is 30 s. The centreband is indicated by an arrow.

Table 4-10 Shielding tensor data for CaSnEDTA from ^{119}Sn spectra by use of the SSB97 program.

Spin rate /kHz	δ /ppm	Linewidth /Hz	$\sigma_{11} - \sigma_{ref}$ /ppm	$\sigma_{22} - \sigma_{ref}$ /ppm	$\sigma_{33} - \sigma_{ref}$ /ppm	$\sigma_{33} - \sigma_{iso}$ ζ /ppm	η
12.0	-683.2	713.9	329 ± 7	452 ± 6	1269 ± 6	585 ± 6	0.21 ± 0.02
14.2	-683.4	661.9	364 ± 26	421 ± 26	1263 ± 9	580 ± 9	0.09 ± 0.09
average	-683.3 ± 0.1	690 ± 15	331 ± 7	450 ± 6	1267 ± 5	583 ± 5	0.20 ± 0.02

The fitting of the spinning sidebands using the STARS program [36] is shown in Figure 4-15. The tin spectrum at a spin rate of 11.9 kHz was chosen for a comparison because it has a better signal-to-noise ratio than that for the higher spin rate. A successful fit is achieved and the parameters obtained are $\zeta = 593$ ppm and $\eta = 0.30$. These results are reasonably consistent with the SSB97 data (Table 4-10).
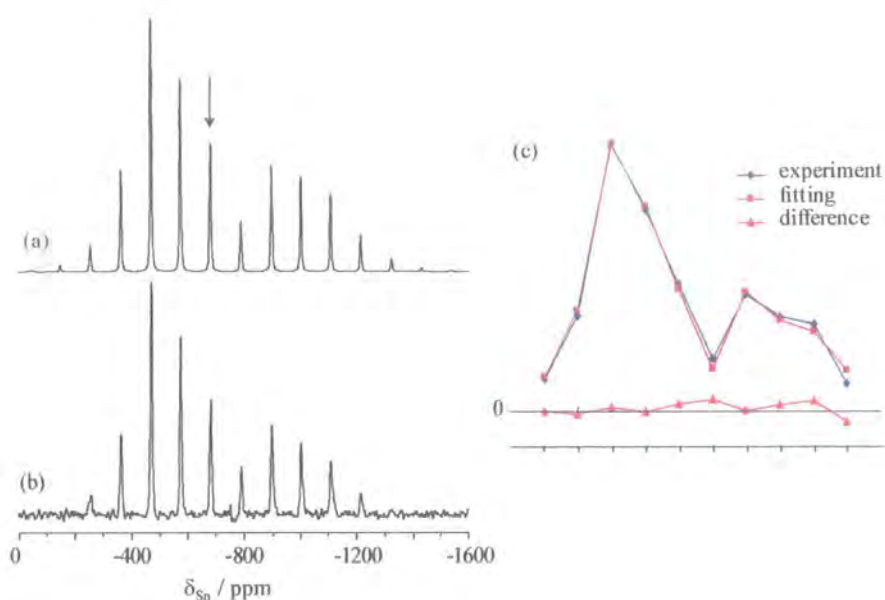
Figure 4-15 ^{119}Sn-{^{1}H} spinning sideband pattern for CaSnEDTA at a spin rate of 11.9 kHz. (a) Computed fit (using the STARS program) and (b) experimental spectra at 111.76 MHz. (c) The integrals and the difference between experimental and simulated values are plotted to the right, the horizontal dashed line being at zero level.

As shown above, clearly, there is no characteristic splitting arising from the coupling between ^{119}Sn and ^{14}N. Therefore, it implies that tin-119 in CaSnEDTA does not involve nitrogen coordination, which is consistent with the conclusion made by Ref. [41] regarding to the ^{13}C chemical shift for carbonyl group (see above).

Tin(II) sulphate, SnSO$_4$

The crystal structure of SnSO$_4$ has been reported [42]. It consists of sulphate groups and layers with tin(II) atoms co-ordinated by three oxygen atoms; there are three Sn-O bonds of 2.25, 2.27 and 2.27 Å, and pyramidal bond angles of 79.0, 77.1 and 77.1°. The structure is shown in Figure 4-16.

A single centreband at -1262.6 ppm in the direct-polarisation [119]Sn spectrum was observed for tin(II) sulfate, as shown in Figure 4-17. This indicates that there is only one type of tin in the crystallographic asymmetric unit. The analysis of the spinning sideband manifold reveals that the tin nuclei are in low symmetric environments (see Table 4-11). These results are in agreement with the published crystal structure [42]. No satellite peaks were seen for this compound.

(a)   (b)
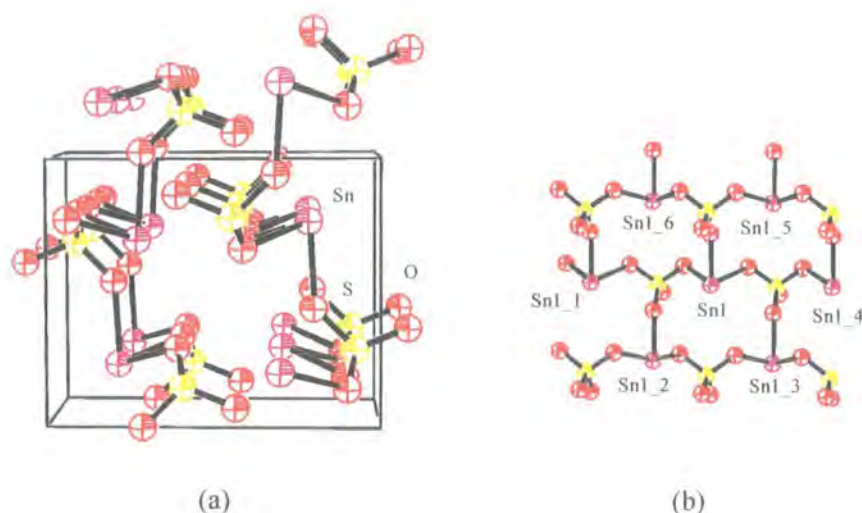
**Figure 4-16** Crystal structure of SnSO$_4$: (a) within a unit cell outline (b) the coordination of tin.
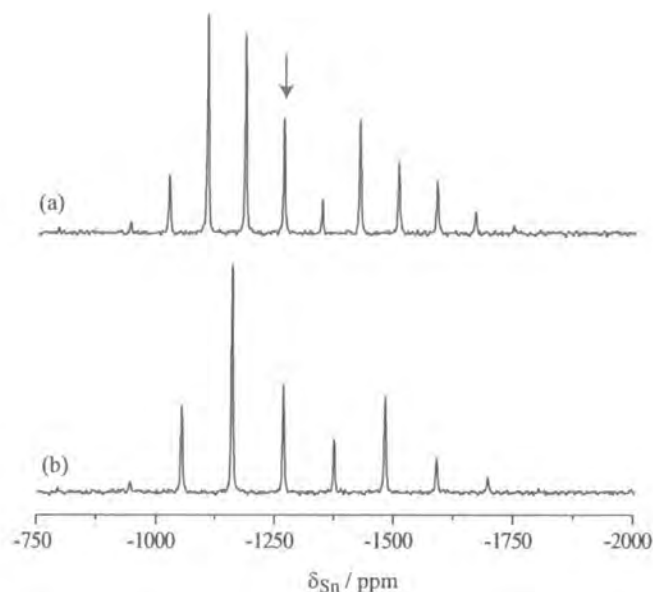
Figure 4-17 ^{119}Sn spectra of $SnSO_4$ at different spin rates: (a) 12.0 kHz with 264 transients, (b) 14.2 kHz with 260 transients. The recycle delay is 300 s. The centreband is indicated by the arrow.

Table 4-11 Shielding tensor data for $SnSO_4$ from ^{119}Sn spectra.

Spin rate /kHz	δ /ppm	Linewidth /Hz	$\sigma_{11} - \sigma_{ref}$ /ppm	$\sigma_{22} - \sigma_{ref}$ /ppm	$\sigma_{33} - \sigma_{ref}$ /ppm	$\sigma_{33} - \sigma_{iso}$ ζ /ppm	η
9.0	-1262.1	330	1030 ± 15	1073 ± 15	1682 ± 2	420 ± 2	0.10 ± 0.07
12.0	-1263.6	310	1031 ± 15	1083 ± 15	1677 ± 3	414 ± 3	0.13 ± 0.07
13.0^a	-1266.6	300	1059 ± 9	1059 ± 9	1681 ± 2	414 ± 2	0.00 ± 0.04
average	-1264.1 ± 2.3	313 ± 15	1047 ± 7	1066 ± 7	1679 ± 1	416 ± 1	0.05 ± 0.03

^{a} New values of the shielding tensors were obtained by re-running the spectrum from a new sample of $SnSO_4$ (the same company as used for the previous one).

4.2.2 Comparison of the ^{119}Sn shielding anisotropies

The shielding anisotropies for five of the six compounds (except $SnSO_4$) in the present work are in a relatively narrow range, 583–722 ppm. In the cases of $SnHPO_3$, $SnHPO_4$ and SnC_2O_4 this may be linked to the layer-type structures which all three possess. As remarked above, only a small number of tin(II) compounds have had their shielding tensors measured. These are listed [22-29] in Table 4-12. With the exception of the two-coordinate systems, they span a similar range, 213–929 ppm. No low values have been measured, in contrast to the situation for tin(IV) compounds. This is presumably because tin(IV) environments are likely to be tetrahedral, allowing a high degree of electronic symmetry when the ligands are similar.

Table 4-12 Tin-119 shielding tensor data for tin(II) compounds.

Compound	ζ /ppm	η	Reference
SnO	675	0.1	[22]
$[H_{\underline{n}}B(pz)_{4-n}]_mSnCl_{2-m}$, n= 0,1 ,2; m=1, 2; pz= pyrazolyl ring, [Poly(pyrazolyl)borate complexes of tin(II)]	320-695	ca. 0.2	[23]
$Sn_2P_2S_6$ (Tin hexathiohypodiphosphate polymorphs)	213 329	0.69 0.18	[24]
SnS	384	Not given	[25]
Two-coordinate low-valent tin compounds $(SnXC_6H_3-2,6-trip_2)$	1794-2532	Not given	[26]
$SnNb_2O_6$ (Tin niobate)	929	0.15	[27]
$BaSnF_4$	593	0.0	[28]
$R_2Sn=SnR_2$, R = $(Me_3Si)_2CH)$	900	0.3	[29]

4.2.3 Investigation the satellite peaks of ^{119}Sn

The small doublet surrounding each sideband for $SnHPO_3$ and $SnHPO_4$ is likely to originate from an indirect J-coupling, which is the interaction between two nuclei through bond. However, the coupling constants are rather large. This is unusual for such long-range (e.g. 4-bond) couplings, which in general give small coupling constants. (Note that, generally, the shorter the bonding path, the larger the coupling.) Nevertheless, (as described in the introduction) it is not totally clear whether this coupling is homonuclear (^{119}Sn/^{119}Sn) or heteronuclear (^{117}Sn/^{119}Sn) or both. Therefore, it is desirable to have an experimental technique to clarify the origin of the satellites.

In this section, the examination the satellite peaks of ^{119}Sn (as shown in Figure 4-4 and Figure 4-7) have been studied using the CPMG pulse sequence [43,44] and point-by-point measurement with a single Hahn echo for each refocusing time. A comparison of the calculated satellite intensities from the tin's nearest neighbours with the experimental results has been also done.

Spin-echo experiments

The signal decay in simple spin-echo experiments is modulated only by homonuclear J-coupling, whereas heteronuclear J-coupling is refocused. If the coupling is due to homonuclear interactions, the time domain signal will be modulated by the J-coupling. On the other hand, no oscillation will be observed if the coupling is purely heteronuclear.

A rotation-synchronised CPMG experiment was performed. The sequence described here was expected to remove line broadening mechanisms. The MAS was carried out to eliminate direct dipolar interactions, proton decoupling was applied in order to assist in removal of heteronuclear (H, Sn) dipolar interactions, ramped-CP was employed to increase the efficiency of cross-polarisation, and the CPMG sequence was required to remove sources of inhomogeneous line broadening.

The pulse sequences used for investigation the splitting are illustrated in Figure 4-18. The rotation-synchronised CPMG sequence (Figure 4-18 (a)) is based on the Carr-Purcell-Meiboom-Gill experiment, with the addition of ramped-CP and proton decoupling. It was carried out with the spacing of the 180° pulses being exactly one rotor period. This requires measurement of the spinning speed very accurately, which was done by averaging the spacing from the spinning sidebands. The centreband was exactly on resonance. The number of data points acquired was typically the maximum possible without risking probe arcing, (the maximum acquisition time under full power proton decoupling was 100 ms).
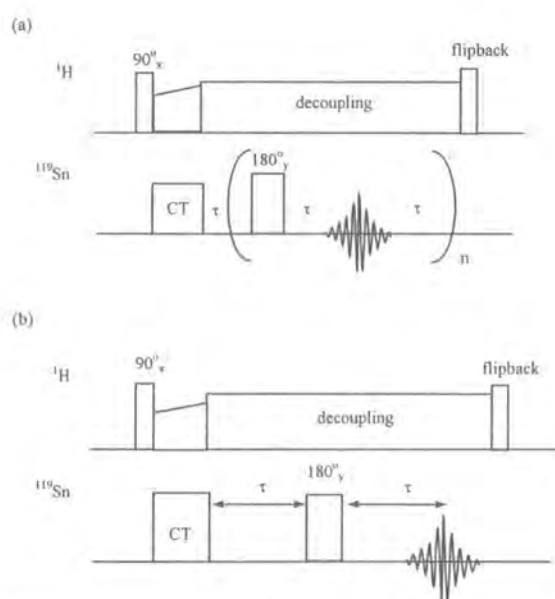
Figure 4-18 Pulse sequences: (a) rotor-synchronised CPMG sequence with ramped-CP and proton decoupling; (b) a corresponding simple Hahn-echo.

The results of a Fourier transformation following pulse sequence (a) (see Figure 4-18) are illustrated in Figure 4-19. The linewidths obtained using this technique are 13.5 and 14.3 Hz for $SnHPO_3$ and $SnHPO_4$, respectively. The significantly narrowed linewidths are much less those in the normal CP/MAS spectra (556 and 496 Hz for $SnHPO_3$ and $SnHPO_4$ respectively). Therefore, it is of interest to explore the intrinsic linewidths of tin-119 using a simple Hahn echo experiment. This experiment has been taken into account to compare the results of the linewidths and also to investigate the satellite peaks

since there is no clear evidence of satellite lines using rotation-synchronised CPMG (see Figure 4-19).
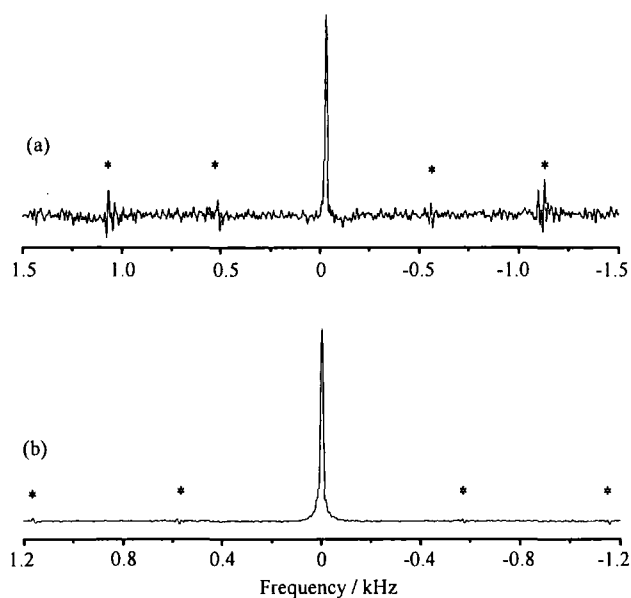
Figure 4-19 ^{119}Sn CPMG MAS spectra of (a) SnHPO$_3$ using 1644 transients, 60 s recycle delay and 10 ms contact time at a spin rate of 14 kHz, (b) SnHPO$_4$ using 65368 transients, 1 s recycle delay and 10 ms contact time at a spin rate of 14 kHz. The asterisks indicate digital artifacts.

More reasonable linewidths (compared to the above results), 78 Hz for SnHPO$_3$ and 51 Hz for SnHPO$_4$, have been obtained using single Hahn echoes with varying refocusing time. The pulse sequence is displayed in Figure 4-18 (b). Adjusting both pulse duration (π pulse) and resonance offset has been done carefully. It is clear that heteronuclear J-coupling (^{117}Sn-^{119}Sn) is refocused since the results from the Fourier transformation (Figure 4-20) show only single peaks. The measured linewidths correspond to values of T_2 which are 4.1 and 6.2 ms for SnHPO$_3$ and SnHPO$_4$, respectively.
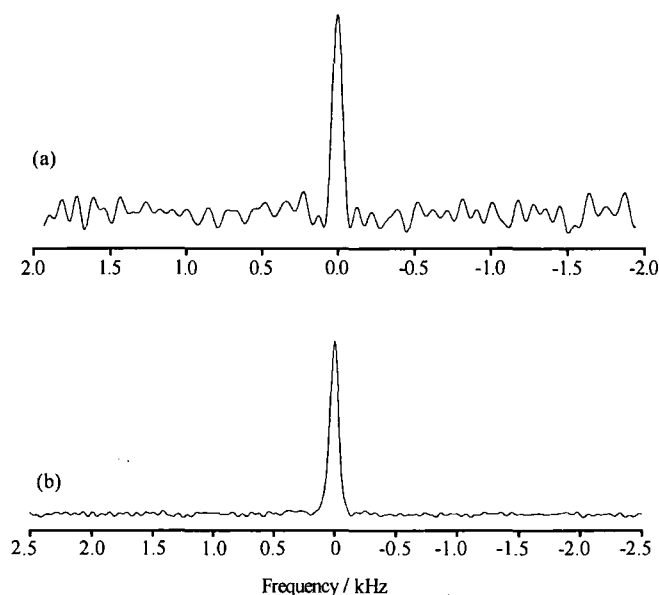
Figure 4-20 Fourier transformation of the maximum echo ^{119}Sn intensities as a function of the refocusing time, 2τ, obtained using single Hahn echos: (a) SnHPO$_3$ using 40 transients, 60 s recycle delay and 10 ms contact time at a spin rate of 15.5 kHz, (b) SnHPO$_4$ using 600 transients, 1 s recycle delay and 10 ms contact time at a spin rate of 15.2 kHz.

Consequently, the satellites seen from both SnHPO$_3$ and SnHPO$_4$ originate from heteronuclear J-coupling (^{117}Sn/^{119}Sn). However, it should be noted that, in principle, there is a network of coupled tin nuclei rather than isolated spin systems, so that second-order effects can be presented to complicate the situation.

Note that there is no clear explanation for the dissimilarity of linewidths between CPMG and simple Hahn echoes (see above) in both SnHPO$_3$ and SnHPO$_4$.

4.2.4 Discussion of Sn, Sn coupling

The values of Sn, Sn coupling constants found for both $SnHPO_3$ and $SnHPO_4$ are very large when we consider the number of chemical bonds separating the nuclei (within the layers) of 4 and 2 respectively. It should be noted that in organotin compounds it is possible to observe long-range couplings. Values of $^4J(SnSn)$ have been reported from solution-state experiments in the range 20-130 Hz [3,4]. However, these data are of limited value with respect to conclusions regarding the structure and the bonding situation. So far, one interesting case of four-bond tin-tin coupling, of 1611 Hz, have been found [45] for 3-substituted-(X)bicyclo[1.1.1]pent-1-yltrimethylstannanes (X = $SnMe_3$). This very large coupling constant has been explained by the significant through-space bridgehead-bridgehead interactions.

In the case of the phosphate, the nearest-neighbour tin atoms within a layer are separated by only two chemical bonds through an oxygen atom, Sn-O-Sn, as shown in Figure 4-5. The coupling is substantially larger for $SnHPO_4$ than in $SnHPO_3$, as might be expected due to the number of atoms separating the tin nuclei, but it is nevertheless unusually large. Scalar two-bond coupling in various organotin compounds has been studied from solution-state NMR experiments and the magnitude of $^2J(Sn-O-Sn)$ has been reported, generally corresponding to 100-1000 Hz [4,46]. As is known from solution-state NMR studies, the coupling constant depends strongly on the organic ligand, and correlates roughly with the Sn-O-Sn angle [47]. The smaller the Sn-O-Sn bond angle, the smaller is the corresponding value of the coupling, and the largest value is found for a linear Sn-O-Sn arrangement. However, the largest Sn-O-Sn bond angle is only 111° in $SnHPO_4$.

Furthermore, a few Sn-O-Sn indirect couplings have been found in solid-state NMR, from several tens to 950 Hz [48-51]. In some of these cases, the reported values are for $\lvert J\ (^{117}Sn,\ ^{119}Sn)\rvert$ [51,52]. The strongest indirect coupling, $\lvert J\ (^{117}Sn,\ ^{119}Sn)\rvert$ of 8300 Hz, was discovered in SnO [22]. However, in this case the authors attributed the

magnitude of the coupling constant to possible bonding between tin atoms in adjacent layers of the structure, which they based their conclusions on the satellite intensities[1]. A marked s-character in the bonding is required, involving weakly-localised 5s orbitals occupying the top of the valence band for SnO. It is noteworthy that the coupling for SnO_2 is small [17,53] (presumably because all the relevant electrons are involved in formal bonding). Effectively, this interpretation involves through-space interactions, but corresponds, in another view, to ^1J. A value for a direct Sn=Sn double bond, $|J(^{117}Sn, ^{119}Sn)| = 1340 \pm 10$ Hz, has been reported [29] for a solid-state dimeric structure $R_2Sn=SnR_2$, R = $(Me_3Si)_2CH$. However, the Sn=Sn bond is unusual in type and is relatively weak since the bond strength is at least a factor of 2 less than that for typical Sn-Sn bond.

Can a similar explanation be considered for $SnHPO_3$ or $SnHPO_4$ or both? A second question to address is the absence of satellite peaks for the oxalate and sulphate. Table 4-13 shows the relevant structural data. In order to explain the puzzling satellite peaks, the number of neighbouring tin atoms and the intensity of the satellite peaks have been taken into account first. The probability of the occurrence of a coupling configuration for a given isotope (^{119}Sn) can be obtained from the number of relevant neighbouring tin atoms and from the natural abundance of the various isotopes (see below).

---

[1] To get agreement between estimated and observed intensities they invoked long-range coupling but their argument is difficult to follow.

Table 4-13 Structural data for layered Sn(II) compounds.

Compound	Space group	Ref.	Co-ordination number	Co-ordination type	INTRA-LAYER			INTER-LAYER	
					No. of bonds	No. of neighbours	Distances through space /Å	No. of neighbours	Distances through space / Å
SnO	Tetragonal P4/nmmz	[54]	4	~Tetragonal pyramid	2	8	Groups of 4 at 3.542 & 3.803[b]	4	3.694[a]
SnHPO₃	Monoclinic Ic	[34]	3	~Trigonal pyramid	4	6	Pairs at 4.180, 4.685 & 5.878	2	4.067
SnHPO₄	Monoclinic P2₁/c	[43]	3	~Trigonal pyramid	2	2	3.848	1	4.487
SnC₂O₄	Monoclinic C2/c	[38]	4	Distorted tetrahedral	4	2	5.991	2	4.324
SnSO₄	Orthorhombic Pnma	[42]	3	~Trigonal pyramid	4	6	Two at 5.319 & four at 4.497	2	4.425

[a] Cossement et al. [22] give this as 3.525 Å.
[b] The 3.542 Å pairs have two Sn–O–Sn paths each, whereas the 3.803 Å pairs only have one.

Calculation of satellite intensity

The probability of the occurrence of a coupling configuration for a given isotope (^{119}Sn) can be calculated from the number of neighbouring tin atoms and from the natural abundance of the other isotopes (^{117}Sn). The crystallographic data of SnHPO$_3$ (see Figure 4-1) shows that a given tin has 6 tin atoms four bonds away. Thus, there are 7 possible ways for ^{119}Sn to couple with ^{117}Sn. If the probability of finding n of these neighbours as ^{117}Sn is denoted p_n and the natural abundance of the ^{117}Sn isotope is written as p_{117}, p_n can be calculated from:

$$p_n = \frac{6!}{(6-n)!n!}(p_{117})^n (1 - p_{117})^{6-n} \qquad (4.1)$$

The probability of each pattern are summarised in Table 4-14.

Table 4-14 The relative proportion of each coupling pattern for SnHPO$_3$.

Number of ^{117}Sn	NMR pattern	Combination factor	Fraction of total signal /%
0	A	1	61.91
1	AX	6	30.90
2	AX$_2$	15	6.43
3	AX$_3$	20	0.71
4	AX$_4$	15	0.04
5	AX$_5$	6	negligible
6	AX$_6$	1	negligible

The calculated relative intensity of each of the first satellites (from the AX and AX_3 cases only) is 15.72 % of the total ^{119}Sn intensity. The calculated value for 6 neighbours is in excellent agreement with the experimental results obtained accurately from deconvolution; the results at a spin rate of 11 kHz are 15.92% and 16.37% for the high- and low-frequency satellites respectively, the results at a spin rate of 13 kHz are 16.04% and 16.03% for the high- and low-frequency satellites respectively. These results were measured on sum of sideband and centreband.

The above result strongly suggests that intra-layer interactions are responsible for the satellite peaks and confirms that the coupling is solely heteronuclear in origin. The former statement arises because there are only two close tin neighbours (at 4.067 Å) in the adjacent layer to a given tin atom, which would give rise to very different satellite intensities (predicted value 7.09%). However, it may be noted that the six intra-layer interactions are not all equivalent. The direct interatomic distances occur in three pairs (4.180, 4.685 and 5.878 Å) so the conformational relations differ. Therefore the "through-bond" coupling constants will not be equal, but presumably they are sufficiently close that the satellite peaks cannot be further resolved. It is possible that the six Sn,Sn interactions giving rise to the satellite peaks for the former are 4 intra-layer and 2 inter-layer, of similar magnitude, with much weaker coupling involving the other pair of intra-layer interactions, but this would seem to be relatively unlikely.

The relative intensity of the satellite peaks for $SnHPO_4$ has been also calculated. From the crystallographic data, there are 2 nearest neighbour tin atoms, two-bonded interactions through oxygen atom, and this suggests that there are only 3 possible patterns for ^{119}Sn coupling with ^{117}Sn. The probability of each pattern is shown in Table 4-15. The result for the relative intensity of satellite peaks is 7.09%. This, however, is not consistent with the experiment results with a recycle delay of 1 s (3.14% and 3.37% obtained with spinning at 11 kHz; 3.16% and 3.19% obtained with spinning at 14 kHz). Since the satellite peaks and the main peak may have different relaxation times, use of a short recycle delay can partially saturate the main peak if its relaxation time is longer than those of the satellite peaks. This is very important when doing the DP experiment. Although CP is employed here (where recycle delay depends on proton relaxation time),

it is also worth checking the experiment by using the longer recycle delay of 30 s. A similar result (3.14% and 3.23 %) was obtained with spinning at 14.2 kHz.

Table 4-15 The relative proportion of each coupling pattern for $SnHPO_4$.

Number of ^{117}Sn	NMR pattern	Combination factor	Fraction of total signal / %
0	A	1	85.23
1	AX	2	14.18
2	AX_2	1	0.59

On the other hand, there is only one close Sn,Sn distance (at 4.487 Å) between tins in different layers. This is consistent with the experimental satellite intensities (predicted values 3.71 %), so we suggest that the Sn,Sn coupling gives evidence of effective bonding between tin atoms in different layers as in SnO [22]. It may be noted that in this case the tin atoms in question are related by a centre of symmetry, so that homonuclear coupling would not affect the MAS spectra under any conditions.

The interatomic distance involved in $SnHPO_4$ is substantially greater than that in SnO (which we measure to be 3.694 Å from the report in Ref. [54], though Ref. [22] gives it as 3.525 Å), which presumably accounts for the fact that the coupling constant in the former is significantly less in magnitude (i.e. about half) than the value in the latter. The apparent lack of inter-layer coupling for $SnHPO_3$ in spite of the small Sn,Sn distance (smaller than for $SnHPO_4$) and the analogous lack of intra-layer coupling for $SnHPO_4$ are very surprising.

It is also odd that for tin(II) oxalate and tin(II) sulfate no tin satellites are seen on the tin resonances (in spite of the relatively narrow linewidth for the former) even though the Sn....Sn distances between layers (4.324 Å in the oxalate and 4.425 Å in the sulfate) are comparable to that in the $SnHPO_4$ and the number of bonds separating tin atoms within a given layer is the same as for $SnHPO_3$. Currently we have no rationale for these apparent anomalies.

4.3   Conclusions

High-resolution solid-state ^{31}P and ^{119}Sn spectra of six tin-containing compounds were readily obtained using ramped-CP and DP techniques. High-resolution solid-state NMR gives useful information about crystallographic asymmetric units in cases where the crystal structure is unknown, as for tin(II) diphosphate and CaSnEDTA, studied here. Data on ^{119}Sn shielding anisotropies as measured from spinning sideband analysis manifolds have also been provided for six tin-containing compounds, together with similar information for ^{31}P in three of the cases.

A particularly interesting aspect of the present ^{119}Sn solid-state NMR studies is the observation of large long-range coupling constants between ^{119}Sn and ^{117}Sn nuclei. A very strong four-bond coupling constant between tin nuclei was observed in SnHPO$_3$, 2599 ± 200 Hz in magnitude, and also large coupling between tin nuclei was discovered in SnHPO$_4$, 4151 ± 200 Hz in magnitude, but the latter appears to be inter-layer in origin. Hahn echoes were used to confirm the heteronuclear (^{119}Sn, ^{117}Sn) nature of these coupling constants. Measurement of satellite intensities gave clear evidence of the bonding between tin atoms since the calculated relative intensities of the satellites are also in agreement with the experiment values; although complete understanding of the relationship of coupling to structure has not been obtained.

4.4   References

[1]   J.D. Kennedy, W. Mcfarlane, in *Multinuclear NMR*, J. Mason, Ed., pp 305, Plenum, New York, 1987.
[2]   B. Wrackmeyer, in *Encyclopedia of NMR*, R. K. Harris and D. M. Grant, Eds., Vol. 4, pp 2538, Wiley, London, 1996.
[3]   B. Wrackmeyer, Annu. Rep. NMR Spectrosc. **38** (1999) 203.
[4]   B. Wrackmeyer, Annu. Rep. NMR Spectrosc. **16** (1985) 73.
[5]   R.K. Harris, E.D. Becker, S.M. Cabral De Menezes, R. Goodfellow, P. Granger, Pure Appl. Chem. **73** (2001) 1795.
[6]   S.R. Hartmann, E.L. Hahn, Phys. Rev. **128** (1962) 2042.
[7]   E.O. Stejskal, J. Schaefer, J.S. Waugh, J. Magn. Reson. **28** (1977) 105.
[8]   M. Sardashti, G.E. Maciel, J. Magn. Reson. **72** (1987) 467.
[9]   R.A. Wind, S.F. Dec, H. Lock, G.E. Maciel, J. Magn. Reson. **79** (1988) 136.
[10]   G. Metz, X. Wu, S.O. Smith, J. Magn. Reson. A **110** (1994) 219.

[11] G. Metz, M. Ziliox, S.O. Smith, Solid State Nucl. Magn. Reson. **7** (1996) 155.

[12] J.R. Ascenso, L.H. Merwin, H. Bai, in-house sideband fitting program, University of Durham.

[13] M.M. Maricq, J.S. Waugh, J. Chem. Phys. **73** (1979) 3300.

[14] A.C. Olivieri, J. Magn. Reson. A. **123** (1996) 207.

[15] P. Hodgkinson, L. Emsley, J. Chem. Phys. **107** (1997) 4808.

[16] H. Bai, R.K. Harris, J. Magn. Reson. **96** (1992) 24.

[17] A. Sebald, NMR Basic Principles and Progress **31** (1994) 91.

[18] R.K. Harris, S.E. Lawrence, S.-W. Oh, V.G.K. Das, J. Mol. struct. **347** (1995) 309 and reference therein.

[19] A. Sebald, *in Advanced Applications of NMR to Organomettali Chemistry*, M. Gielen et al., Eds., pp 123, Wiley, London, 1996.

[20] J.C. Cherryman, R.K. Harris, J. Magn. Reson. **128** (1997) 21.

[21] C. Camacho-Camacho, R. Contreras, H. Nöth, M. Bechmann, A. Sebald, W. Milius, B. Wrackmeyer, Magn. Reson. Chem. **40** (2002) 31.

[22] C. Cossement, J. Darville, J.-M. Gilles, J.B. Nagy, C. Fernandez, J.-P. Amoureux, Magn. Reson. Chem. **30** (1992) 263.

[23] D.L. Reger, M.F. Huff, S.J. Knox, R.J. Adams, D.C. Apperley, R.K. Harris, Inorg. Chem. **32** (1993) 4472.

[24] D.C. Apperley, R.K. Harris, D.A. Cleary, Chem. Mater. **5** (1993) 1772.

[25] T. Pietrass, F. Taulelle, Magn. Reson. Chem. **35** (1997) 363.

[26] B.E. Eichler, B.L. Phillips, P.P. Power, M.P. Augustine, Inorg. Chem. **39** (2000) 5450.

[27] L.P. Cruz, J.-M. Savariault, J. Rocha, J.-C. Jumas, J.D. Pedrosa De Jesus, J. Solid State Chem. **156** (2001) 349.

[28] S. Chaudhuri, F. Wang, C.P. Grey, J. Am. Chem. Soc. **124** (2002) 11746.

[29] K.W. Zilm, D.M. Grant, J. Am. Chem. Soc. **103** (1981) 2913.

[30] R.R. Mayhew, L.R. Brown, J. Dent. Res. **60** (1981) 1809.

[31] D.A. Camosci, N. Tinanoff, J. Dent. Res. **63** (1984) 1121.

[32] R. Challoner, T. Nakai, C.A. McDowell, J. Chem. Phys. **94** (1991) 7038.

[33] E. Klaus, A. Sebald, Angew. Chem. Int. Ed. Engl. **34** (1995) 667.

[34] R.C. McDonald, A.R. Erisks, Inorg. Chem. **19** (1980) 1237.

[35] D.E.C. Corbridge, E.J. Lowe, J. Chem. Soc. (1954) 4555.

[36] Varian Incorporated, NMR systems STARS software.

[37] M.A. Petrova, A.E. Mal'shikov, G.A. Mikirticheva, A.S. Novikova, S.A. Petrov, T.G. Kostyreva, Russ. J. Inorg. Chem. **46** (2001) 9.

[38] A. Gleizes, J. Galy, J. Solid State Chem. **30** (1979) 23.

[39] A.A. McConnell, R.H. Nuttall, D.M. Stalker, Talanta. **25** (1978) 425.

[40] S. Aime, R. Gobetto, R. Nano, E. Santucci, Inorg. Chim. Acta. **123** (1987) L23.

[41] T.M. Alam, R.A. Assink, Magn. Reson. Chem. **35** (1997) 427.

[42] J.D. Donaldson, D.C. Puxley, Acta Cryst. **B28** (1972) 864.

[43] H.Y. Carr, E.M. Purcell, Phys. Rev. **94** (1954) 630.

[44] S. Meiboom, D. Gill, Rev. Sci. Instr. **29** (1958) 688.

[45] W. Adcock, A.R. Krstic, Magn. Reson. Chem. **35** (1997) 663.

[46] F. Banse, F. Ribot, P. Tolédano, J. Maquet, C. Sanchez, Inorg. Chem. **34** (1995) 6371.

[47]   T.P. Lockhart, W.F. Manders, F.E. Brinckman, J. Organomet. Chem. **286** (1985) 153.

[48]   N.J. Clayden, C.M. Dobson, A. Fern, J. Chem. Soc. Dalton Trans. (1989) 843.

[49]   H. Bai, Ph.D. Thesis, University of Durham (1991).

[50]   R.K. Harris, A. Sebald, Magn. Reson. Chem. **27** (1989) 81.

[51]   C. Marichal, A. Sebald, Chem. Phys. Lett. **286** (1998) 298.

[52]   N.J. Clayden, C.M. Dobson, L.-Y. Lian, J. Magn. Reson. **69** (1986) 476.

[53]   C.P. Grey, D. Phil Thesis, University of Oxford (1990).

[54]   J. Pannetier, G. Denes, Acta Cryst. **B36** (1980) 2763.

CHAPTER 5

STUDIES OF TWO-SPIN ^{31}P, ^{1}H SYSTEMS

5.1   Introduction

This chapter will focus on the study of two systems containing relatively isolated ^{1}H, ^{31}P spin pairs, using high-resolution solid-state NMR techniques.   Both protons and phosphorus nuclei are abundant spins (spin-½ isotopes).   In this work, tin (II) phosphite (SnHPO$_3$) and tin (II) hydrogen phosphate (SnHPO$_4$) were investigated   (though most attention is given to SnHPO$_3$) to show both the opportunities and the complications in these isolated spin systems.

Unlike NMR in the solution state, where rapid isotropic re-orientation efficiently averages out anisotropic interactions, NMR of the solid-state is dominated by anisotropic interactions, most notably dipolar coupling between nuclear spins.   For typical solid organic materials, for example, ^{1}H NMR spectra are broad and featureless as a result of the strong and numerous dipolar interactions between the protons.   Spinning the sample rapidly at the "magic angle"–Magic-Angle Spinning (MAS)–can significantly improve resolution by partly suppressing the dipolar interactions, but the resolution remains low compared to that for solution-state NMR.   On the other hand, spinning at moderate rates also gives rise to high-resolution spectra, but with the addition of spinning sidebands, the intensities of which provide a wealth of anisotropy information by suitable analysis. Interesting cases occur when several interactions, each of which is a tensor, contribute to the intensity distribution, as when shielding (σ), (direct) dipolar coupling (D), and (indirect) scalar coupling (J) are all important.   The interplay of tensors results in different effective anisotropies as displayed in the intensity distribution of the spinning-sideband manifolds [1,2].   This influence was also observed in coupled proton and phosphorus spectra for SnHPO$_3$.

The cross-polarisation (CP) experiment with MAS not only enhances the signal intensity of rare spins (S) with low gyromagnetic ratios by transferring magnetisation from the abundant spins (I), but also provides valuable information on the dipolar coupling between I and S spins for strongly coupled spin systems when the "transient oscillations" are observed during short contact times, T_{CP} [3]. This phenomenon generally occurs under very fast spin rates resulting in the fact that the efficient transfer of magnetisation is perturbed [4,5] and the "matching condition" becomes $v_I = v_S + nv_r$, where v_r is the spin rate. In the limit of spinning fast compared to the dipolar linewidth, n is restricted to $\pm 1, \pm 2$. Note that at modest spin rates efficient transfer of magnetisation can occur between abundant (I) and rare (S) spins by matching the nutation rates associated with the RF fields applied simultaneously to the two nuclei, $v_I = v_S$ [6,7].

In this study of ^{31}P CPMAS of SnHPO$_3$ and SnHPO$_4$, the ^{1}H, ^{31}P dipolar couplings were able to be determined by measuring the transient oscillations on cross-polarisation build-up curves [8], and hence the length of the ^{1}H, ^{31}P internuclear distance in these systems. This distance could not be determined by X-ray diffraction studies due to the difficulty of locating the H atoms in the presence of the strong scattering from Sn [9].

It has been well known that heteronuclear decoupling is one of the main components of high-resolution solid-state NMR. A spectrum, e.g. ^{13}C spectrum, can often be significantly improved when the heteronuclear interaction is suppressed. Continuous-wave (CW) RF irradiation [7,10] is the main technique to achieve the high resolution and sensitivity, in which a RF field is applied at the Larmor frequency of proton to reduce their influence on carbon, whose signal is observed. It is generally accepted that for efficient decoupling the RF field strength must be greater than the magnitudes of both the homonuclear and the heteronuclear interactions. Nevertheless, using ^{31}P CW decoupling for the isolated ^{1}H, ^{31}P pair does not lead to a sharp line but rather the {^{31}P}-^{1}H spectra exhibit complicating features. The second-order recoupling of shielding and dipolar coupling tensors has been previously described in carefully-chosen model systems [11], but has not, to be the best of our knowledge, been previously reported on "normal" samples. These effects lead to unexpected line-splittings, which could have been

mistaken for real features in more complex systems. This chapter will show how these effects can be diagnosed from their dependence on decoupling, although it proves difficult to eliminate them completely due the size of the ^{31}P chemical shift anisotropy (CSA) relative to the strength of the RF decoupling.

Very recently, it has been reported that the line splitting which comes from second-order effects can be strongly reduced using two-pulse phase modulation (TPPM) decoupling [11-13] in contrast to CW decoupling. This sequence offers a simple way to decouple better than with CW irradiation. TPPM involves continuous irradiation with repetition of two pulses of equal flip angle α_p, usually close to π, and with a phase difference of $\Delta\phi$. In this study, this decoupling sequence was also implemented for our case, $\{^{31}P\}\text{-}^1H$.

5.2   Results and Discussions

5.2.1   Interplay of shielding, direct and indirect coupling tensors

A single pulse-and-acquire method was employed to obtain ^{1}H spectra and direct-polarisation without proton decoupling was used to observe ^{31}P spectra for SnHPO$_3$. The coupled proton and phosphorus spectra are illustrated in Figure 5-1 (a) and (b) respectively. Apparently, each spectrum consists of two peaks for the centrebands. The splittings observed in the coupled spectra (both ^{1}H and ^{31}P) suggest that this is due to scalar coupling. The investigation of the isotropic scalar coupling will be given later in section 5.2.2. It should be noted that all proton spectra presented in this Chapter were obtained after implementing the "backward linear projection" of data shift. This process is essential due to the probe background problem.

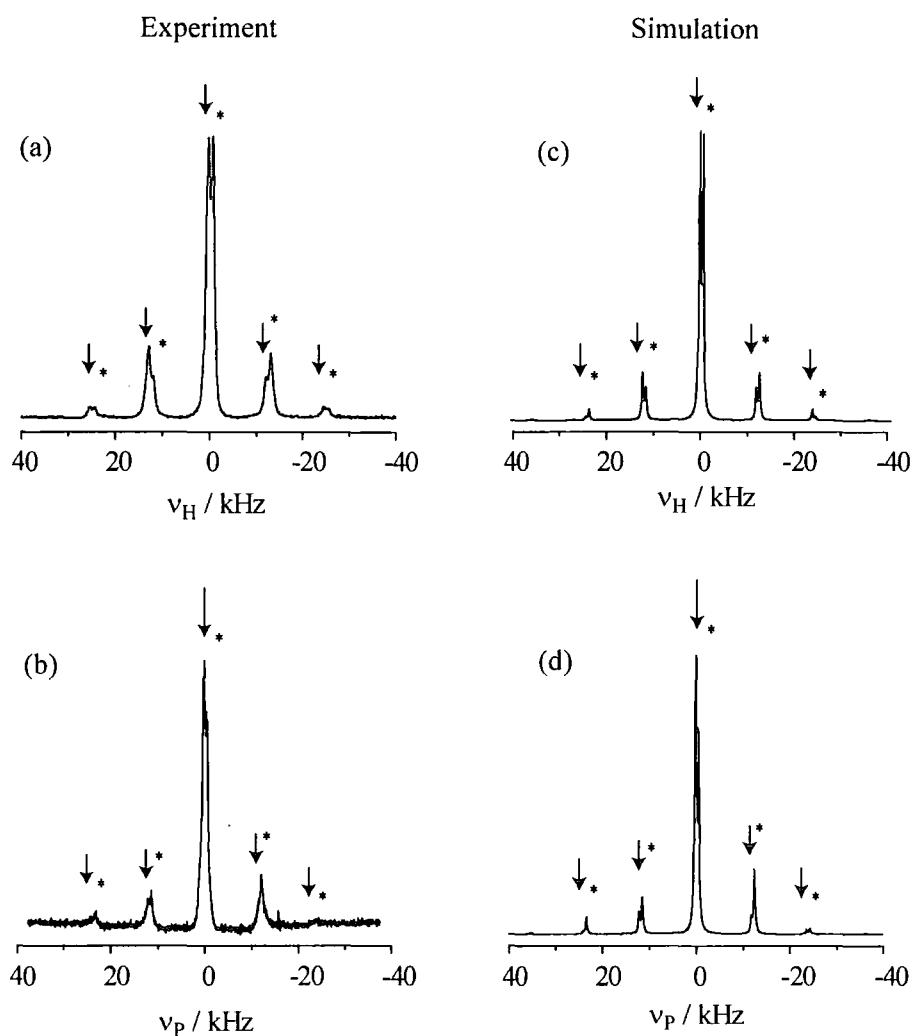Experiment   Simulation

Figure 5-1 Experimental (a) Proton spectrum and (b) phosphorus-31 spectrum of tin(II) phosphite at 200.13 MHz spectrometer, obtained at a spin rate of (a) 12.5 kHz with a single-pulse experiment, (b) 11.6 kHz with direct-polarisation under without proton CW decoupling. Simulated (a) ^{1}H and (b) ^{31}P coupled MAS spectra at 200.13 and 81.01 MHz respectively. ↓ and * indicate the two sets of sidebands, which relate to the high- and low-frequency centrebands respectively. The centrebands of these two manifolds are separated by J_{PH}. Acquisition parameters were: (a) recycle delay 120 s and number of transients 4; (b) recycle delay 300 s and number of transients 4. Simulation parameters: ^{31}P,^{1}H dipolar interaction 16.8 kHz; ^{31}P shielding anisotropy –68 ppm, ^{31}P shielding asymmetry 0 (the results for shielding anisotropy and asymmetry were analysed using SSB97 [14] and are shown in Table 4-1); J_{PH} 693 Hz (obtained from the result in section 5.2.2); spin rate 12.5 kHz.

As shown above in Figure 5-1 (a), the structures of the sidebands on both sides of the centreband show inverted intensity, but the total intensities of the two sideband manifolds are approximately equal as established by careful deconvolution. For the ^{31}P spectrum (Figure 5-1 (b)), the sideband structures are more complicated, and also the observed two peaks are clearly of unequal intensity, but again the total intensities of the two sideband manifolds are equal. These appearances can be explained from the influence of the interplay of shielding (σ), (direct) dipolar coupling (D), and (indirect) scalar coupling (J) tensors. The theory of such interplay for isolated heteronuclear two-spin (IS) systems with $I_I = I_S = 1/2$ has been stated by Harris *et al.* [1]. The simplest case occurs when axial symmetry prevails, and thus all three tensors (for the A spin) are co-axial (with the major principal axes of σ and J along the internuclear I, S distance, r_{IS}). Note that the theory of this influence is given in Chapter 2.

Clearly, the influence of the interplay of tensors has an effect on the spinning sideband manifolds for both ^{1}H or ^{31}P spectra, but in different ways: the full proton spectrum is nearly symmetrical, in contrast to the phosphorus spectrum. This is related to the magnitude of the shielding anisotropy; proton shielding anisotropy is likely to be small whereas phosphorus shielding anisotropy is relatively large.

In addition, it is easy to observe the distribution into the two sub-spectra for bandshapes of static powder patterns for this isolated ^{1}H, ^{31}P pair, as shown in Figure 5-2. Cross-polarisation and direct-polarisation spectra without proton decoupling were obtained from the Chemagnetics CMX200 and Varian InfinityPlus spectrometers. One static powder spectrum is clearly 'stretched' whereas in the other is 'squeezed' under the influence of effective anisotropies, ζ_A^{eff}. Since the separation between the horns (dipolar coupling) is unaffected by the interplay of tensors, the differences between the horns from the two fields are found to be closely similar, *ca.* 16.4 kHz and *ca.* 16.6 kHz at 4.7 T and 11.7 T respectively.
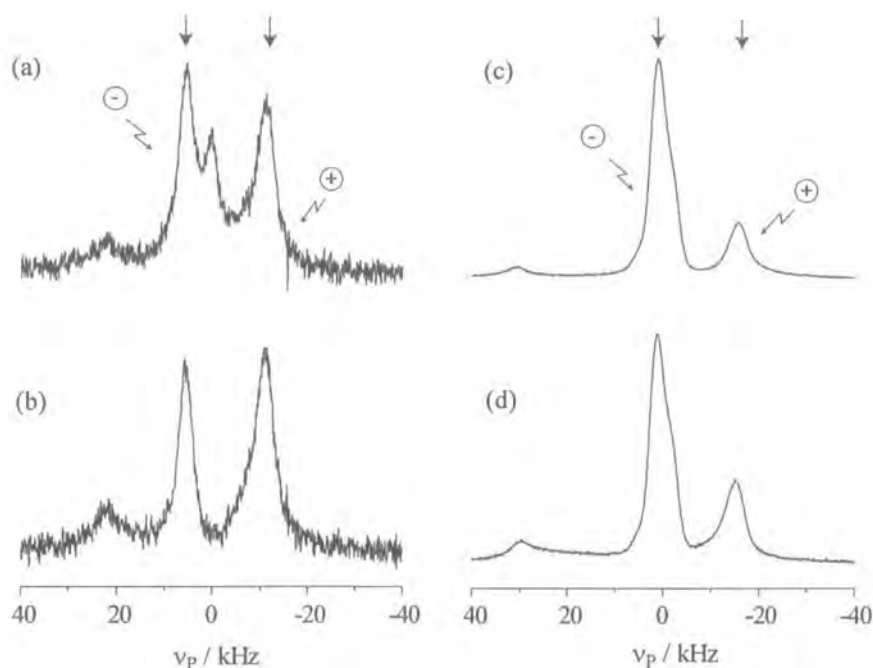
Figure 5-2 Phosphorus-31 static spectra of tin(II) phosphite at (a), (b) 81.01 MHz, and (c), (d) 202.28 MHz. Direct-polarisation without high-power proton decoupling was employed in (a) and (c), recycle delay 300 s and number of transient (a) 100 and (b) 21. Cross-polarisation from protons without high-power proton decoupling was used in (b) and (d). Acquisition parameters were: recycle delay 120 s; contact time 5 ms; number of transients (b) 80 and (d) 8. The separation between the horns is indicated by the arrows. The "stretched" subspectrum and the "squeezed" subspectrum are marked with the "plus" and "minus" respectively.

At a field of 4.7 T, the measured magnitudes of the 'stretched' and 'squeezed' effective anisotropies are 32 and 16 kHz, respectively (see Figure 5-2 (a) and (b)). Use of Equation 2.11 from Chapter 2, shows that when the ^{31}P shielding anisotropy is –68 ppm and the dipolar interaction is 16.8 kHz (an effective dipolar interaction $D' = D - \Delta J / 3 \approx D$ when $\Delta J \approx 0$), the calculated magnitudes of the 'stretched' and 'squeezed' anisotropies ($\Delta \sigma$) are 33 and 16.5 kHz, respectively. These values are in excellent agreement with the experiments. This is not true only at the low field but also at the high field. Table 5-1 summarises the data for the magnitude of the stretched and squeezed anisotropies between the calculations and experiments. The appearances of the stretched and squeezed

subspectra are more pronounced at the higher field due to the increase in size of the ^{31}P shielding anisotropy expressed in Hz. (The anisotropy in J is assumed to be zero for the calculation.) Note that the dipolar interaction used for the simulation in this Chapter is 16.8 kHz, obtained from a variable contact time experiment at a spin rate of 15 kHz as described in Section 5.2.3.

Table 5-1 Experimental and calculated values of the stretched and squeezed sub-spectra ($\Delta\sigma^{eff}$). The shielding anisotropy of ^{31}P is -68 ppm. D_{PH} is 16.8 kHz obtained from a variable contact time experiment described in Section 5.2.3.

Magnetic	Experiment /kHz^{a}			Calculation /kHz		
field / T	stretched	Squeezed	horn separation	stretched	squeezed	horn separation
4.7	32	16	16.4	33	17	16.8
11.7	45	6	16.6	46	5	16.8

^{a} ± 200 Hz.

Note that the anomalous lineshapes for the static coupled spectra are observed at 81.01 MHz, which Figure 5-2 (a) shows an extra peak at the middle and in Figure 5-2 (b) displays 'dip' between two horns. These unexpected appearances may relate to the unusual CSA patterns observed under condition of proton decoupling (see Chapter 7). However, the bandshape distortion does not affect the magnitude of the 'squeezed' and 'stretched' anisotropies.

The signs of the ^{31}P shielding anisotropy and the scalar coupling constant (J_{PH}) can be taken into account in the features of the two sub-spectra. Note that D is positive since γ_H and γ_P are both positive. Since the ^{31}P shielding anisotropy is negative in sign, as derived using SSB97 [14], and $^{1}J_{PH}$ has been also known to be positive [15], it is evident that the structure of the two sub-spectra (Figure 5-2) is in agreement with one of the four possible types of static two-spin spectra [1].

When such distributions of the two sub-spectra both in static and spinning spectra arise from the interplay of tensors, it is also of interest to simulate the appearance of phosphorus-31 proton-coupled spectra. Such simulated static ^{31}P spectra are shown in

Figure 5-3 using SIMPSON [16] and compared to the experimental spectra in Figure 5-2. For spinning cases, Figure 5-1 (c) and (d) shows simulated ^{1}H and ^{31}P coupled MAS spectra, which are consistent with the experimental results (Figure 5-1 (a) and (b)). Clearly, the influence of the interplay of tensors dominates the appearance of the coupled spectra for the isolated heteronuclear two-spin (^{31}P, ^{1}H) systems.
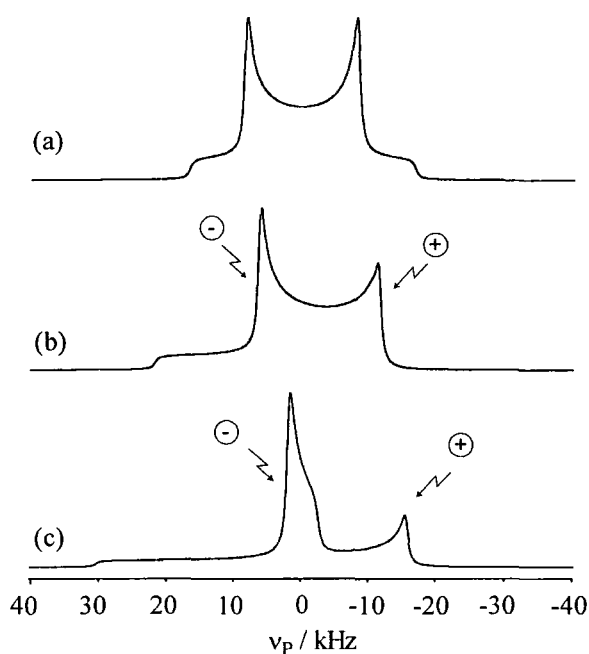

Figure 5-3 Simulated ^{31}P static proton-coupled spectra at (a), (b) 81.01 MHz and (c) 202.28 MHz. For the purpose of comparison, (a) no interplay of tensors has been taken onto account in the simulation. Other simulation parameters: ^{31}P, ^{1}H dipolar interaction 16.8 kHz; ^{31}P shielding anisotropy -68 ppm, ^{31}P shielding asymmetry 0. The "stretched" subspectrum and the "squeezed" subspectrum are marked with the "plus" and "minus" respectively.

The proton spinning sideband manifolds were also analysed (using SSB97) to extract the effective values for the anisotropy and asymmetry shown in Table 5-2. These results will not be accurate because there are very few spinning sidebands. However, the results for the anisotropies of the two sub-spectra are similar in magnitude as expected because the dipolar coupling constant is likely to be much larger than the proton shielding anisotropy. It is not feasible to derive a value for the latter. The subspectra anisotropies are equivalent to a dipolar coupling constant of 21 kHz (see Chapter 2). This is in approximate

agreement with the dipolar interaction of 16.8 kHz obtained from the Fourier transformation of data from a variable contact time experiment, discussed in section 5.2.3.

Table 5-2 Tensor data for protons in SnHPO$_3$.

δ_{iso}/ ppm	Anisotropy ζ^{eff} / ppm	Asymmetry η_{eff}
7.8	106 ± 4	0.00 ± 0.24
2.8	-104 ± 4	0.00 ± 0.23

It is not possible to obtain the effective shielding anisotropy of ^{31}P accurately from the coupled phosphorus spectrum because there are very few spinning sidebands, as shown previously in Figure 5-1 (b).

5.2.2   The proton-phosphorus scalar coupling constant

As previously shown, the coupled spectra of ^{1}H and ^{31}P for SnHPO$_3$ (Figure 5-1) contain splittings arising from the indirect coupling constant, J_{PH}. The magnitude of the splittings obtained by careful deconvolution was *ca.* 960 Hz from the proton spectrum obtained at a spin rate of 12.5 kHz and *ca.* 690 Hz for phosphorus spectrum at a spin rate of 11.6 kHz. In principle, they should be the same, but from the experiments there is a discrepancy.

It is important to note that a significant property of scalar coupling is that the coupling constant remains unchanged (when expressed in Hz) at different fields. Hence, it can easily be measured by running the sample at three different fields, 4.7 T, 7.05 T and 11.7 T. Figure 5-4 shows the ^{1}H and ^{31}P spectra obtained on a Varian UnityPlus 300 spectrometer. The line splittings are found, and the values are *ca.* 970 Hz and *ca.* 690 Hz from single-resonance ^{1}H and ^{31}P spectra (obtained at a spin rate of 16 kHz), respectively. Figure 5-5 illustrates the ^{1}H and ^{31}P spectra obtained at a spin rate of 15 kHz on a Varian InfinityPlus 500 spectrometer. The line splittings are extracted, and the values are *ca.*

930 Hz and *ca.* 700 Hz from single-resonance ^{1}H and ^{31}P spectra, respectively. The magnitudes from the experiments at the three fields are similar. However, the apparent inconsistency of J_{PH} values from ^{1}H and ^{31}P remains.
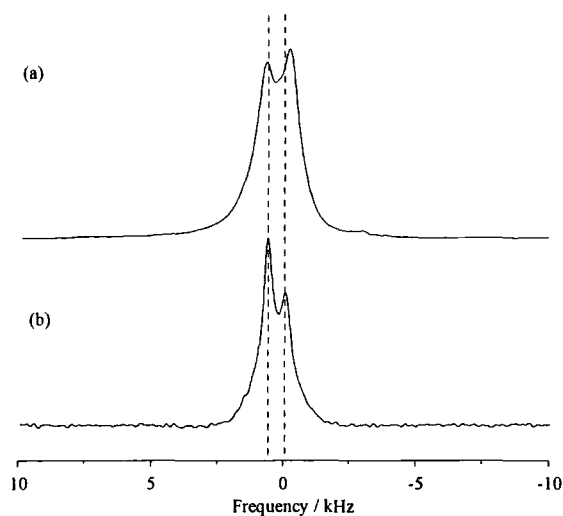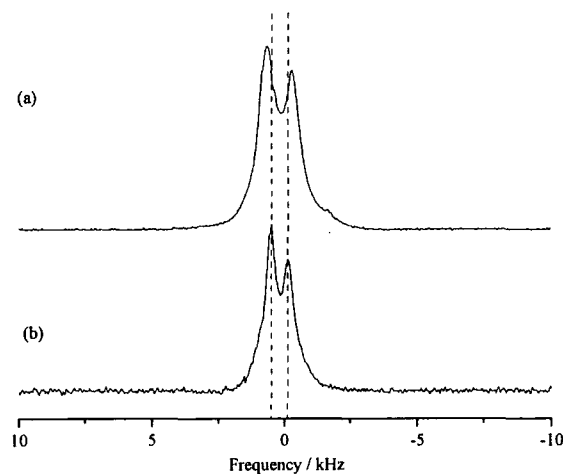

Figure 5-4 (a) ^{1}H and (b) ^{31}P spectra of tin(II) phosphite at 7.05 T obtained at a spin rate of 16 kHz. Spectrometer operating conditions: (a) recycle delay 300 s and number of transients 4; (b) recycle delay 600 s and number of transients 4.

Figure 5-5 (a) ^{1}H and (b) ^{31}P spectra of tin(II) phosphite at 11.7 T obtained at a spin rate of 15 kHz. Spectrometer operating conditions: (a) recycle delay 120 s and number of transients 4; (b) recycle delay 300 s and number of transients 4.

Therefore, it is of interest to obtain an accurate value for the coupling constant. A spin-echo experiment [17] was used to provide more precise information on coupling constants. A single Hahn echo-experiment of ^{31}P, with 180° pulses implemented simultaneously [17,18] for both proton and phosphorus nuclei after cross-polarisation, successfully resolved the heteronuclear coupling between phosphorus and proton. The pulse sequence is displayed in Figure 5-6. Use of such a spin-echo pulse sequence removes many line-broadening mechanisms, yielding the intrinsic linewidth and thus disclosing a contribution from heteronuclear spin-spin coupling (see Chapter 2).
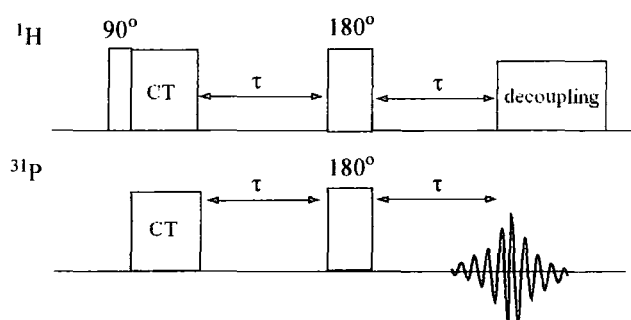

Figure 5-6 Pulse sequence of the single Hahn echo experiment, used for ^{31}P by applying π pulses to both nuclei after cross-polarisation. The refocusing time, τ, is rotor-synchronised.
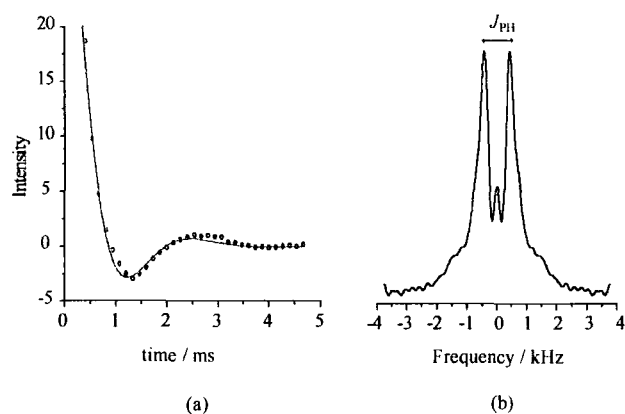

Figure 5-7 Result of a single Hahn-echo experiment obtained by applying π pulses simultaneously to both proton and phosphorus nuclei for SnHPO$_3$: (a) Time evolution at a spin rate of 15 kHz with proton decoupling power equivalent to 83 kHz; (b) Fourier transform of (a) after zero filling but with no line broadening.

As expected, the signal decay in the time domain was modulated by heteronuclear coupling, as shown in Figure 5-7. An oscillation was indeed observed and revealed a symmetrical doublet after Fourier transformation. The decay rate could be fitted easily with the equation

$$y = A + B\cos(\pi J 2\tau)\exp(-2\tau / T_2) \tag{5.1}$$

This reveals the scalar coupling as J_{PH}, is 693 ± 12 Hz, which corresponds approximately to the values reported, 580-800 Hz, in solution-state NMR for $Na_2H_2P_2O_5$, the divalent anion PHO_3^{2-} in isotonic solution, and Na_2PHO_3 [19-21]. Such one-bond P-H coupling constants appear always to be positive [15]. The result is close to that obtained directly from the ^{31}P spectra (see above) so it is concluded that the ^{1}H splitting is anomalous (see below).

Another parameter that we took into account to explain the unexpected inconsistency of the splitting observed from ^{31}P and ^{1}H spectra is the spin rate. The situation concerning the coupled spectra is more complicated when we consider the magnitude of the splittings at different spin rates. Figure 5-8 shows that the splittings of the ^{1}H spectra decrease with increasing spin rate while the splittings of the ^{31}P spectra are more constant at spin rates higher than 12 kHz. The results observed from three different fields are similar. These experiments are useful and may imply that an asymptotic value of the splitting from the ^{1}H spectrum is possible to be obtained at very fast spin rates ($v_r >> 16.8$ kHz). However, at the highest spin rate (22 kHz) available from the 3.2 mm probe, it is not sufficient to reduce the splitting to the isotropic coupling constant.
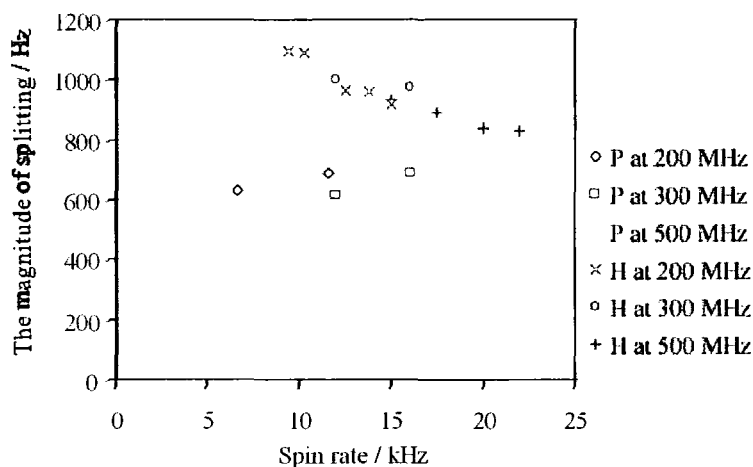
Figure 5-8 Plots of the magnitude of the splitting, obtained from deconvolution of ^{31}P and ^{1}H spectra, as a function of spin rate at different three different fields, 4.5, 7.05 and 11.7 T.

Figure 5-9 also shows the ^{1}H spectra at different spin rates. Apparently, a sideband pattern can be observed at low spin rates. The heteronuclear dipolar coupling becomes time-dependent under MAS and leads to sideband patterns as does the chemical shift anisotropy (CSA). The behaviour of forming spinning sidebands at a low spin rate is indicative of an inhomogeneous system, obtained because the P,H spin pair is relatively isolated. This, however, is not the case for tightly coupled spin systems such that the proton spectrum is not easy to break down at such a spin rate of 6 kHz.
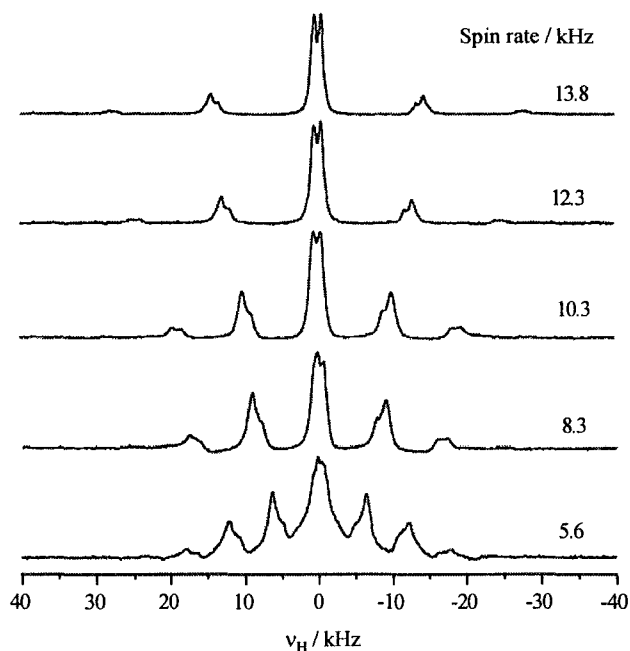
Figure 5-9 ^{1}H spectra at 200.13 MHz as a function of spin rate. A single-pulse experiment was employed with recycle delay 120 s and number of transients 4.

5.2.3   P-H distance determination in SnHPO$_3$ and SnHPO$_4$

The experiments in this section were carried out at 11.7 T on the Varian InfinityPlus spectrometer equipped with a 3.2 mm double-resonance MAS probe. To stabilise the spin rate, the MAS controller was used.

Standard Hartmann-Hahn cross-polarisation was used to transfer magnetisation from ^{1}H to ^{31}P, where the signal was detected. The integrated intensity of the ^{31}P resonance in SnHPO$_3$ as a function of the proton RF-field strength for spin rates of 15 and 18 kHz is shown for a fixed contact time of 5 ms, respectively, in Figure 5-10 (^{31}P spin-lock field of 83 kHz). The behaviour for ^{31}P in SnHPO$_4$ is similar, as shown in Figure 5-11 for spin rates of 12 and 15 kHz with a fixed contact time of 10 ms and the ^{31}P spin-lock field strength was 71 kHz. As expected, the ±1 and ±2 sidebands clearly dominate the matching profiles, i.e. efficient CP under fast spinning can only be obtained by matching

at the ± 1 and ± 2 sidebands, $v_I = v_S + nv_r$. The $n = \pm 1$ matching condition is preferred in practice because the effective dipolar coupling is larger than at $n = \pm 2$ [8].

It should be noted that the difference in estimated nutation rates for the sidebands in Figure 5-10 and 5-11 do exactly match the actual spin rate, within the error limits on the nutation rates. The matching profile needs to be obtained first to identify the ^{1}H RF field strength at $n = \pm 1$, and a variable contact time experiment to extract the dipolar coupling can be carried out later.

The build-up of the ^{31}P magnetisation as a function of CP contact time at different Hartmann-Hahn matching conditions was determined for SnHPO$_3$ and SnHPO$_4$. The results for SnHPO$_3$ at the $n = \pm 1$ matching condition at a spin rate of 15 kHz are shown in Figure 5-12. For this experiment, seventy-eight increments of the contact time were used in the range of 0–1.15 ms. A narrow range of contact times was studied since the splitting between the horns of the powder pattern is largely independent of the long-time behaviour of the build-up curve, which is affected by factors such as spin-diffusion and $T_{1\rho}$ relaxation [22]. As illustrated in Figure 5-12, no significant intensity decay due to $T_{1\rho}$ relaxation is detected for the range of contact times used. Clear "transient oscillations" are seen at short contact times indicating the presence of a strong resolved ^{31}P, ^{1}H dipolar coupling. The same experiment performed at 18 kHz also shows pronounced dipolar oscillations, as displayed in Figure 5-13.
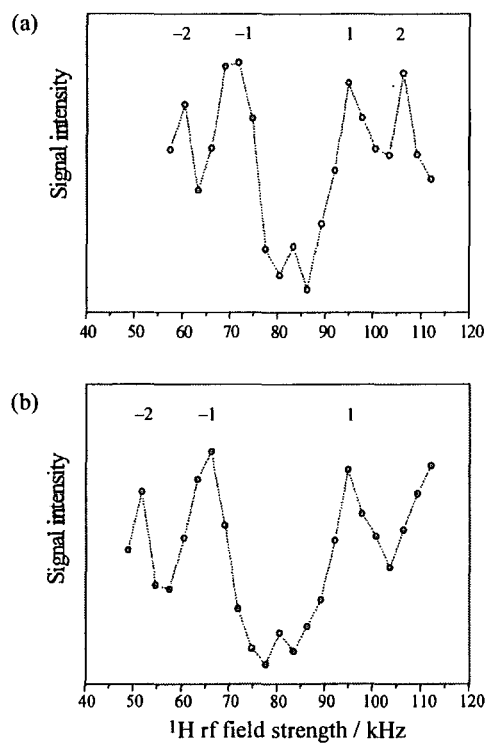
Figure 5-10 Intensity of the ^{31}P signal for SnHPO$_3$ following cross-polarisation from protons as a function of the ^{1}H RF field strength at a spin rate of (a) 15 kHz and (b) 18 kHz. The matching 'sidebands', corresponding to efficient cross-polarisation, are located at the Hartmann-Hahn condition plus and minus multiples of the MAS frequency. Acquisition parameters: ^{31}P RF field strength 83 kHz; contact time 5 ms; recycle delay 120 s; number of transients 4. The proton decoupling power during acquisition time was equivalent to 70 kHz. The ^{31}P and ^{1}H transmitter frequencies were exactly on resonance.
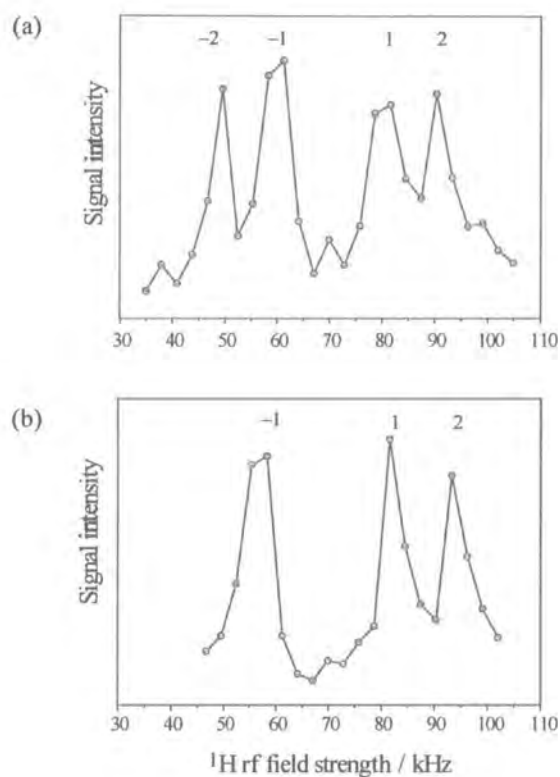
Figure 5-11 Intensity of the ^{31}P signal for SnHPO$_4$ following cross-polarisation from protons as a function of the ^{1}H RF field strength at a spin rate of (a) 12 kHz and (b) 15 kHz. The matching 'sidebands', corresponding to efficient cross-polarisation, are located at the Hartmann-Hahn condition plus and minus multiples of the MAS frequency. Acquisition parameters: ^{31}P RF field strength 71 kHz; contact time 10 ms; recycle delay 120 s; number of transients 4. The proton decoupling power during acquisition time was equivalent to 70 kHz. The ^{31}P and ^{1}H transmitter frequencies were exactly on resonance.

Fast CP MAS at 12 and 15 kHz was also applied successfully for SnHPO$_4$. The variable contact time curves at the $n = \pm 1$ matching condition are presented in Figure 5-14, with forty increments of contact time in the range of 0–1.6 ms. The oscillatory behaviour is less pronounced than is observed in SnHPO$_3$. This behaviour corresponds to the lower magnitude of the dipolar coupling since stronger dipolar coupling gives more pronounced oscillations.
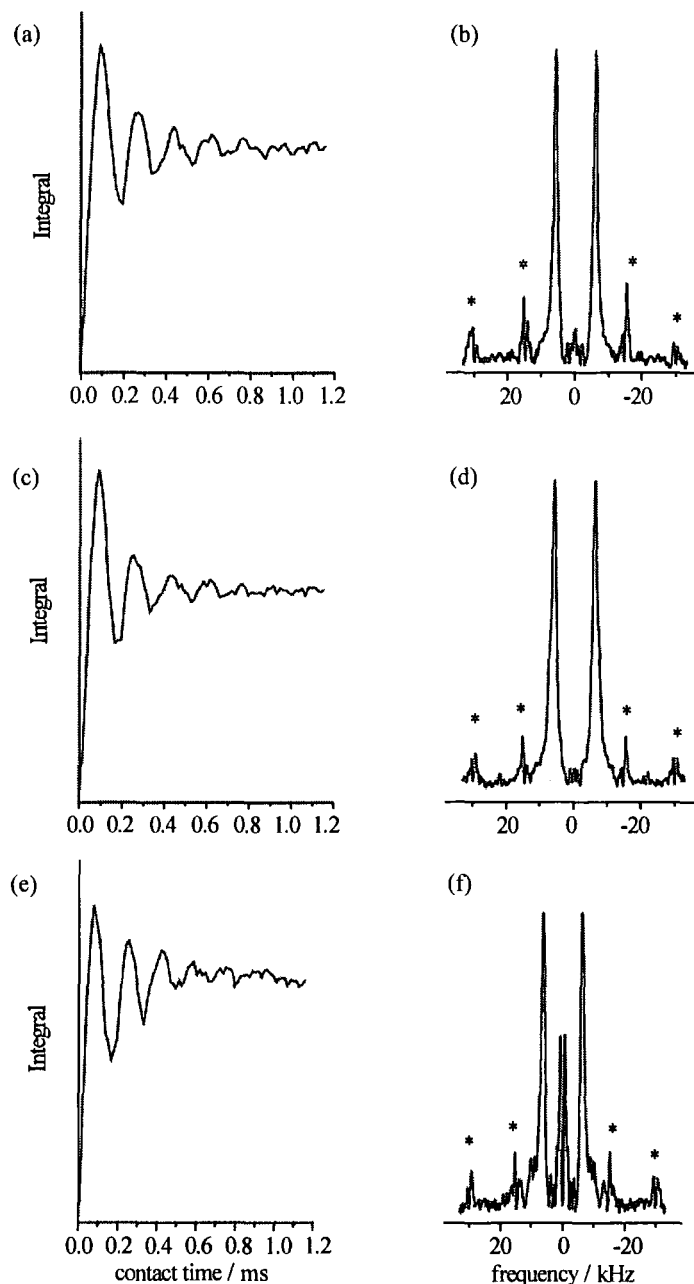
Figure 5-12 $\{^1H\}$-^{31}P cross-polarization dynamics for SnHPO$_3$. For curve (a) and (c), the spin rate was set to 15 kHz for the matching conditions of $n = +1$ and $n = -1$ respectively. (b) and (d) Fourier transform of (a) and (c) after multiplication by -1, removal of "DC offset" and zero-filling. For (a), $v_1(^1H) \approx 95$ kHz and $v_1(^{31}P) \approx 83$ kHz, whereas $v_1(^1H) \approx 72$ kHz and $v_1(^{31}P) \approx 83$ kHz were set for (c). The mis-setting for (e) was set to $v_1(^1H) \approx 92$ kHz and $v_1(^{31}P) \approx 83$ kHz. (f) Fourier transform of (e) with the same data treatment as in (b). The acquisition parameters were: recycle delay 120 s; number of transients 4. Asterisks mark frequency components at multiples of the spinning speed arising from a "periodic quasi-equilibrium" state [22].
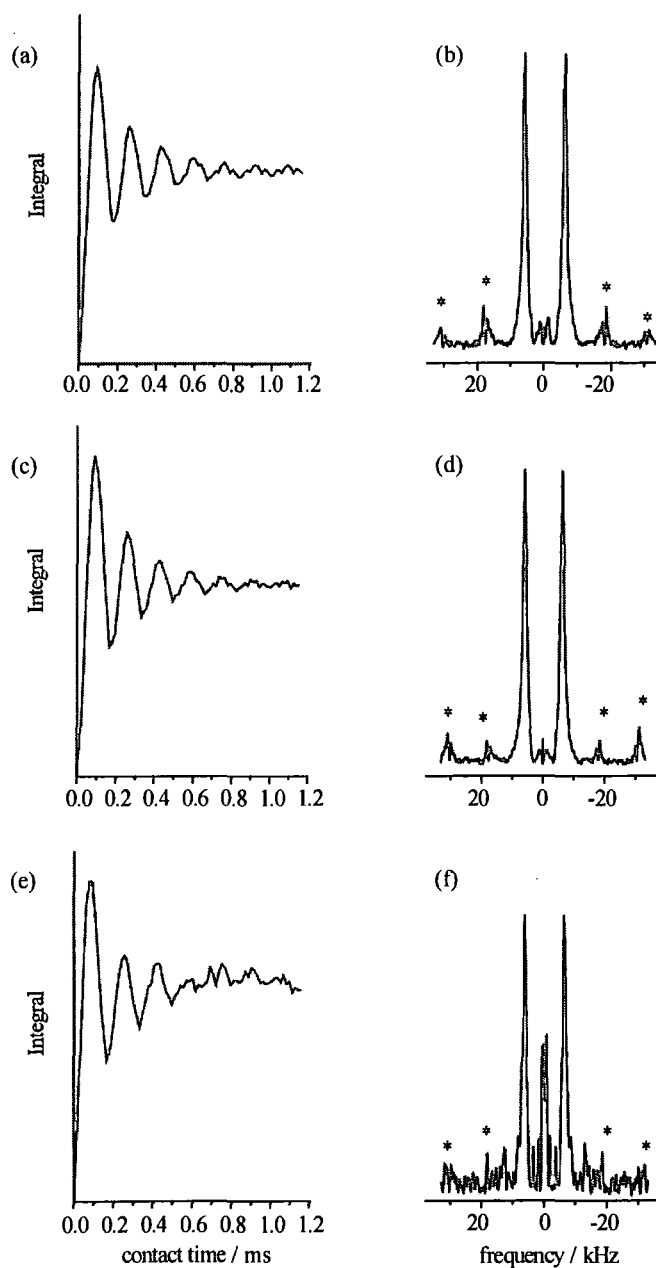
Figure 5-13 $\{^{1}\text{H}\}$-^{31}P cross-polarization dynamics for SnHPO$_3$ under a spin rate of 18 kHz at the $n = \pm 1$ Hartmann-Hahn matching condition. For curves (a) and (c), the matching condition was set to $n = +1$ and $n = -1$ respectively. (b) and (d) Fourier transform of (a) and (b) after multiplication by -1, removal of "DC offset" and zero-filling. For (a), $v_1(^{1}\text{H}) \approx 95$ kHz and $v_1(^{31}\text{P}) \approx 83$ kHz, whereas $v_1(^{1}\text{H}) \approx 66$ kHz and $v_1(^{31}\text{P}) \approx 83$ kHz were set for (c). The mis-setting for (e) was $v_1(^{1}\text{H}) \approx 92$ kHz and $v_1(^{31}\text{P}) \approx 83$ kHz. (f) Fourier transform of (e) with the same data treatment as in (b). The acquisition parameters were: recycle delay 120 s; number of transients 4.
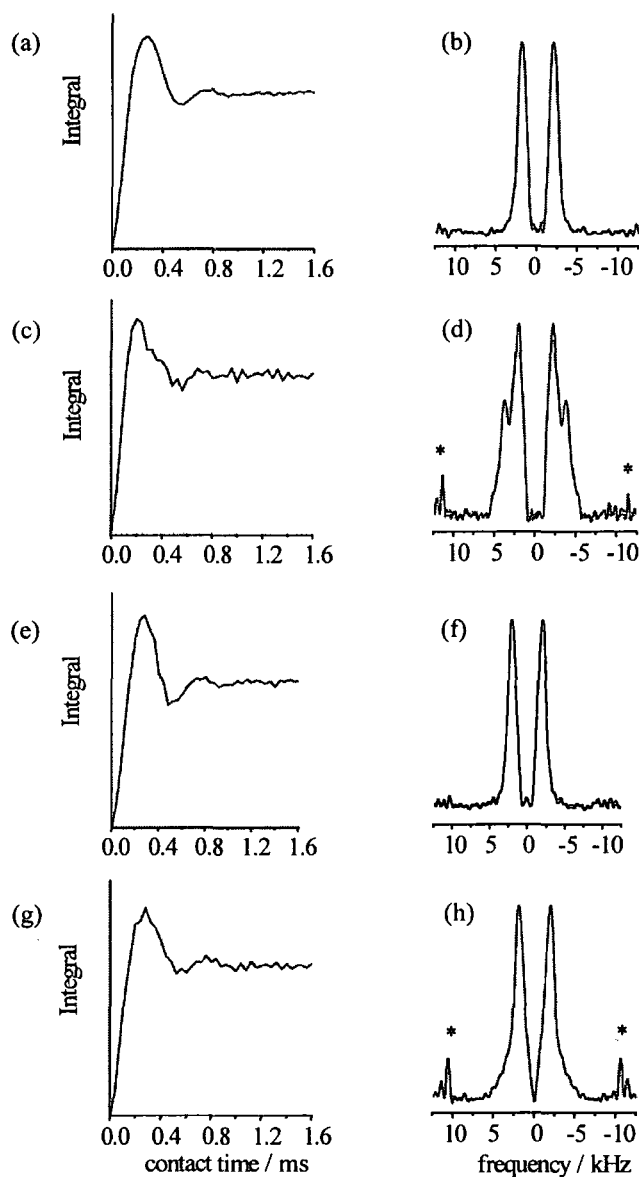
Figure 5-14 {^{1}H}-^{31}P cross-polarization dynamics for SnHPO$_4$ at a spin rate of 12 kHz for (a) and (c), and 15 kHz for (e) and (g). Hartmann-Hahn matching conditions were: (a) v_1(^{1}H) and v_1(^{31}P) estimated to be 82 and 71 kHz respectively; (c) v_1(^{1}H) and v_1(^{31}P) estimated to be 61 and 71 kHz respectively; (e) v_1(^{1}H) and v_1(^{31}P) estimated to be 82 and 71 kHz respectively; (g) v_1(^{1}H) and v_1(^{31}P) estimated to be 58 and 71 kHz respectively. (b), (d), (f) and (h) Fourier transforms of (a), (c), (e) and (h) after multiplication by -1, removal of "DC offset" and zero-filling. The acquisition parameters were: recycle delay 60 s; number of transients 4.

Fourier transformation of the build-up curves gives Pake-like powder patterns in the frequency domain, as presented above. The difference between the horns of the powder pattern is directly proportional to the dipolar coupling, D_{PH}, which depends on the order, n, of the sideband matching condition (see below). This situation has been addressed by Bertani *et al.* [8]. Following Ref. [8], it is known that, under fast spinning conditions $(v_r >> D_{PH})$ at the $n = \pm 1$ and $n = \pm 2$ sideband matches, the transferred magnetisation is given by (neglecting spin-lattice relaxation in the rotating frame and ^{1}H-^{1}H/^{31}P-^{31}P spin diffusion [23]):

$$M_{^{31}P}(t) = \frac{\gamma_{^1H}}{2\gamma_{^{31}P}} M_0 \left[1 - \cos(\delta_n t)\right] \tag{5.2}$$

where $\delta_{\pm n}$ are defined by:

$$\delta_{\pm 1} = \frac{D_{PH}}{4} \sqrt{2} \sin 2\beta \tag{5.3}$$

$$\delta_{\pm 2} = \frac{D_{PH}}{4} \sin^2 \beta \tag{5.4}$$

β is the angle between r_{PH} and the rotor axis. D_{PH} is the magnitude of the ^{31}P,^{1}H dipolar coupling. This is related to the internuclear distance r_{PH} by:

$$D_{PH} = \frac{\gamma_{^1H}\gamma_{^{31}P}\hbar(\mu_0/4\pi)}{2\pi r_{PH}^3} \tag{5.5}$$

As in the static case, D_{PH} can be directly determined from the Pake-like powder pattern. However, for the $n = \pm 1$ sideband matching, the maximum splitting in the powder pattern is found at $\beta = \pi/4$, and the separation of the horns of the powder pattern will be $D_{PH}/\sqrt{2}$. For the $n = \pm 2$ condition, the maximum splitting in the powder pattern is found at $\beta = \pi/2$, and the separation of the horns of the powder pattern will be $D_{PH}/2$. Thus, distance determination by this technique is very straightforward because there is no

need to fit to numerical simulations since the dipolar coupling can be directly extracted from the line splitting of the powder pattern. The measured dipolar coupling constants were 16.76 kHz for SnHPO$_3$ (Figure 5-12 (b)) and 5.70 kHz for SnHPO$_4$ (Figure 5-14 (f)), corresponding to P,H distances of 1.43 Å (direct P–H bond) and 2.03 Å (P–O–H unit) respectively.

The reproducibility of the distance determination using this technique was studied by repeating experiments at the $n = \pm 1$ conditions with different spinning speeds. Four results (Table 5-3) at two spin rates of 15 and 18 kHz gave distances within the range 1.41–1.43 Å for SnHPO$_3$, and so it may be concluded that the average of r_{PH} is 1.42 ± 0.01 Å, in good agreement with the P–H distance reported for MgHPO$_3$ · 6H$_2$O [24] of 1.47 Å.

Table 5-3 Dipolar coupling constants (D_{PH}) and the internuclear distances (r_{PH}) for SnHPO$_3$ determined using the variable contact time experiment. ^{31}P RF-field was set to 83.33 kHz. It is assumed that ΔJ is negligible.

Spin rate / kHz	^{1}H RF-field strength / kHz	Sideband no.	Separation of the horns / Hz^a	D_{PH} / Hz^b	r_{PH} /Å^c
15	94.82	+1	11849	16758	1.43
	71.84	-1	12004	16976	1.42
18	94.82	+1	12109	17123	1.42
	66.08	-1	12207	17263	1.41

^{a} ± 160 Hz.
^{b} ± 215 Hz.
^{c} ± 0.01 Å

The results for SnHPO$_4$ are in Table 5-4. The distance range was 2.02–2.07 Å, obtained at spin rates of 12 and 15 kHz, corresponding to an average r_{PH} = 2.05 ± 0.03 Å. The result is consistent with the values in the range of 2.07-2.27 Å reported from crystallographic studies for SnHPO$_4$ [25] and other phosphate compounds Zr(HPO$_4$)$_2$ [26] and CaHPO$_4$ [27], CaHPO$_4$ · 2H$_2$O [28].

Table 5-4 Dipolar coupling constants (D_{PH}) and the internuclear distances (r_{PH}) for SnHPO$_4$ determined using the variable contact time experiment. ^{31}P RF-field was set to 71.43 kHz. It is assumed that ΔJ is negligible.

Spin rate / kHz	^{1}H RF-field strength / kHz	Sideband no.	Separation of the horns / Hz^a	D_{PH} / Hz^b	r_{PH} /Å^c
12	81.63	+1	4205	5946	2.02
	61.23	-1	3876	5480	2.07
15	81.63	+1	4102	5700	2.03
	58.31	-1	3906	5523	2.07

^{a} ± 160 Hz.
^{b} ± 225 Hz.
^{c} ± 0.03 Å

It is important to consider the effect of mis-setting the sideband matching condition, since this is the most likely source of experimental error in this otherwise robust experiment. Following Ref. [8], the relationship between the separation of the horns, S_1, and the mis-set of the Hartmann-Hahn matching condition ($\Delta = v_I - v_s - nv_r$) at the $n = \pm 1$ matching condition is:

$$S_1 = 2\sqrt{\Delta^2 + D_{PH}^2 / 8} \qquad (5.6)$$

If we are in the limit where the mismatch is small compared to the dipolar coupling, the corresponding expression for the dipolar coupling in terms of S_1 can be written:

$$D_{PH} = S_1 \sqrt{2 - (8\Delta / S_1)^2} \approx S_1 \sqrt{2}\left(1 - \frac{2\Delta^2}{S_1^2}\right) \qquad (5.7)$$

A mismatch has the effect of decreasing the apparent dipolar coupling constant for a fixed value of S_1. But (in this limit), the effect is second-order in the ratio Δ / S_1. Moreover, the strong dependence of dipolar coupling on internuclear distance, $D_{IS} \propto r_{IS}^{-3}$,

means that the fractional error on r_{IS} is one-third that of any fractional error in D_{IS}. Note that any mismatch will tend to underestimate r_{IS}.

This is supported experimentally. The mis-setting of 2.8 kHz from exact match for SnHPO$_3$, as shown in Figure 5-10, was chosen since the ^{31}P signal could be observed with a good-signal-to-noise even though this RF field strength was half way from the exact match. As shown in Figure 5-12 (f) and Figure 5-13 (f) at spin rates of 15 and 18 kHz, deliberate mis-settings of 2.8 kHz for SnHPO$_3$ from exact sideband matching resulted in an increase of the separation of the horns, 12451 and 12516 Hz respectively. For the spin rate of 15 kHz, it leads to an increase of *ca.* 5% in the *apparent* dipolar coupling constant and a decrease of only 1.4% in r_{PH}, to 1.404 Å. Similarly, only a 1.1% decrease in r_{PH} is decreased to 1.402 Å is obtained for the mis-setting at the spin rate of 18 kHz. The variation in the dipolar coupling measurement is less than predicted by Equation 5.5 (6 and 7% for a mis-setting at the spin rates of 15 and 18 kHz respectively), which is probably due to a constructive interaction between mismatch and inhomogeneities of the B_1 field; the signal will be strongest from the regions in which these effects have tended to cancel, while little signal will be observed from regions where the overall mismatch is large. Hence there is relatively little advantage to reducing RF inhomogeneities by restricting the sample volume to the centre of the coil. Although this will sharpen the matching profile, allowing the match to be set with greater precision, the robustness of the experiment would not be greatly improved while sensitivity would be significantly worse.

It is also worth noting that the heteronuclear distances are most often measured by Rotation-echo Double-resonance (REDOR) [29]. This "recoupling" method employs very strong π pulses synchronously with the sample rotation and in this way tries to re-introduce the heteronuclear dipolar coupling. However, this method is only suitable for the study of weak heteronuclear dipolar interactions (a few hundred to a few thousand Hertz) since the π pulses are assumed to be very short compared to the sample rotation period, which is hard to realise for high spin rates [30]. This implies that the REDOR technique is perhaps less well adapted to the measurement of strong couplings (such as

those between ^{31}P and ^{1}H). On the other hand, variable contact time experiments under fast spin rates do not suffer from these complication, resulting in the fact the method it is well-suited to the measurement of *strong* couplings. Similar conclusions have been drawn by other workers [8],[31].

As can be seen above, all results (for both SnHPO$_3$ and SnHPO$_4$) are consistent with X-ray diffraction data from related compounds, but it is important to note that XRD was unable to locate the hydrogens in our tin compounds due to the proximity of the heavy tin atoms [9]. It is also important to note that distance measurements by NMR and X-ray diffraction are based on different phenomena. The distance is determined using the electron density distribution in X-ray diffraction whereas NMR can extract the distance from internuclear interactions (based on the nuclei). Thus, the results from the two techniques will not be, in principle, equal; X-ray studies may provide shorter internuclear distances than NMR due to the delocalisation of electrons and the way mobility can affect measurements of dipolar coupling constants [32].

5.2.4   Unusual behaviour under ^{31}P decoupling

The experiments under MAS were performed using the direct polarization pulse sequence with and without CW ^{31}P decoupling during acquisition. Figure 5-15 (a) shows the ^{1}H spectrum of SnHPO$_3$ obtained without CW decoupling. This shows a splitting due to indirect (*J*) coupling to ^{31}P, which is too complicated (see in section 5.2.2). Hence the ^{1}H spectrum acquired under ^{31}P decoupling is expected to be a single peak, corresponding to the unique hydrogen site in the asymmetric unit. However, the proton spectrum acquired with CW ^{31}P decoupling, as shown in Figure 5-15 (b), shows *two* peaks with a splitting of 520 Hz. This unexpected result is more pronounced at a higher field (11.7 T), as shown in Figure 5-15 (e). The splitting broadens to about 1520 Hz under CW decoupling.
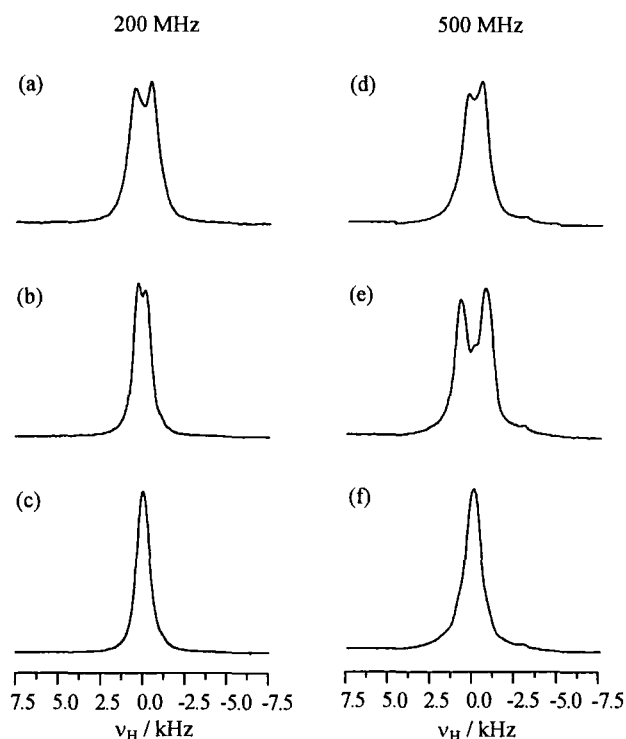
200 MHz   500 MHz

(a)   (d)

(b)   (e)

(c)   (f)

┌──┬──┬──┬──┬──┬──┐   ┌──┬──┬──┬──┬──┬──┐
7.5 5.0 2.5 0.0 -2.5 -5.0 -7.5   7.5 5.0 2.5 0.0 -2.5 -5.0 -7.5
      v_H / kHz v_H / kHz

Figure 5-15 ^{1}H spectra of SnHPO$_3$ at (a-c) 200.13 MHz, (d-f) 499.97 MHz. The ^{1}H spectra in (a) and (d) were obtained without CW decoupling, whereas (b) and (e) were studied under CW decoupling. TPPM decoupling was employed to acquire the ^{1}H spectra in (c) and (f). The sample was spinning at the magic angle with spin rates of 12.5 kHz (a-c) or 18 kHz (d-f)). The ^{31}P RF field strength was 83 kHz (b, c) or 70 kHz (e,f). The TPPM tip angle was set to ~180° with a phase difference of 15°.

It has been known that under CW decoupling, e.g. off-resonance, insufficient decoupling field strength could lead to incomplete decoupling and residual line splitting [33,34]. Therefore, to investigate the line splitting observed above, the field strengths of CW decoupling and off-resonance magnitude were taken into account.

Figure 5-16 displays the splitting in the proton spectra as a function of ^{31}P RF field strength (CW decoupling) on the 200 MHz spectrometer. The separation of the peaks was strongly dependent on the decoupling power (Figure 5-16 (b)). The line splitting did not vanish at the decoupling power of 83 kHz. Note that the maximum safe decoupling power is 83 kHz for the probe used (4 mm rotor). Although using such a high decoupling may remove the splitting, this can also lead to undesired heating of the probe (especially when the acquisition time is too long).
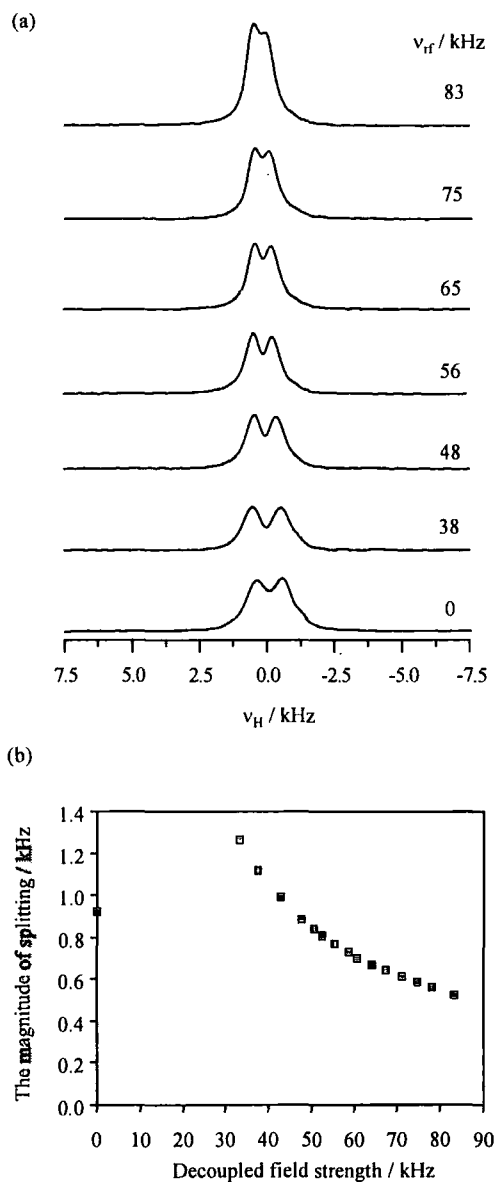
Figure 5-16 (a) ^{1}H spectra at 200.13 MHz under CW decoupling as a function of ^{31}P CW-decoupling power at a spin rate of 12.5 kHz. Direct polarisation was employed. The acquisition parameters were: recycle delay 120 s; number of transients 4. (b) The magnitude of the splitting (from deconvolution) as a function of ^{31}P CW-decoupling power.

An effect of off resonance CW decoupling on the line splitting was further investigated on the 200 MHz spectrometer. Figure 5-17 shows a series of proton spectra where the ^{31}P off-resonance frequency was varied from 0 to 100 kHz at a fixed decoupling power of 83 kHz. As expected, the splittings were a function of the resonance offset (Figure 5-17 (b)), with a greater magnitude of the splitting at higher off-resonance frequencies. The asymptotic value of the splitting is ca. 900 Hz. However, even with on-resonance decoupling the line splitting is still clearly pronounced. Note that good CW decoupling of the heteronuclear dipolar interaction requires that the irradiated nuclei is on-resonance [34,35]. Experimentally, off-resonance effects are normally minimized by optimising the position of the ^{31}P transmitter frequency, which straightforward for the case of $SnHPO_3$ since there is only one phosphorus resonance.

The effect of the ^{31}P off-resonance frequency (an offset of the ^{31}P transmitter) on the magnitude of the splitting of ^{1}H spectrum under 70 kHz CW decoupling power was also studied at higher field (11.7 T), as shown in Figure 5-18. The splitting on-resonance is *ca.* 1500 Hz. This splitting increases with increasing off-resonance frequency from 0 to 10 kHz, but (in contrast to the case shown in Figure 5-17) the splittings significantly decrease with a further increase in off-resonance frequency. For the negative off-resonance frequency, the splittings reduce with increasing the off-resonance frequency from 0 to -110 kHz. The magnitudes of the splitting on the two sides of resonance (plus and minus) are not symmetrical. This is probably due to the size of the phosphorus shielding anisotropy ($\zeta = -68$ ppm) and the low asymmetry, since the phosphorus nuclei are in a nearly axial symmetric environment (see Chapter 4). From Figure 5-18, it is obvious that the intensities of the peaks at lower frequency and higher frequency are not generally equal.
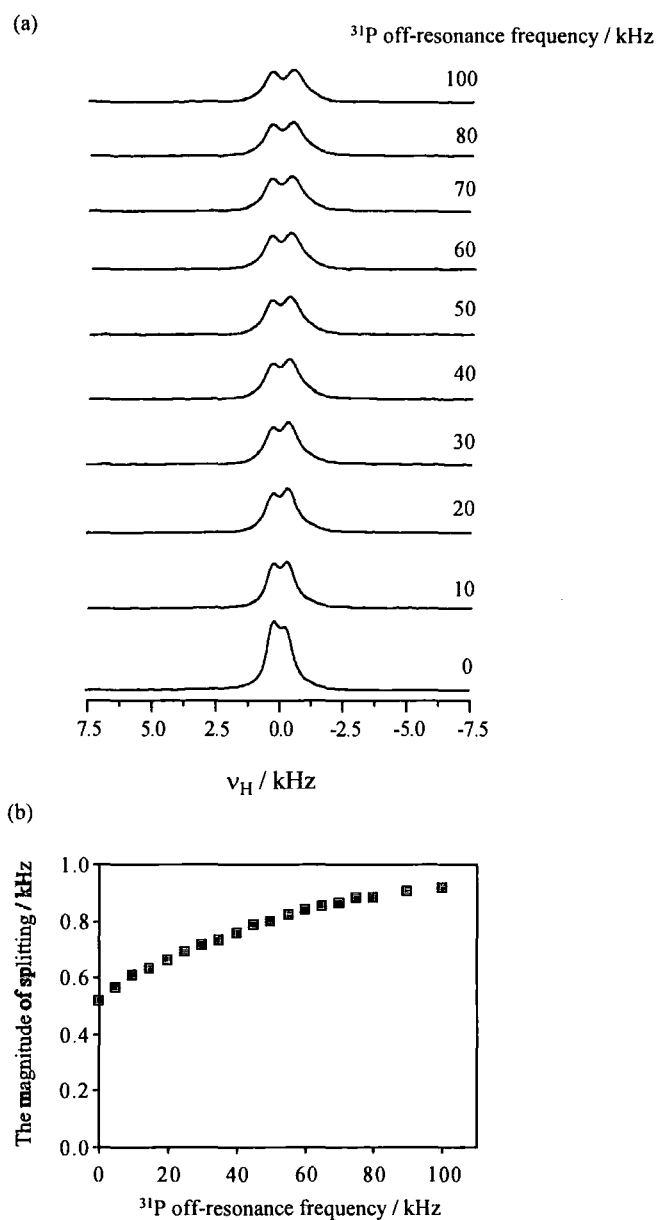
(a)

^{31}P off-resonance frequency / kHz

100

80

70

60

50

40

30

20

10

0

| 7.5 | 5.0 | 2.5 | 0.0 | -2.5 | -5.0 | -7.5 |

ν_H / kHz

(b)

The magnitude of splitting / kHz

1.0					
0.8					
0.6					
0.4					
0.2					
0.0					
0	20	40	60	80	100

^{31}P off-resonance frequency / kHz

Figure 5-17 (a) ^{1}H spectra at 200.13 MHz under CW decoupling as a function of ^{31}P resonance offset. Direct polarisation was employed. The decoupling field strength for all spectra was set to 83 kHz, and the spin rate was 12.5 kHz. The acquisition parameters were: recycle delay 120 s; number of transients 4. (b) The magnitude of the splitting as a function of ^{31}P off-resonance frequency.
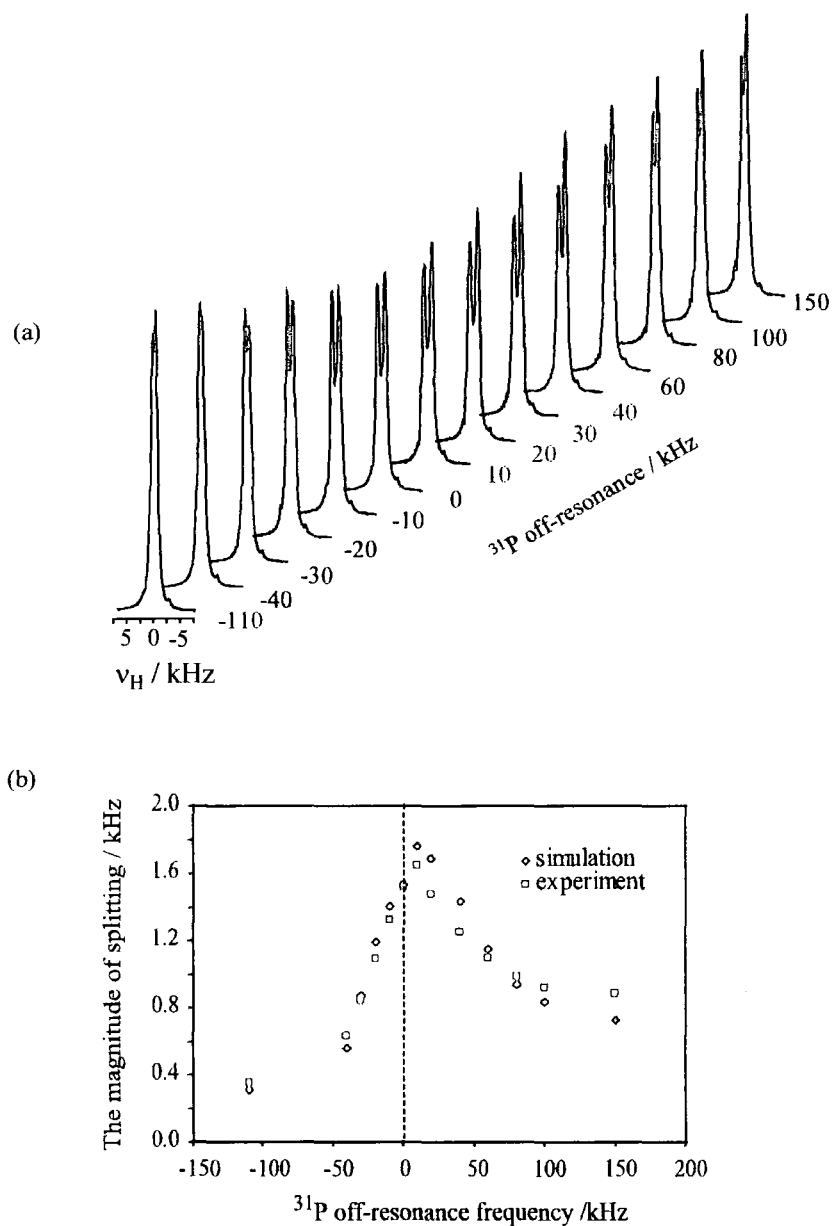
Figure 5-18 ^{1}H spectra at 499.70 MHz under CW decoupling as a function of ^{31}P off-resonance frequency. Direct polarisation was employed. The decoupling field strength for all spectra was set to 70 kHz, and the spin rate was 18 kHz. The acquisition parameters were: recycle delay 120 s; number of transients 4. (b) Plots of the magnitude of the splitting as a function of ^{31}P off-resonance frequency, including results from simulations (see Figure 5-22).

The dependence of the ^{1}H splitting at 500 MHz on the ^{31}P RF field strength (CW decoupling) is shown in Figure 5-19. The line is still split and rather broad even with the highest decoupling field strength. The magnitude of the splitting increases with the decrease of RF field strength. In addition, another unexpected result was found in this study; a new peak was seen in the middle of the spectrum. This peak was more noticeable as the RF field strength was decreased, which this may be explained by the inhomogeneity in B_1. At the moment we cannot explain satisfactorily the origin of this peak.
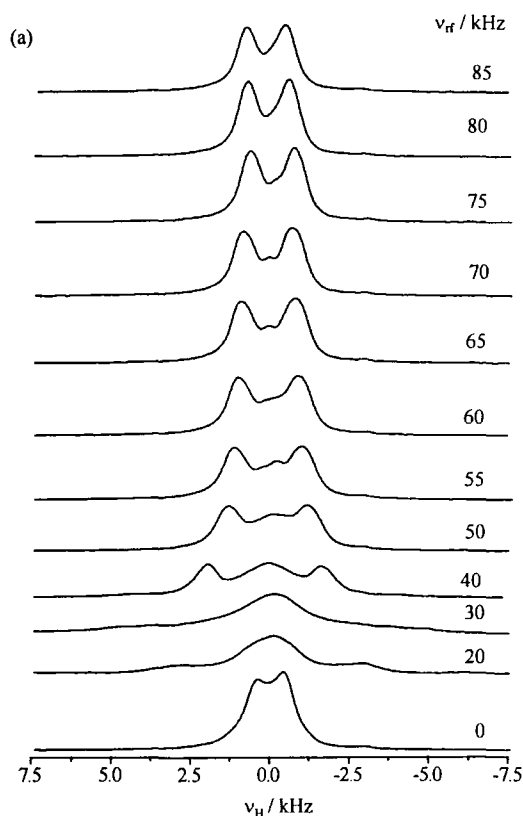
Figure 5-19 (a) ^{1}H spectra at 499.70 MHz under CW decoupling as a function of ^{31}P CW-decoupling power at a spin rate of 18 kHz. Direct polarisation was employed. The acquisition parameters were: recycle delay 120 s; number of transients 4.

In order to understand the behaviour of unusual splitting, simulations ^{1}H spectra under CW decoupling have been carried out using SIMPSON [16], concentrating on the observed behaviour at the higher field. In all simulations, the anisotropy of the dipolar tensor was set to 16.8 kHz, the coupling constant was 693 Hz, the decoupling power 70 kHz, and shielding anisotropy was –68 ppm. Axially symmetry was assumed.

Since the splitting is possibly orientation-dependent, one of the important parameters which needs to be considered first is the angle β (which is the angle between the dipolar and shielding tensors). The aim of specifying angle β is to test the accuracy of the simulation model that should be in agreement with the experimental model. Thus, the first set of proton spectra was done under fixed ^{31}P CW decoupling (70 kHz) and spin rate (18 kHz).

Figure 5-20 show the simulation of the dependence of the proton spectra on the relative orientation of the dipolar tensor. It can clearly be seen that there is a strong dependence of the magnitude of splitting on the angle β. At the angle β of 0, the magnitude of the splitting (ca. 1520 Hz) for the simulated proton spectrum is consistent with the experimental result (ca. 1550 Hz). This indicates that the simulation model is correct, and can reproduce the experimental result. The result also strongly suggests that the dipolar coupling tensor and the shielding tensor are coaxial. Therefore, all the simulated results in this section the angle β was set to 0.

Note that the splitting cannot be seen at the angle β of 54.74°. This is probably due to the employed line broadening 400 Hz, which is quite large compared to the scalar coupling.
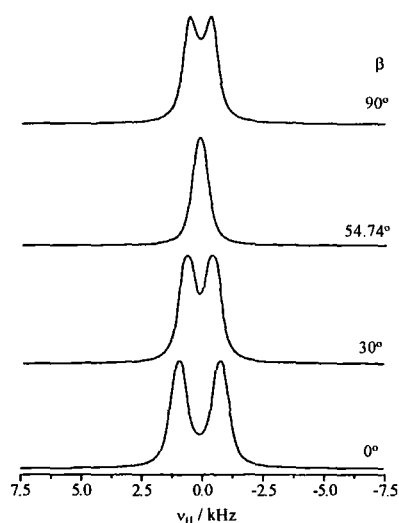
Figure 5-20 Dependence of the splitting on the orientation, β, of the dipolar tensor relative to the shielding tensor. Simulation parameters: the anisotropy of the dipolar tensor was set to 16.8 kHz, the coupling constant was 693 Hz, the decoupling power 70 kHz, and shielding anisotropy was set to -68 ppm and assumed to be axially symmetric.

Figure 5-21 presents ^{1}H spectra as a function of the decoupling field strength. The magnitudes of the splitting from the simulation are in agreement with the experiments, as shown in Figure 5-21 (b), but the central lines are not reproduced by the simulation. The difference may be explained by considering the inhomogeneity in B_1 since this parameter has not been included in the simulations. It would be very difficult to include this parameter in the simulation, so that the real system is more complicated than the simulation. We have not emphasised this problem in this Chapter. On the other hand, we concentrated on investigating and understanding the anomalous behaviour of the splitting under CW decoupling.
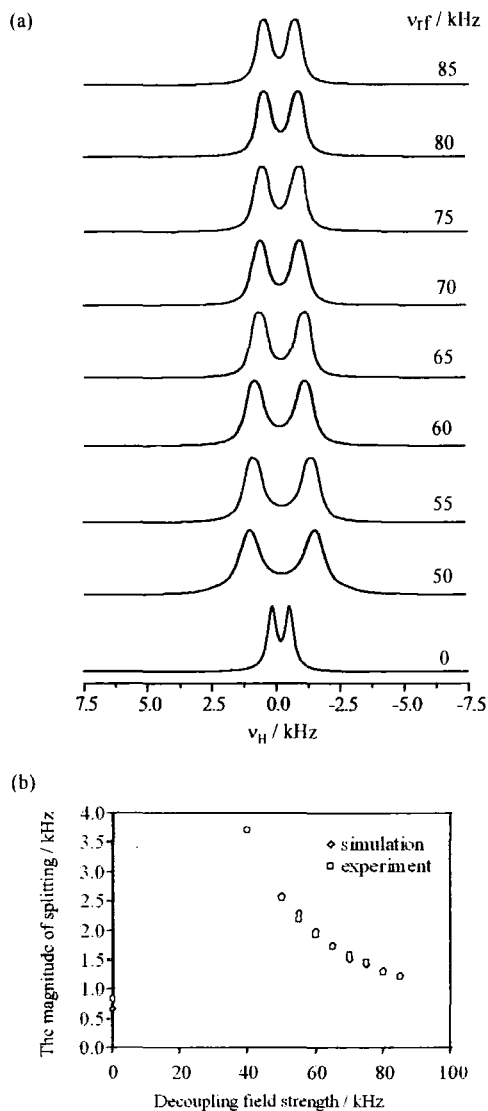
Figure 5-21 (a) Simulated CW-decoupled ^{1}H spectra at 499.97 MHz as a function of RF decoupling power. Other simulation parameters: ^{31}P-^{1}H dipolar interaction 16.8 kHz, ^{31}P shielding anisotropy 13.8 kHz in magnitude, ^{31}P shielding asymmetry 0, spin rate 18 kHz, line broadening 400 Hz. (b) comparison of the splitting of ^{1}H spectrum derived from simulation and experimental results.

The influence of ^{31}P off-resonance decoupling on the magnitude of the splitting was also studied using SIMPSON, as shown in Figure 5-22. The magnitude of the splitting from the simulated results is in good agreement with the experimental results. Comparison of the values is shown in Figure 5-18 (b). However, the intensities of the peaks from the simulated results are equal, which differs from the experimental results (Figure 5-18 (a)).
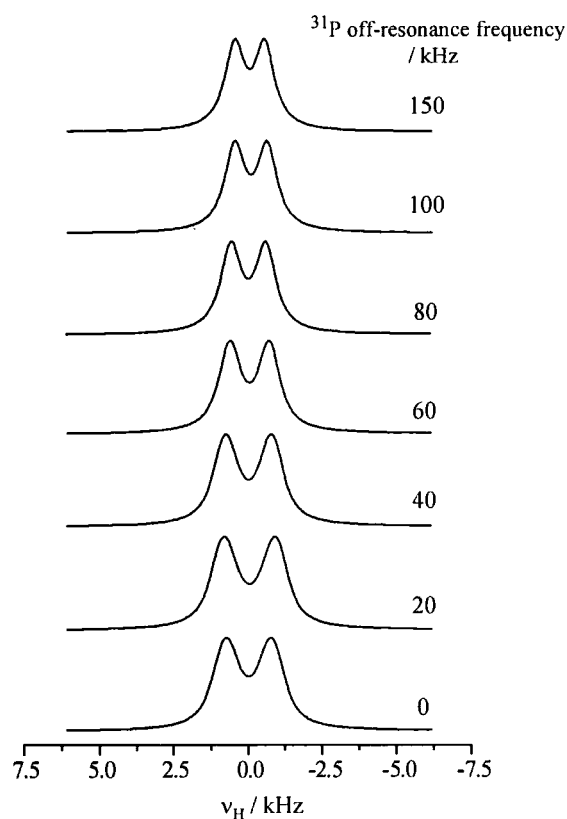
Figure 5-22 Simulated ^{1}H spectra at 499.97 MHz under CW decoupling for a variable of ^{31}P off-resonance frequency. Simulation parameters: ^{31}P-^{1}H dipolar interaction 16.8 kHz, ^{31}P shielding anisotropy 13.8 kHz in magnitude, ^{31}P shielding asymmetry 0, J_{PH} coupling constant 693 Hz, RF field strength 70 kHz, spin rate 18 kHz, line broadening 400 Hz.

Clearly, numerical simulation of the two spin ^{1}H, ^{31}P spin system reproduces the experimental behaviour of the magnitude in the splitting (Figure 5-21 (b)), which is encouraging, but provides little physical insight. Following Ref [11], we can write the spin Hamiltonian in the doubly rotating frame for this problem, using S to denote the observed ^{1}H spin and I for the irradiated ^{31}P, as:

$$H = [\omega_D(\Omega_D) + J(\Omega_J)/2] \cdot 2I_z S_z + \omega_S(\Omega_S)S_z + \omega_I(\Omega_I)I_z + \omega_{rf}I_x \qquad (5.8)$$

where ω_D, ω_J, ω_S and ω_I are the strengths of the dipolar and indirect coupling interactions, and the offsets from the transmitter frequency of the S and I spins respectively (expressed in common frequency units). These interactions are all potentially orientation-dependent, with Ω_i representing the set of Euler angles relating the principal axis system of the tensor interaction I with the laboratory frame. ω_{rf} is the nutation rate of the I spins under CW decoupling. The heteronuclear J interaction is straightforwardly incorporated into the previous treatment [11] by replacing the dipolar coupling with the effective coupling term $\omega_{D,eff}(\Omega_{D,J}) = \omega_D(\Omega_D) + J(\Omega_J)/2$, noting that this effective interaction now contains an isotropic component (unlike the dipolar interaction) and that the principal axis systems of the interactions are likely to be co-incident i.e. $\Omega_D \approx \Omega_J$.

As previously shown [11], if it is assumed that ω_{rf} is significantly larger than the other interactions, second-order perturbation theory can be used to derive the frequencies of the two strong transitions corresponding to the S spin resonance:

$$\omega \approx \omega_S(\Omega_S) \pm \frac{\omega_{D,eff}(\Omega_{D,J})\omega_I(\Omega_I)}{\omega_{rf}} \qquad (5.9)$$

Under conditions of magic-angle spinning, the corresponding centreband frequencies are determined by the time average of these frequencies:

$$\langle\omega\rangle \approx \langle\omega_S(\Omega_S)\rangle \pm \frac{\langle\omega_{D,\textit{eff}}(\Omega_{D,J})\omega_I(\Omega_I)\rangle}{\omega_{\mathrm{rf}}} \tag{5.10}$$

We assume that $2\pi v_r \ll \omega_{rf}$, i.e. the averaging due to the MAS and RF irradiation can be treated independently. The first term in Equation 5.10 is simply the isotropic chemical shift of the observed S spin, while the second is a cross-term between the (effective) heteronuclear coupling and the shielding of the I spin. This cross between an effective rank 0 + rank 2 interaction and another rank 2 interaction will contain terms of rank $0 + 2 + 4$. Under normal decoupling conditions, the resulting isotropic term is negligibly small and the rank 2 term is eliminated (like the anisotropy of ω_S) by the MAS, but the rank 4 terms survives the averaging. At finite decoupling power (ω_{rf}), this term separates the otherwise degenerate transitions, and the S spin spectrum from an individual crystallite appears as a doublet. The size of the splitting depends on the crystallite orientation (in addition to the relative orientations of the tensor interactions) and so the spectrum of a powdered sample appears as a Pake-like double-peaked lineshape.

Thus the broadening rank 4 term arises from the cross-term between the chemical shift anisotropy of the decoupled (I) spin and the anisotropy of the coupling (dipolar + J) between I and S. Hence, it is unsurprising that these effects are not widely observed in ^{1}H-decoupled spectra, due to the weakness of the ^{1}H CSA. In this case, however, we are decoupling ^{31}P, which has a substantially larger shielding anisotropy (ζ = -68 ppm), and so these effects are much more prominent. We have also recently observed analogous effects in the $\{^1$H$\}$-^{13}C NMR of fluorine-containing systems; here the ^{1}H–^{19}F dipolar coupling appears, from the viewpoint of the decoupling, as equivalent to a large effective ^{1}H CSA [36]. Furthermore, this is the first sample involving the P,H pair of nuclei, with a resolvable J-coupling (693 Hz), shows the splitting under CW decoupling arising from the second-order recoupling. Note that the model sample studied in Ref [11] is fully ^{15}N labeled tris-(trideuteromethyl)-ammoniumchloride with $J_{NH} \approx 100$ Hz, which does not give an observable splitting in the fully-coupled spectrum at a ^{1}H Larmor frequency of

301.2 MHz. However, the splitting can be seen in a 600 MHz spectrum obtained at a spin rate of 30 kHz [37].

Fortunately, the second-order effects can be averaged out using two-pulse phase modulation (TPPM) decoupling [38]. The sequence consists of the following: application of RF pulses with the flip angle alternating between two phases separated by an angle ϕ. The small phase-alternation reduces the second-order recoupling effect; for TPPM decoupling with the model pulse sequence of $(180^\circ_{+\phi}180^\circ_{-\phi})_N$ with $\phi = \pi/(2N)$ and with N>1. It has been reported [38] that the effect of TPPM depends strongly on the flip angle and the phase difference. The dependence becomes more pronounced at high MAS frequencies. Consequently, these parameters need to be optimized to achieve high resolution under this decoupling sequence.
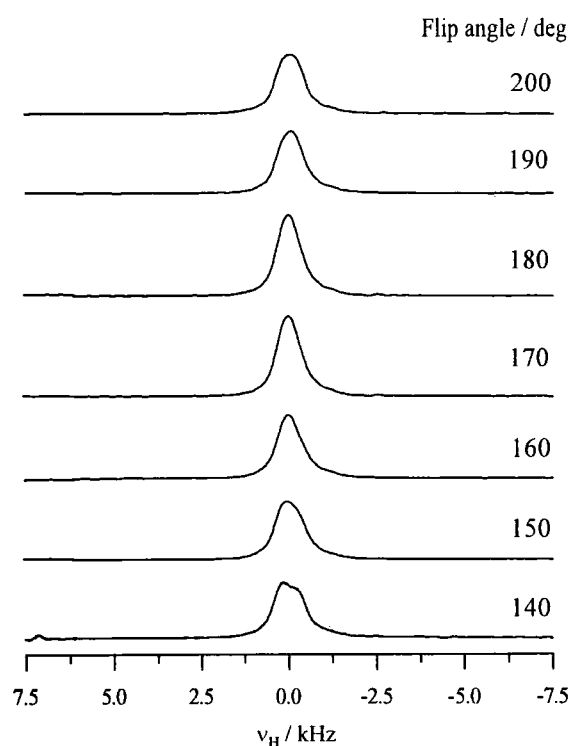
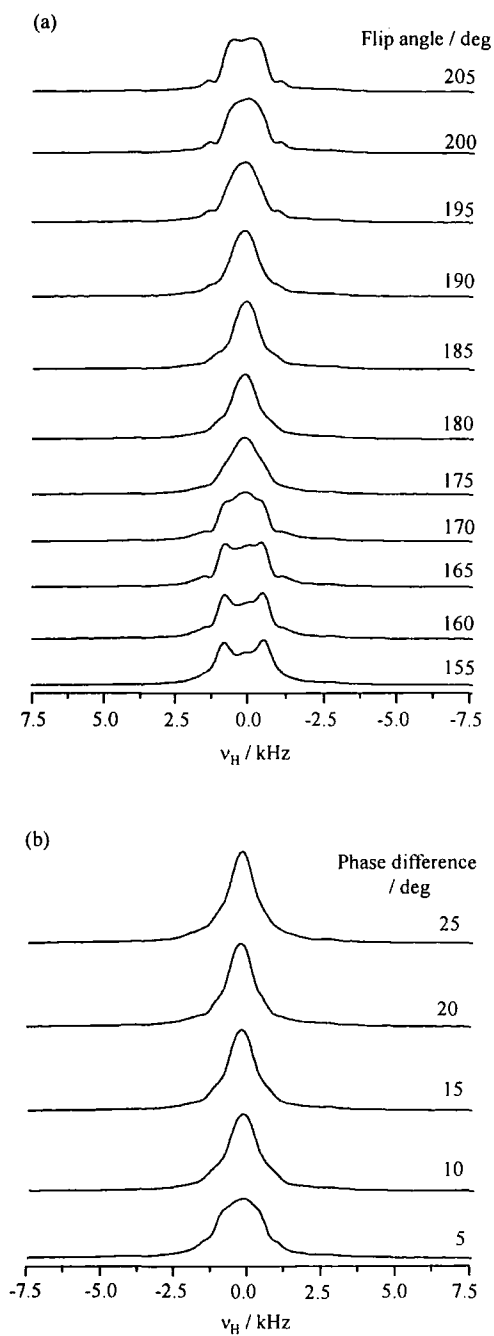**Figure 5-23** Experimental ^{1}H spectra at 200.13 MHz under TPPM decoupling for seven different flip angles from 140° to 200° at fixed phase difference 15°. The decoupling power was set to 83 kHz.

Figure 5-23 illustrates the dependence of the ^{1}H spectrum on the flip angle at the magnetic field of 4.7 T. Clearly, at the flip angle of 180° at fixed phase difference of 15°, the splitting was eliminated. The comparison between the line splitting under TPPM decoupling and CW decoupling is shown in Figure 5-15 (b) and (c). The TPPM sequence has succeeded in eliminating any observed splitting.

The dependence of the splitting on the flip angle and phase difference at 500 MHz are presented in Figure 5-24. The experiments were studied at 70 kHz RF field strength and 18 kHz spin rate. It is obvious that both flip angle and the phase difference at higher field are very sensitive parameters. The optimal flip angle was set to 180° and the optimal phase difference was 15°. However, even with the precise setting of both flip angle and phase difference the ^{1}H spectrum is still not a simple single line.

As can be seen, the use of TPPM decoupling under MAS can reduce the line-broadenings and splittings only at lower fields (4.7 T), but is not totally successful at higher fields (11.7 T). The latter fact is attributed to the increase in magnitude (in frequency units) of the ^{31}P shielding anisotropy. Hence, a new decoupling sequence for nuclei with large CSAs under MAS is required and this means a challenge for current decoupling methods in solid-state NMR.

Figure 5-24 Experimental ^{1}H spectra at 499.70 MHz under TPPM decoupling for (a) seven different flip angles from 155 deg to 205 deg at a fixed phase difference 15° and (b) five different phase differences from 5 deg to 25 deg at a fixed flip angle 180°. The decoupling power was set to 70 kHz. The spin rate was 18 kHz

5.3   Conclusions

Isolated spin systems present both opportunites and complications for solid-state NMR. It has been shown that reliable internuclear distances of P-H for SnHPO$_3$ and P-O-H for SnHPO$_4$ can be determined from a variable contact time experiment under a fast spin rate, which has provided the internuclear distances 1.42 ± 0.01 Å (SnHPO$_3$) and 2.05 ± 0.03 Å (SnHPO$_4$). This technique is very powerful for precisely evaluating the P,H internuclear distances in the phosphate and phosphite compounds, since they cannot be readily measured by X-ray diffraction.

It has been also found that the second-order cross term between the CSA of ^{31}P (in SnHPO$_3$) and the (effective) heteronuclear dipolar coupling is the significant contribution to the residual line splitting and also linewidth under CW decoupling of isolated two-spin systems. Since this residual line splitting arises from the coupling of two second-rank tensors it will not be removed under MAS conditions because rank 4 terms remain. However, use of an efficient decoupling sequence (such as TPPM) can remove the second-order recoupling effect. This was successful at a low magnetic field (4.7 T), but not completely for a higher magnetic field (11.7 T) because of the increase in ^{31}P shielding anisotropy.

5.4   References

[1]   R.K. Harris, K.J. Packer, A.M. Thayer, J. Magn. Reson. 62 (1985) 284.
[2]   H. Bai, R.K. Harris, J. Magn. Reson. 96 (1992) 24.
[3]   S. Hediger, Ph.D Thesis, ETH Zurich (1997).
[4]   B.H. Meier, Chem. Phys. Lett. 188 (1992) 201.
[5]   S. Ding, C.A. McDowell, C. Ye, J. Magn. Reson. A 109 (1994) 6.
[6]   S.R. Hartmann, E.L. Hahn, Phys. Rev. 128 (1962) 2042.
[7]   M. Mehring, Principles of High Resolution NMR in Solids, 2nd ed., Springer-Verlag, Berlin, 1983.
[8]   P. Bertani, J. Raya, P. Reinheimer, R. Gougeon, L. Delmotte, J. Hirschinger, Solid State Nucl. Magn. Reson. 13 (1999) 219.
[9]   R.C. McDonald, A.R. Erisks, Inorg. Chem. 19 (1980) 1237.
[10]   K. Schmidt-Rohr, H.W. Spiess, Multidimensional Solid-State NMR and Polymers, Academic Press, London, 1994.
[11]   M. Ernst, S. Bush, A.C. Kolbert, A. Pines, J. Chem. Phys. 105 (1996) 3387.

[12]   M. Carravetta, M. Edén, X. Zhao, A. Brinkmann, M.H. Levitt, Chem. Phys. Lett. **321** (2000) 205.

[13]   K. Takegoshi, J. Mizokami, T. Terao, Chem. Phys. Lett. **341** (2001) 540.

[14]   J.R. Ascenso, L.H. Merwin, H. Bai, in-house sideband fitting program, University of Durham.

[15]   G. Mavel, Ann. Repts NMR Spectrosc. **5B** (1973) 1.

[16]   M. Bak, J.T. Rasmussen, N.C. Nielsen, J. Magn. Reson. **147** (2000) 296.

[17]   R. Freeman, H.D.W. Hill, J. Chem. Phys. **54** (1971) 301.

[18]   R.K. Harris, Nuclear Magnetic Resonance Spectroscopy, Longman, London, 1987.

[19]   R.E. Mesmer, R.L. Carroll, J. Am. Chem. Soc. **88** (1966) 1381.

[20]   T.C. Farrar, J.L. Schwartz, S. Rodriguez, J. Phys. Chem. **97** (1993) 7201.

[21]   T.R. Eykyn, P.W. Kuchel, Magn. Reson. Med. **2003** (2003) 693.

[22]   D. Sakellariou, P. Hodgkinson, S. Hediger, L. Emsley, Chem. Phys. Lett. **308** (1999) 381.

[23]   X. Wu, K.W. Zilm, J. Magn. Reson. A. **104** (1993) 154.

[24]   D.E.C. Corbridge, Acta Cryst. **9** (1956) 991.

[25]   L.W. Schroeder, E. Prince, Acta Cryst. B. **32** (1976) 3309.

[26]   A.M. Krogh-Andersen, P. Norby, J.C. Hanson, T. Vogt, Inorg. Chem. **37** (1998) 876.

[27]   M. Catti, G. Ferraris, A. Filhol, Acta Cryst. B. **33** (1977) 1223.

[28]   N.A. Curry, D.W. Jones, J. Chem. Soc. A. (1971) 3725.

[29]   T. Gullion, J. Schaefer, Adv. Magn. Reson. **13** (1989) 57.

[30]   C. Jaroniec, B.A. Tounge, C.M. Rienstra, J. Herzfeld, R.G. Griffin, J. Magn. Reson. **146** (2000) 132.

[31]   C.A. Fyfe, A.R. Lewis, J.M. Chézeau, G. Hiltrud, J. Am. Chem. Soc. **119** (1997) 12210.

[32]   R.K. Harris, P.Y. Ghi, R.B. Hammond, C.-Y. Ma, K.J. Roberts, Chem. Comm. (2003) 2834.

[33]   M.M. Maricq, J.S. Waugh, J. Chem. Phys. **73** (1979) 3300.

[34]   D.L. Vanderhart, W.L. Earl, A.N. Garroway, J. Magn. Reson. **44** (1981) 361.

[35]   D.L. Vanderhart, G.C. Campbell, J. Magn. Reson. **134** (1998) 88.

[36]   G. Antonioli, D.E. McMillan, P. Hodgkinson, Chem. Phys. Lett. **344** (2001) 68.

[37]   M. Ernst, J. Magn. Reson. **162** (2003) 1.

[38]   A.E. Bennett, C.M. Rienstra, M. Auger, K.V. Lakshmi, R.G. Griffin, J. Chem. Phys. **103** (1995) 6951.

CHAPTER 6

MULTINUCLEAR MAGNETIC RESONANCE STUDIES OF SOLID SILVER COMPOUNDS

6.1   Introduction

Silver(I) compounds are of interest to a wide range of scientists including chemists and biochemists. Silver(I) exhibits a rich biological chemistry [1], forming the basis of a widely used antibacterial agent and a transcriptional initiator in plants and animals. The action of silver ion effectively prevents breeding of bacteria while being harmless for humans. Inorganic silver-based agents are used for tile, tableware, silverware, dental material and sanitary ware. However, many silver compounds are light-sensitive to the point that often X-ray crystallographic information cannot be obtained.

For various reasons, silver is an attractive element for high-resolution solid-state NMR. Direct observation of Ag NMR signals is advantageous since the Ag chemical shift (a range of ~ 1000 ppm) is very sensitive to the chemical environment of the nucleus. Furthermore, silver has two active isotopes, ^{107}Ag and ^{109}Ag, with spin ½ (see Table 6-1). Most NMR studies have involved the ^{109}Ag nucleus because of its higher magnetic moment, and so even though its 48.16% natural abundance is slightly less than that of ^{107}Ag, its receptivity is about 1.4 times greater. Thus, solid-state NMR studies of silver are very helpful understanding areas from fast ion conducting glasses to organometallic complexes of biological significance.

Table 6-1 NMR parameters of the nuclei ^{107}Ag and ^{109}Ag [2].

Isotope	Natural abundance (x / %)	Magnetic moment (μ/μ_N)	Magnetogyric ratio (γ / 10^7rad T^{-1} s^{-1})	Relative receptivity D^P/ 10^{-5}	D^C
^{107}Ag	51.839	-0.1969	-1.0889	3.44	0.205
^{109}Ag	48.161	-0.2264	-1.2519	4.86	0.290

D^P and D^C are the receptivities relative to ^{1}H and ^{13}C respectively.

The main difficulty of silver NMR arises from the low magnetogyric ratio, and so low sensitivity. Moreover, the spin-lattice relaxation time (T_1) is often extremely long for solid silver compounds, usually greater than one minute, which implies long delays between pulses. Thus, the observation of silver-109 signals in solids can be a serious challenge [3,4].

The problem of long relaxation times can be alleviated, to some degree, by use of cross-polarisation (CP) from ^{1}H. However, only a few ^{109}Ag CPMAS investigations have been reported to date [1,5-9] (see literature survey). Moreover, a high proportion of the reports for ^{109}Ag is related to silver-containing glasses (no protons), where silver ions display high ionic mobility resulting in shorter relaxation times, so it is easy to observe. The chemical shift anisotropies ($\Delta\sigma$) of the small number of previously reported systems [1,7,9] cover a range of 500–2000 ppm in magnitude, which results in the appearance of several spinning sidebands at typical spin rates.

In this chapter, the measurement and interpretation of the ^{109}Ag CP/MAS spectra of a number of silver(I) compounds are reported. The study was carried out in order to gain a better understanding of the relationship between the structure of silver complexes (where the crystal structures have been known already) and the observed ^{109}Ag NMR parameters, and to extract the structural information from the NMR studies. The results will be presented in three sections: the first section will involve diammine silver(I) complexes, the second will report on silver(I) nitrate complexes with various ligands in silver(I)-cations, and the last will discuss some silver phosphate compounds. Carbon-13, nitrogen-15 and phosphorus-31 NMR studies are also included in this chapter.

6.2   Literature Survey

As a result of the low sensitivity, only a limited number of [109]Ag NMR studies have been reported in the literature, and most of these have dealt with Ag compounds in solution. Results from solution-state [109]Ag NMR have been summarized by Mann [10].

In solid-state NMR studies, the technique of cross-polarisation, transfer of magnetisation from protons, can reduce the problems associated with long T_1 and lack of sensitivity. The signal enhancement could be ~21 (γ_H / γ_{Ag}), and the experiment time can also be decreased since the recycle delay is governed by the T_1 of protons. As previously described in Chapter 2, in the CP experiment the transfer occurs during the contact time, when both radio frequencies are being transmitted. The CP experiment can be achieved when the Hartmann-Hahn matching condition, $\gamma_H B_{1H} = \gamma_{Ag} B_{1Ag}$, is satisfied. The power requirement for silver to fulfill the matching condition is technically much more demanding than for commonly used nuclei like ^{13}C due to the large value of B_{1Ag} required. Thus, the power handling capability of the probe used is of significance [3,4].

The first [109]Ag CP/MAS spectra have been reported by Merwin and Sebald [7]. [109]Ag CP/MAS spectra of silver acetate, $(CH_3CO_2)Ag$, silver lactate, $[CH_3CHC(OH)CO_2]Ag$ and silver acetylatonate, $(C_5H_7O_2)Ag$, have been studied. It has been found that isotropic chemical shifts cover quite a wide range of 33–472 ppm. Most silver compounds required long contact times, *ca.* 40–50 ms. After the study of various possible CP set-up compounds, silver lactate has been suggested as a standard (chemical shifts are 210.7, 219.7, 320.2 and 345.9 ppm referenced to $AgNO_3$ in H_2O). Silver acetate can be also used as the secondary reference (382.7 and 401.2 ppm with respect to $AgNO_3$ in H_2O) [1]. Nevertheless, both these compounds give more than one signal in NMR (due to crystallographic inequivalencies) and are, moreover, light sensitive. Very recently silver methanesulfonate, $AgSO_3CH_3$, has been found to be a suitable standard for solid-state NMR [11]. The [109]Ag chemical shift of this solid is 87.2 ppm with respect to a saturated solution of $AgNO_3$. The signal is easily seen at a contact time of 10 ms. This compound

shows no air sensitivity and very weak light sensitity. In addition, the spinning sidebands are eliminated at a spin rate of 4 kHz (because of a small CSA).

The first examples of a solid acid catalyst, trisilver dodecatungstophosphates ($Ag_3PW_{12}O_{40} \cdot 6H_2O$), have been observed by using [109]Ag MAS NMR [8]. The [109]Ag NMR spectra, consisting of a single peak at 30 ppm, indicates homogeneous microenvironments of Ag^+ ions coordinated with water molecules.

Fijolek et al. [1,5,6] carried out a detailed study of silver thiolates and related compounds using CPMAS NMR. It was observed that [109]Ag NMR is remarkably sensitive to differences in Ag environment; small differences in bond lengths and angles result in very different isotropic shifts. The chemical shifts are in the range of 826–1228 ppm and the silver sites also show a significant range in their CSA, with values of 569–2120 ppm reported for two- and three- coordinated Ag thiolates in Ref. [1].

Rammial et al. [9] reported the [109]Ag CPMAS NMR spectrum for a monomeric imidazol-2-yldine-silver(I) chloride complex, which contains single peak at 532 ppm. The shielding tensor reveals a large CSA ($\Delta\sigma = 1798$ ppm) and the silver environment is nearly axially symmetric, arising from the linear Cl-Ag-Cl geometry.

6.3   Experimental Considerations

The spectrometers used to acquire silver-109 signals in this work were (a) Varian UnityPlus 300, and (b) Varian InfinityPlus 500. A 7 mm double resonance HX MAS probe and a 7.5 mm double resonance HX MAS solids probe (equipped with an external tuning box for frequencies below ^{15}N) were employed with the Varian UnityPlus 300 and Varian InfinityPlus 500 spectrometers respectively. A 9 M aqueous solution of $AgNO_3$ was used as a standard reference for convenience. The chemical shift is set to 0.0 ppm. The frequencies of the silver nuclei on the two spectrometers are 13.97 MHz and 23.27 MHz respectively. (For ^{13}C, ^{15}N and [77]Se, the frequencies of the individual nuclei, reference compounds and probes used are stated in Chapter 3.)

For the Varian UnityPlus 300 spectrometer, ^{39}K is more amenable than ^{109}Ag because T_1^K < T_1^{Ag} and it gives a sharper signal, so the 90° pulse duration was determined using a solution of KCl. It was assumed that, with the spectrometer in the same configuration but tuned to ^{109}Ag, the pulse duration would be the same (since ^{39}K and ^{109}Ag have similar resonance frequencies: 14.00 and 13.97 MHz, respectively). A ^{109}Ag radiofrequency power equivalent to ca. 36 kHz (equivalent to 7 μs 90° pulse duration) was employed. After finding the power setting, $AgNO_3$ solution was used to set the reference signal. The Hartmann-Hahn match condition was determined by linearly scaling the ^{1}H field for a known 90° pulse (using adamantane) to give a 90° pulse duration equal to that determined for ^{109}Ag via ^{39}K of the KCl solution. It is worth noting that B_{1Ag} (equivalent to 0.02 T at the RF field of 36 kHz) has to be very high compared to B_{1H} (0.0008 T) to achieve the Hartmann-Hahn match condition.

On the other hand, on the Varian InfinityPlus 500 spectrometer, the 90° pulse duration was directly determined using the ^{109}Ag signal of an $AgNO_3$ solution, and a power of ca. 17 kHz (equivalent to 15 μs 90° pulse duration). KCl was not used for this spectrometer because the tuning condition for the probe used required the exact resonance frequency of ^{109}Ag for setting the 90° pulse duration. Besides, using $AgNO_3$ gave a sensible signal-to-noise and linewidth. The 90° pulse duration for protons was found by linearly scaling the power setting required for the 90° proton pulse on adamantane. The Hartmann-Hahn match condition was directly optimised from the sample.

Both the optimum recycle delay and the optimum contact time were found directly from proton and silver signals on the sample, respectively. The recycle delay was determined by a variable recycle-delay-time experiment and checked by measurement of T_1^H where appropriate. The optimum contact time was found by arraying this parameter on each sample and choosing that giving the greatest signal intensity.

6.4   Results and Discussions

6.4.1   Silver(I) Amine Complexes

A series of three silver amine complexes were studied, namely diammine silver(I)-nitrate, [Ag(NH$_3$)$_2$]NO$_3$, diammine silver(I)-sulphate, [Ag(NH$_3$)$_2$]$_2$SO$_4$ and diammine silver(I)-selenate, [Ag(NH$_3$)$_2$]$_2$SeO$_4$. The [Ag(NH$_3$)$_2$]NO$_3$, [Ag(NH$_3$)$_2$]$_2$SO$_4$ and [Ag(NH$_3$)$_2$]$_2$SeO$_4$ are the products of reactions between silver(I) nitrate, silver(I) sulphate and silver(I) selenate, respectively, and concentrated aqueous ammonia. The microcrystalline products are light sensitive.

Crystal structure data

The nitrate complex, [Ag(NH$_3$)$_2$]NO$_3$, and the sulphate complex, [Ag(NH$_3$)$_2$]$_2$SO$_4$, have been previously studied by X-ray crystallography [12,13], and the crystal structure of [Ag(NH$_3$)$_2$]$_2$SeO$_4$ was recently reported [14]. The structural data and selected bond distances and angles of the three silver(I) ammine complex are presented in Table 6-2.

Table 6-2 Summary of selected bond distances (Å) and angles (deg) for [Ag(NH$_3$)$_2$]NO$_3$, [Ag(NH$_3$)$_2$]$_2$SO$_4$, and [Ag(NH$_3$)$_2$]$_2$SeO$_4$

	[Ag(NH$_3$)$_2$]NO$_3$ [a]		[Ag(NH$_3$)$_2$]$_2$SO$_4$ [b]	[Ag(NH$_3$)$_2$]$_2$SeO$_4$ [c]
Crystal system	orthorhombic		tetragonal	tetragonal
Space group	*Pnnm*		$P\bar{4}2_1c$	$P\bar{4}2_1c$
Ag(1)-N	2.155(16)	Ag-N	2.110(3)	2.112(2)
Ag(2)-N	2.172(22)			
Ag(2)-O(1)	2.915(23)	Ag-O	3.259(3)	3.249(3)
Ag(1)-O	3.791(11)			
N-Ag-N	180.00(81)	N-Ag-N	174.31(11)	172.84(14)
N-Ag-Ag-N	54.72(64)	N-Ag-Ag-N	38.68(11)	38.98(10)
Ag-Ag [d]	3.143(1)	Ag-Ag	3.20	3.262(0)

[a] Ref [12]. [b] Ref [13]. [c] Ref [14]. [d] The van der Waals radius of Ag is 1.72 Å.

The structure of diammine silver(I) nitrate is shown in Figure 6-1. It consists of linear $[Ag(NH_3)_2]^+$-units, which are aligned in a columnar arrangement along the crystallographic c-axis. The units are held together with Ag-Ag separations of 3.143 Å. The $[Ag(NH_3)_2]^+$-columns are surrounded by NO_3^--ions, which lie parallel to the (011) plane. The angle of torsion of the stacked $[Ag(NH_3)_2]^+$-ions, (N-Ag-Ag-N), is 54.7°. The Ag(1)-atoms occupy the centre of prisms, which are the result of the alignment of the nitrate-anions, as shown in Figure 6-2. The Ag(2)-atoms occupy the centre of four nitrate anions, which form parallelograms. Additionally, Ag(2) is coordinated by two oxygen atoms, where the distance $d(Ag(2)-O(1)) = 2.915$ Å. The Ag(2) environment is distorted square planar. However, the N-Ag-N angle of the diammine silver(I)-cation is 180°.
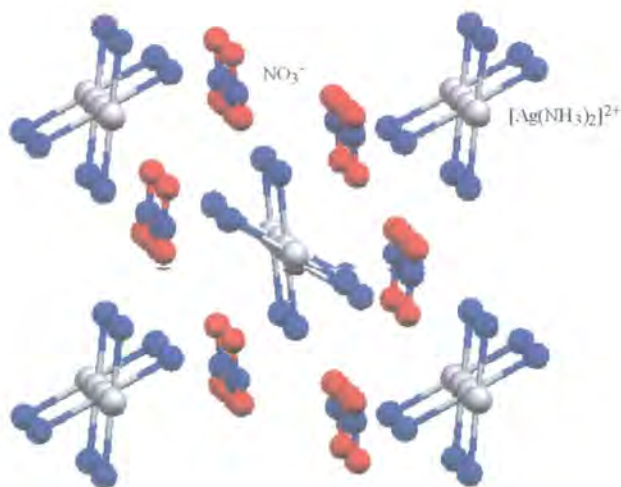
Figure 6-1 Perspective view of the structure of $[Ag(NH_3)_2]NO_3$ along the c-axis. The coordinates of the hydrogen atoms are unknown.
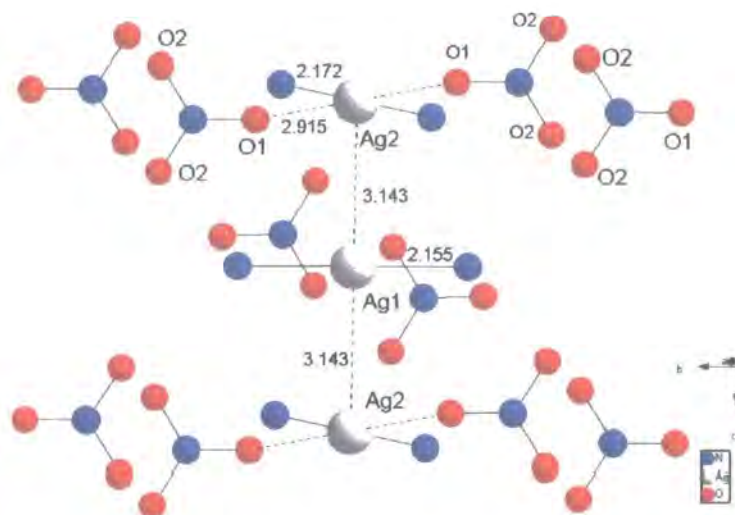
Figure 6-2 The immediate NO_3^--environment of one $[Ag(NH_3)_2]^+$-column in $[Ag(NH_3)_2]NO_3$. The coordinates of the hydrogen atoms are unknown.

The structure of diammine silver(I)-sulfate is shown in Figure 6-3, and is similar to that of diammine silver(I)-nitrate. The structure is built up of metal-over-metal stacks of $[Ag(NH_3)_2]^+$-cations along the crystallographic c-axis. The $[Ag(NH_3)_2]^+$-units are held together with a Ag-Ag separation of 3.200 Å by slightly bent hydrogen bonds N-H···O as can be seen in Figure 6-4. The torsion angle N-Ag-Ag-N of 38.68° is smaller than in the case of $[Ag(NH_3)_2]NO_3$. The N-Ag-N angle of the diammine silver(I)-cation is 174.31°. This departure from linearity is due to the coordination of silver(I) by two oxygen atoms of the sulfate anions. However, the distance d(Ag-O) = 3.259 Å is significantly longer than d(Ag-N) = 2.110 Å.
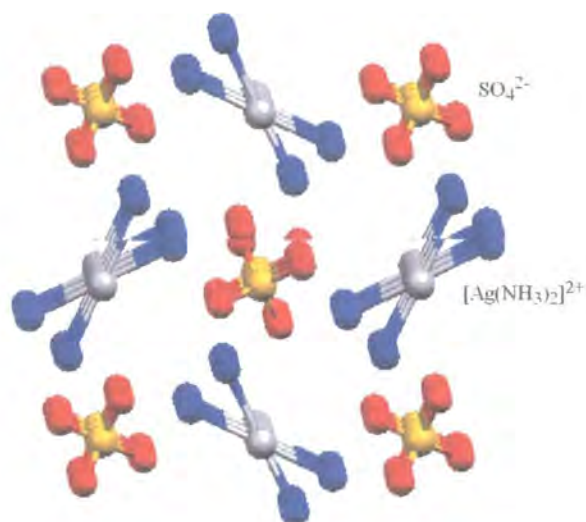
Figure 6-3 Perspective view of the structure of [Ag(NH₃)₂]₂SO₄ along the *c*-axis. The hydrogen atoms have been omitted for clarity.
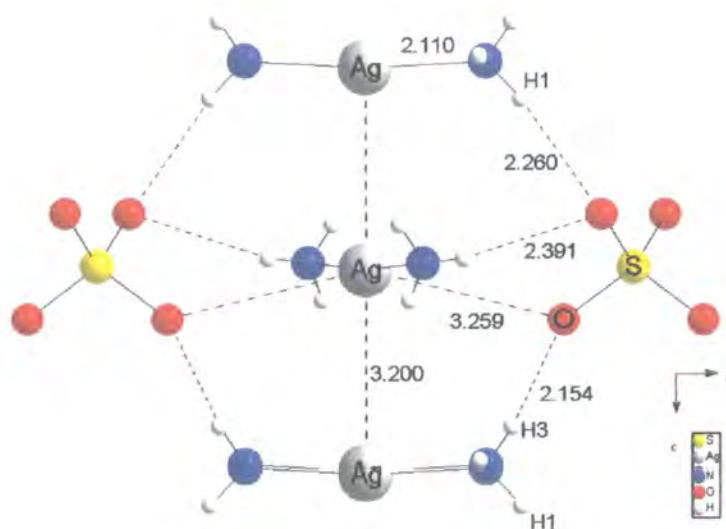
Figure 6-4 The immediate NO₃⁻-environment of one [Ag(NH₃)₂]⁺-column in [Ag(NH₃)₂]₂SO₄

The structure of diammine silver(I)-selenate shows that the selenate complex is isomorphous with the corresponding sulphate complex. The N-Ag-N angle for the diammine silver(I)-cation is non-linear, 172.84°.

Diammine silver(I)-nitrate, [Ag(NH₃)₂]NO₃

Silver-109 CP/MAS spectra with proton decoupling of $[Ag(NH_3)_2]NO_3$ are shown in Figure 6-5. The spectrum in Figure 6-5 (a), obtained at 13.97 MHz with spinning at 3 kHz, shows a large number of spinning sidebands. This suggests a large shielding anisotropy for the silver nuclei, which is characteristic of heavy atoms. The centrebands are expanded in Figure 6-5 (b), which consist of two symmetrical 1:2:3:2:1 quintets. This implies that the asymmetric unit contains two silver atoms in the nitrate. It is clearly consistent with the crystal structure data.

The quintet pattern arises from the coupling between a single silver nucleus ($I = 1/2$) and two equivalent ^{14}N nuclei ($I = 1$). Thus, the splitting of the quintets with a spacing of about 49 Hz can be attributed to the presence of indirect $^1J(^{109}Ag^{14}N)$ spin-spin coupling. The chemical shifts and coupling constants are summarised in Table 6-3.

Coupling constants have been confirmed by acquiring the spectrum at a higher field strength (11.7 T) since the J-coupling (when expressed in Hz) is independent of the magnetic field. The ^{109}Ag CPMAS spectrum (centreband expansion) obtained at 23.27 MHz is shown in Figure 6-5 (c). The quintets from the two fields give clear evidence that no second-order effects arising from dipolar coupling between ^{109}Ag and the quadrupolar ^{14}N nuclei.
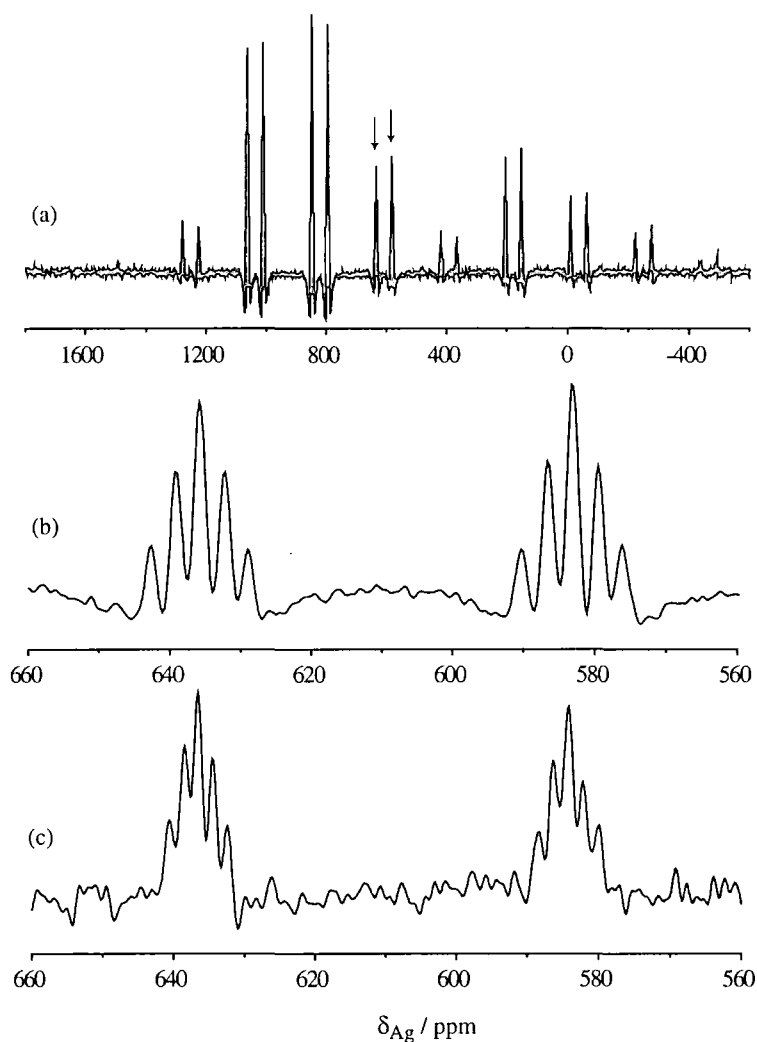
Figure 6-5 Silver-109 CPMAS NMR spectra of [Ag(NH₃)₂]NO₃, obtained at (a), (b) 13.97 MHz with spinning at 3 kHz and (c) 23.27 MHz with spinning at 6 kHz. The centrebands are indicated by arrows. Acquisition parameters were: contact time 8 ms, recycle delay 2 s, and number of transients: (a), (b) 27584, (c) 25372.

Only the centreband is shown (see Figure 6-5 (c)) because the sidebands cannot be adjusted to the same phase in the ^{109}Ag spectrum. One possible reason of this problem may relate to the spin-lock field strength, which is probably not sufficient to efficiently lock the silver magnetisations along B_1-axis during the mixing time (CSA ~ 36 kHz whereas the spin-locked field strength is *ca.* 17 kHz). This problem, however, has no effect on the magnitude of the splittings, and the values obtained from the sidebands are consistent with that of the centreband.

The dips around the peaks in the ^{109}Ag spectrum obtained at 13.97 MHz, as shown in Figure 6-5 (a), probably arise from problems with recovery of the receiver circuitry after the excitation (the RF powers used are *ca.* 1 kW). Note that the problems of baseline distortion are not due to the dead time since a long delay time *ca.*100 μs was used for the selenate and sulphate complexes to avoid these problems; this however still did not produce a distortion-free spectrum. A spin-echo with a standard CP sequence was employed for the nitrate complex (the rotor period is *ca.* 250 μs and the delay times, τ, before and after the echo pulse were set to this). However, the distortions were still observed.

A nitrogen-15 spectrum for [Ag(NH$_3$)$_2$]NO$_3$ was easily acquired using CP/MAS and proton decoupling, as shown in Figure 6-6 (a). Two doublet signals at -391.5 and -394.1 ppm for [Ag(NH$_3$)$_2$]$^{2+}$ (the expanded peaks are also shown) and one peak at -4.2 ppm for NO$_3^-$ are observed. These are in excellent agreement with the crystal structure, which consists of three nitrogen atoms in the asymmetric unit.

The splittings in the ^{15}N spectrum can be assigned to ^1J coupling between ^{109}Ag and ^{15}N. However, it was not clear whether the correct values are from the spacing between lines no. 1 and 2 or lines no. 1 and 3 (see Figure 6-6 (a)). Therefore, the values were confirmed from the nitrogen-15 spectrum at 11.7 T, as shown in Figure 6-6 (b). Clearly, the two amine groups give $\left| {^1J(^{107,109}\text{Ag}^{15}\text{N})} \right|$ of 62 and 65 Hz. These values were obtained from the spectrum at the lower field (7.05 T) and are from the separations between lines no. 1 and 2, and lines no. 3 and 4 (see the top right in Figure 6-6 (a)).

It should be noted that using the natural abundances and magnetogyric ratios of the ^{107}Ag and ^{109}Ag [15,16], it can be shown that the average coupling constant $^1J(^{109}Ag^{15}N)$ = $1.072 \times \, ^1J(^{107,109}Ag^{15}N)$, so that $| \, ^1J(^{109}Ag^{15}N) \, |$ = 66 and 70 Hz for the nitrate. Therefore, the observed ratio of $J(^{109}Ag^{15}N)/J(^{109}Ag^{14}N)$, 68/49 is 1.39, consistent with γ_{15}/γ_{14}, 1.40. The ^{15}N chemical shifts and the coupling constants are given in Table 6-3.
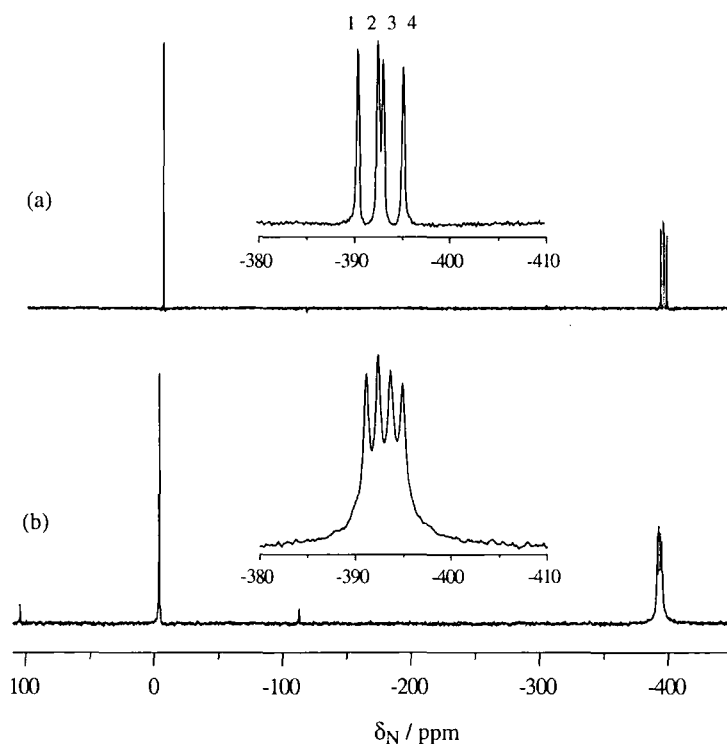
Figure 6-6 Nitrogen-15 CPMAS NMR spectra of $[Ag(NH_3)_2]NO_3$, obtained at (a) 30.40 MHz with spinning at 3.5 kHz and (b) 50.64 MHz with spinning at 6 kHz. Acquisition parameters were: contact time 20 ms, recycle delay 2 s, and number of transients: (a) 30000, (b) 8824.

From the above results (both the crystal structure and NMR studies), it is clear that there are two half cations of $[Ag(NH_3)_2]$ in the asymmetric unit.

Table 6-3 Chemical shifts and coupling constants for $[Ag(NH_3)_2]^+$ ions from solid-state ^{109}Ag and ^{15}N NMR spectra.

Compound	Nucleus	δ_{iso} / ppm	$|{}^1J({}^{109}Ag^{14,\,15}N)|$ / Hz ^{a}	
			at 300 MHz	at 500 MHz
$[Ag(NH_3)_2]NO_3$	^{109}Ag	636.5	48.5	48.2
	^{109}Ag	583.8	49.4	49.4
	$^{15}N^b$	-391.5	66.8^d	67.3^d
	$^{15}N^b$	-394.1	69.6^d	70.0^d
	$^{15}N^c$	-4.2		
$[Ag(NH_3)_2]_2SO_4$	^{109}Ag	606.9	43.4	46.8
	^{15}N	-389.1	65.7^d	
$[Ag(NH_3)_2]_2SeO_4$	^{109}Ag	596.5	49.0	46.8
	^{15}N	-388.1	64.7^d	
	^{77}Se	1044.4		

^{a} ± 0.5 Hz. ^{b} Values for the nitrogen peaks for $[Ag(NH_3)_2]^{2+}$ cations. ^{c} Value for the nitrate peak.

^{d} Values are obtained from the observed $|{}^1J({}^{107,109}Ag^{15}N)|$ by using ${}^1J({}^{109}Ag^{15}N) = 1.072 \times {}^1J({}^{107,109}Ag^{15}N)$, which can be calculated from the natural abundances and gyromagnetic ratios of ^{107}Ag and ^{109}Ag.

Diammine silver(I)-sulphate, $[Ag(NH_3)_2]_2SO_4$

Figure 6-7 shows the ^{109}Ag spectra for $[Ag(NH_3)_2]_2SO_4$. A single quintet with a separation of *ca.* 43 Hz was found in the spectrum obtained at 13.97 MHz, as shown in Figure 6-7 (b). This information suggests that there is only one silver atom in the crystallographic asymmetric unit, which also correlates well with the finding from X-ray crystallography [13].

The apparently unsymmetrical intensity distribution in the quintet was puzzling. This anomalous result was investigated by acquiring the spectrum at a different magnetic field (11.7 T). The silver-109 was successfully obtained at 23.27 MHz, as shown in Figure 6-7 (c) (only the centreband is displayed due to the difficulty in phasing that is explained

above). Obviously, the relative intensities of the component are a symmetrical 1:2:3:2:1 quintet, which produces the expected ^{109}Ag-^{14}N splitting of 47 Hz. Therefore, it can be concluded that the odd intensity distribution observed at the lower field (7.05 T) is an artifact caused by the difficulty of implementing CP for ^{109}Ag, i.e. large B_{1Ag}. (see also the results for the selenate, below)
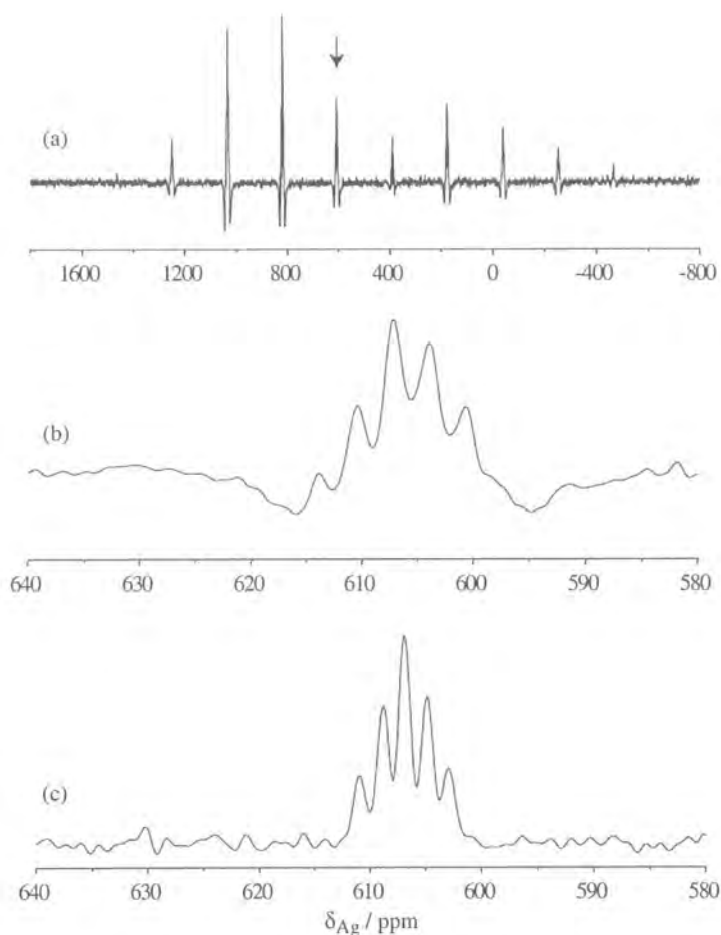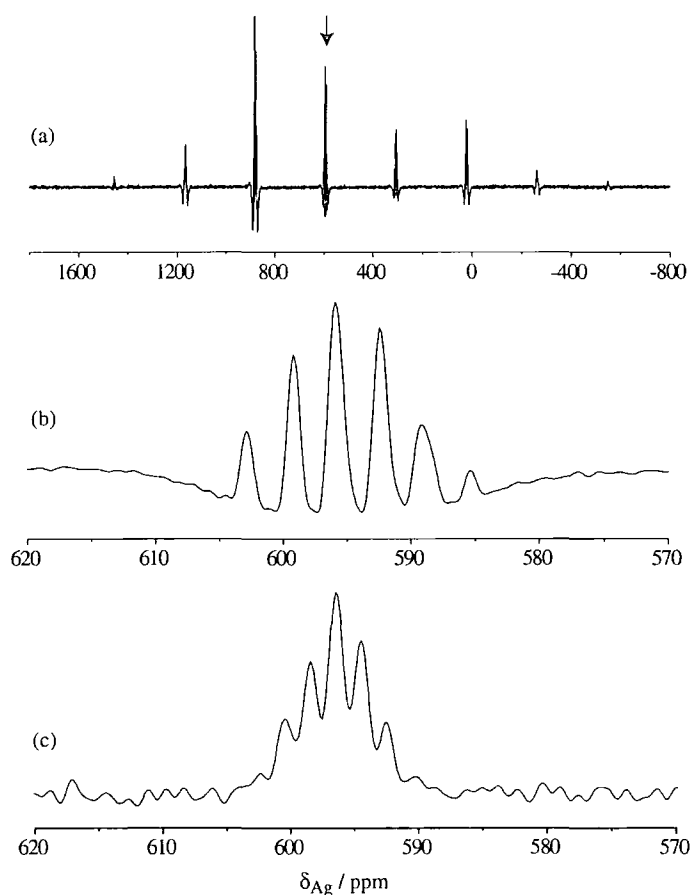

Figure 6-7 Silver-109 CPMAS NMR spectra of [Ag(NH$_3$)$_2$]$_2$SO$_4$, obtained at (a), (b) 13.97 MHz with spinning at 3 kHz and (c) 23.27 MHz with spinning at 6 kHz. Acquisition parameters were: contact time 8 ms, recycle delay 2 s, and number of transients: (a), (b) 4000, (c) 2640.

Figure 6-8 shows the proton-decoupled ^{15}N spectrum with CPMAS experiment, obtained at 30.40 MHz. There is only a single doublet at -389.1 ppm, with a separation of 61 Hz. This reveals that only one nitrogen atom exists in the asymmetric unit, in agreement with the crystal structure.
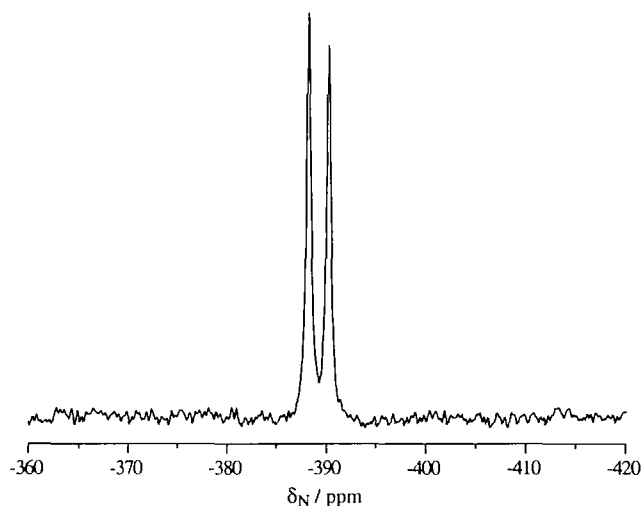
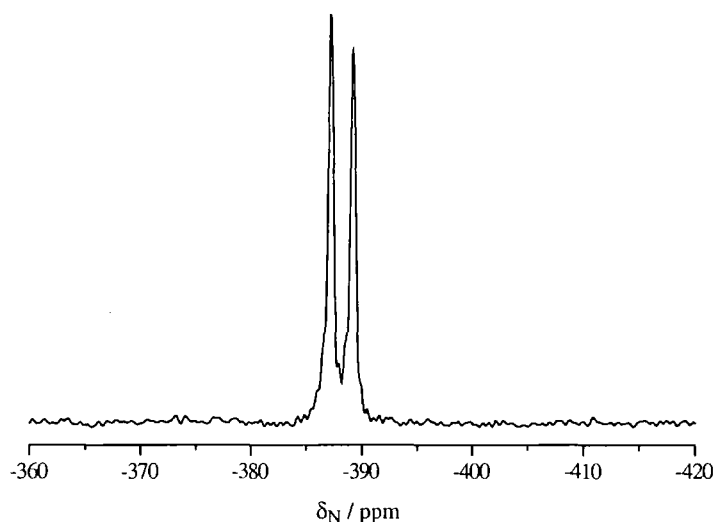**Figure 6-8** Nitrogen-15 CPMAS NMR spectra of [Ag(NH$_3$)$_2$]$_2$SO$_4$, obtained at 30.40 MHz with spinning at 3.5 kHz. Acquisition parameters were: contact time 20 ms, recycle delay 2 s, and number of transients 3296.

As previously shown, the NMR results are fully consistent with the described structure, and it can be concluded that there is a half molecule of [Ag(NH$_3$)$_2$]$^+$ present in the asymmetric unit.

Diammine silver(I)-selenate, [Ag(NH$_3$)$_2$]$_2$SeO$_4$

Silver-109 CPMAS spectra of the selenate complex [Ag(NH$_3$)$_2$]$_2$SeO$_4$ are displayed in Figure 6-9. The centreband obtained at 13.97 MHz, as shown in Figure 6-9 (a), appears to consist of six lines rather than the quintet found for the nitrate complex [Ag(NH$_3$)$_2$]NO$_3$. The separation of each peak is 49 Hz. The appearance of the centreband is similar to its counterpart in the sulphate complex [Ag(NH$_3$)$_2$]$_2$SO$_4$. Thus, it is of interest to investigate this multiplet pattern at a different field.

Figure 6-9 Silver-109 CPMAS NMR spectra of [Ag(NH₃)₂]₂SeO₄, obtained at (a), (b) 13.97 MHz with spinning at 4 kHz and (c) 23.27 MHz with spinning at 6 kHz. Acquisition parameters were: contact time 8 ms, recycle delay 2 s, and number of transients: (a), (b) 30048, (c) 2048.

The [109]Ag CPMAS spectrum at 23.27 MHz was obtained to examine the appearance of the centreband. The result is illustrated in Figure 6-9 (c). It shows a clear 1:2:3:2:1 quintet as expected with a splitting of 47 Hz (unsurprisingly, the coupling arises from the two equivalent ^{14}N atoms). Therefore, the result obtained at the higher field strongly suggests that unsymmetrical sextet, as shown in Figure 6-9 (b), is (see the explanation for the odd intensity distribution in the sulphate complex) wrong.

Two lines were observed in the nitrogen-15 CPMAS spectrum, as shown in Figure 6-10. The separation is 60 Hz, which is very close to the 61 Hz found for the sulphate complex, and the ratio of $J(^{109}\text{Ag}^{15}\text{N})/J(^{109}\text{Ag}^{14}\text{N})$, 64/48 is 1.33.

The NMR results suggest that there is one half of a $[\text{Ag(NH}_3)_2]$-cation in the asymmetric unit.

Figure 6-10 Nitrogen-15 CPMAS NMR spectra of $[\text{Ag(NH}_3)_2]_2\text{SeO}_4$, obtained at 30.40 MHz with spinning at 3.5 kHz. Acquisition parameters were: contact time 20 ms, recycle delay 2 s, and number of transients 6592.

Furthermore, a ^{77}Se signal from the selenate anion was detected at 57.27 MHz, as shown in Figure 6-11. A single peak at 1044.4 ppm is observed, in agreement with the presence of one anion in the asymmetric unit of the structure derived from X-ray diffraction measurements.

The chemical shifts and coupling constants for the selenate complex are summarised in Table 6-3.
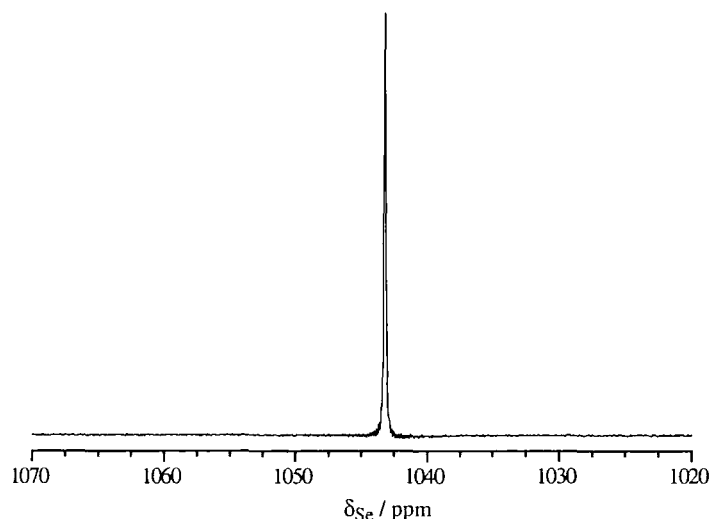
Figure 6-11 Selenium-77 CPMAS NMR spectra of $[Ag(NH_3)_2]_2SeO_4$, obtained at 57.27 MHz with spinning at 3.5 kHz. Acquisition parameters were: contact time 10 ms, recycle delay 2 s, and number of transients 64.

Spinning sideband analysis

The spinning sideband intensities in the ^{109}Ag CPMAS spectra of $[Ag(NH_3)_2]NO_3$, $[Ag(NH_3)_2]_2SO_4$ and $[Ag(NH_3)_2]_2SeO_4$ were analysed. An iterative program for spinning sideband analysis (SSB97) [17], written in-house, was used to obtain values for the anisotropy and asymmetry via the principal shielding tensor components of those compounds. Absolute value spectra were employed to solve the problem of baseline dips around the peaks, so all signals are always positive. After applying the absolute-value mode, the peak height of the highest peak (in general at the middle) of each sideband was used instead of the peak integral. The fitting procedure used the peak height of 7 to 9 sidebands plus the centreband, and was carried out at spinning rates of: 3 kHz for $[Ag(NH_3)_2]NO_3$ and $[Ag(NH_3)_2]SO_4$, 4 kHz for $[Ag(NH_3)_2]SeO_4$. The ^{109}Ag shielding tensor data are given in Table 6-4.

Table 6-4 Tensor information from spinning sideband analysis, with observation of ^{109}Ag at 23.27 MHz.^{a}

Compound	$\sigma_{11} - \sigma_{ref}$ /ppm	$\sigma_{22} - \sigma_{ref}$ /ppm	$\sigma_{33} - \sigma_{ref}$ /ppm	ζ /ppm	η
$[Ag(NH_3)_2]NO_3$					
at 636.5 ppm	-1195 ± 49	-1118 ± 48	405 ± 12	1041 ± 12	0.07 ± 0.09
at 583.8 ppm	-1111 ± 53	-1111 ± 53	472 ± 9	1056 ± 9	0.00 ± 0.10
$[Ag(NH_3)_2]SO_4$	-1161 ± 10	-954 ± 9	327 ± 7	923 ± 7	0.22 ± 0.02
$[Ag(NH_3)_2]SeO_4$	-1285 ± 14	-961 ± 10	424 ± 17	1032 ± 17	0.31 ± 0.01

^{a} Errors in the shielding tensors are statistical and were calculated by a published method [18] .

The shielding anisotropy values, ζ, are all positive, and lie in the range of 923-1056 ppm. Note that accuracy was limited by the relatively high noise levels. The sign is the same as that observed for ^{199}Hg shielding anisotropies for linear two-coordinate mercury(II) complexes, but the magnitudes of this parameter for silver are considerably lower than those observed in the mercury compounds [19]. Both of these observations are consistent with the view that the shielding anisotropy is determined mainly by the local paramagnetic contributions to the shielding (see below). Following Ref. [19] the expression for the local paramagnetic contribution, σ_P, considering np electrons only, is:

$$\sigma_P = -\mu_0 e^2 h^2 \left\langle r^{-3} \right\rangle_{np} / 4\pi m^2 \Delta E \tag{0.1}$$

where μ_0 is the permeability constant, e is the electronic charge, m is the electron rest mass, $\left\langle r^{-3} \right\rangle_{np}$ is the expectation value of r^{-3} for the valence np electron and ΔE is an average excitation energy.

σ_P generally includes d-orbitals when heavier nuclei are considered, but the d-orbital involvement in the bonding will be small for Hg(II) and Ag(I) ($5d^{10}$ and $4d^{10}$ respectively).

Thus, a reduction in shielding anisotropies from the Hg(II) to the Ag(I) case is expected due to the reduction in $<r^{-3}>_{np}$ for the metal np orbitals (see Equation 6.1) involved in the metal-ligand bonding ($6p$ in Hg(II) and $5p$ in Ag(I)) [19].

As shown in Table 6-4, the analyses of the spinning sideband manifolds imply that the silver atom in [Ag(NH$_3$)$_2$]NO$_3$ has nearly axial symmetry. On the other hand, the silver atoms in both [Ag(NH$_3$)$_2$]$_2$SO$_4$ and [Ag(NH$_3$)$_2$]$_2$SeO$_4$ are clearly in non-axially symmetric environments. Note that the spectra are not sensitive to low asymmetry values, so it is difficult to distinguish between axially symmetric ($\eta = 0$) and nearly-axially symmetric ($\eta < 0.2$) systems.

From the above analysis, the asymmetry parameter may imply that the N-Ag-N angles in [Ag(NH$_3$)$_2$]-cation for [Ag(NH$_3$)$_2$]NO$_3$ complexes are linear whereas for the sulphate and selenate this angle is non-linear. These results are consistent with the angles obtained from X-ray diffraction studies (180°, 174.31°, 172.84° for the nitrate, sulphate and selenate respectively).

6.4.2   Various Silver Complexes with a Nitrate Counter Ion

This section involves the study of five silver(I)-nitrate complexes: dipyridine silver(I)-nitrate, [Ag(py)$_2$]NO$_3$, dilutidine silver(I)-nitrate, [Ag(lut)$_2$]NO$_3$, dicollidine silver(I)-nitrate, [Ag(coll)$_2$]NO$_3$, di(2-picoline) silver(I)-nitrate, [Ag(2-pic)$_2$]NO$_3$, and diquinoline silver(I)-nitrate, [Ag(quin)$_2$]NO$_3$. The aims of the solid-state NMR experiments is to gain structural information about the compounds, especially concerning the crystallographic asymmetric unit to compare with the known crystal structures, and to report the chemical-shift data.

In general, an isolated molecule of $[Ag(X)_2]NO_3$, where X = py, lut, coll, 2-pic, quin, contains a $[Ag(X)_2]^+$ cation and a NO_3^- anion. Schematic representations of the substituted X structures in silver(I)-cations for the five compounds are shown below:
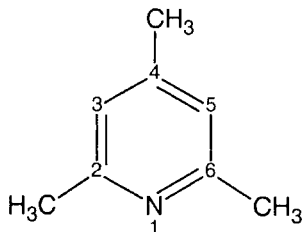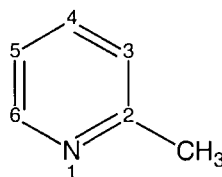
py = pyridine
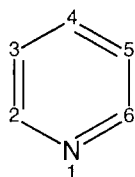
lutidine = 2,6-dimethylpyridine
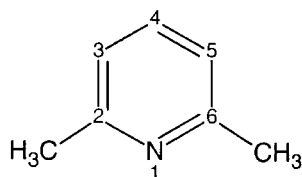
collidine = 2,4,6-trimethylpyridine

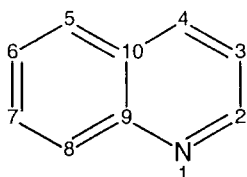2-picoline = 2-methylpyridine

quinoline

Figure 6-12 Schematic structures of the ligands in the silver(I)-cations.

The crystal structure of $[Ag(lut)_2]NO_3$ was previously determined by X-ray crystallography [20], and the structures of $[Ag(py)_2]NO_3$, $[Ag(coll)_2]NO_3$, $[Ag(quin)_2]NO_3$ and $[Ag(2\text{-pic})_2]NO_3$ were recently studied [21], but they have not been reported in the literature yet. A common structural characteristic is silver(I) two coordinated to N atoms (N-Ag-N) of aromatic ligands. For the purpose of comparison, the structural data and selected bond distances and angles of these complexes are summarised in Table 6-5.

Table 6-5 Summary of selected bond distances (Å) and angles (deg) for [Ag(x)$_2$]NO$_3$, where X = py, lut, coll, 2-pic, quin.

	[Ag(py)$_2$]NO$_3$	[Ag(lut)$_2$]NO$_3$	[Ag(coll)$_2$]NO$_3$	[Ag(2-pic)$_2$]NO$_3$	[Ag(quin)$_2$]NO$_3$
Crystal system	monoclinic	monoclinic	monoclinic	triclinic	monoclinic
Space group	$C2/c$	$P2_1/n$	$P2_1/n$	$P\overline{1}$	$P\overline{1}$
Ag(1)-N(1)	2.180(3)	2.182(6)	2.160(4)	2.201(6)	2.23(3)
Ag(1)-N(2)		2.192(6)	2.162(4)	2.207(6)	2.19(3)
Ag(2)-N(11)					2.26(3)
Ag(2)-N(21)					2.18(4)
Ag(1)-O(1)	2.858(3)	2.715(8)	2.691(6)	2.54(1)	2.51(4)
Ag(1)-O(2)	2.9140(7)	2.663(7)	2.731(6)	2.547(8)	2.84(3)
Ag(2)-O(1)					2.64(5)
Ag(2)-O(3)					2.90(4)
Ag(2)-O(4)					2.70(4)
N(1)-Ag(1)-N(2)	172.8(1)	169.3(2)	166.9(2)	140.4(3)	143(1)
N(11)-Ag(2)-N(21)					144(1)

Carbon-13 and Nitrogen-15 CPMAS spectra were acquired for all compounds. Silver-109 CPMAS spectra were obtained at 23.27 MHz with high-power proton decoupling for [Ag(lut)$_2$]NO$_3$ and [Ag(2-pic)$_2$]NO$_3$. The assignment of carbon signals in this study was made by reference of 'carbon-13 NMR spectroscopy' by Stothers [22] and 'spectroscopic method in organic chemistry' by Williams and Fleming [23].

The ^{13}C and ^{15}N chemical shifts of silver(I) complexes for this section are given in Table 6-6 and 6-7.

Table 6-6 Carbon-13 chemical shifts of the silver(I)-nitrate complexes

Compound	δ_{iso}/ppm			
	C-2,6	C-3,5	C-4	CH$_3$
[Ag(py)$_2$]NO$_3$	151.4	125.4	143.1	-
[Ag(lut)$_2$]NO$_3$	159.5^a	123.2^a	141.0^a	27.4, 26.5, 25.5
	157.5^a	121.7^a	139.9^a	
[Ag(coll)$_2$]NO$_3$	157.7	123.2	152.4	27.8, 26.7, 24.9,
		122.1	150.3	21.7, 20.7

	C-2	C-3	C-4	C-5	C-6	CH$_3$
[Ag(2-pic)$_2$]NO$_3$	157.5	125.6	139.1	122.5	149.6	25.2
	159.1	123.2			151.1	27.0

	C-2	C-3	C-4	C-5	C-6	C-7	C-8	C-9	C-10
[Ag(quin)$_2$]NO$_3$^{b}	154.1	-	-	-	-	-	-	145.6	-

^{a} All values are obtained by deconvolution.

^{b} Most of peak positions cannot be derived (see the texts).

Table 6-7 Nitrogen-15 chemical shift of silver(I)-nitrate complexes.

Compound	δ_{iso}/ppm		$\lvert {}^1J({}^{109}Ag{}^{15}N)\rvert$ /Hz [b]
	${}^{15}N^a$ in silver(I)-cations	NO_3	
[Ag(py)₂]NO₃	-117.0	-1.2	81.8
[Ag(lut)₂]NO₃	-109.0, -112.4	-2.2	81.5
[Ag(coll)₂]NO₃	-118.4, -122.3	-4.2	84.2, 77.7
[Ag(2pic)₂]NO₃	-105.4, -107.1	-3.0	59.0
[Ag(quin)₂]NO₃ [c]	-112.6, -115.2	-2.8	-

[a] The ${}^{15}N$ chemical shifts in the isolated pyridine-derivative ligands obtained from solution-state NMR (with respect to nitromethane) are in a range of (-62.2) – (-63.5) ppm [24]. (see the texts for discussion of the chemical shift discrepancies)

[b] See footnote in Table 6-3.

[c] The peak position in silver(I)-cations are not clear from the obtained spectra.

Dipyridine silver(I)-nitrate, [Ag(py)₂]NO₃

The structure was determined by X-ray crystallography [21] including the monohydrate, in which water has no apparent structural role. The asymmetric unit consists of one molecule of pyridine ligand, silver, nitrate and water. The [Ag(py)₂]NO₃ is a flat one-dimensional polymer and crystal packing is dominated by overlapping symmetry-related pyridine ligands. The Ag atom lies on a crystallographic 2-axis, which is coordinated by two nitrogen atoms from a pair of pyridine ligands. The N-Ag-N angle of [Ag(py)₂]-cation is 172.8(2)°. Equatorial to the N-Ag-N axis, the Ag is approached from either side by a pair of symmetry-related chelating oxygen atoms from the nitrate group. The nitrate group has almost trigonal symmetry (in term of bond angles and distances: 1.235(4), 1.247(7) Å; 119.9(3) °, 120.3(5)° (×2)), while Ag-O-Ag (at the bridging oxygen) is nearly linear (169.4(2)°).

High-resolution solid-state carbon-13 spectra are characterised by individual isotropic chemical shifts, each of which may be assigned to a chemically different carbon atom in the unit cell. The carbon-13 spectrum obtained under conditions of cross-polarisation from protons is illustrated in Figure 6-13. Three peaks and their separate spinning sideband manifolds are clearly observed. The chemical shifts are at 151.4, 125.4 and 143.1 ppm for C-2,6, C-3,5 and C-4 respectively.
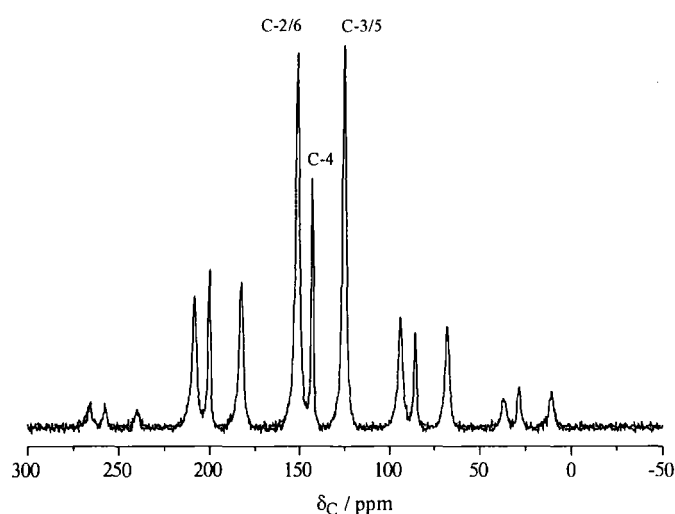

Figure 6-13 Carbon-13 CPMAS NMR spectra of [Ag(py)$_2$]NO$_3$, obtained at 75.43 MHz with spinning at 4.4 kHz. Acquisition parameters were: contact time 1 ms, recycle delay 5 s, and number of transients 800.

Structural information may be obtained by considering the number of resonances for C-4 and C-3,5. A single peak observed for C-4 suggests a half-molecule or one whole molecule of pyridine in the asymmetric unit. If there is half a molecule in the asymmetric unit, it must give a single line for C-3,5. On the other hand, if there is one whole molecule in the asymmetric unit, it must give two lines for C-3,5. It is not feasible to distinguish these cases from the lines observed since the signal for C-3,5 is rather broad (see the discussion below). This suggests that there is one whole molecule of pyridine ligand in the asymmetric unit, in agreement with the crystal structure described above.
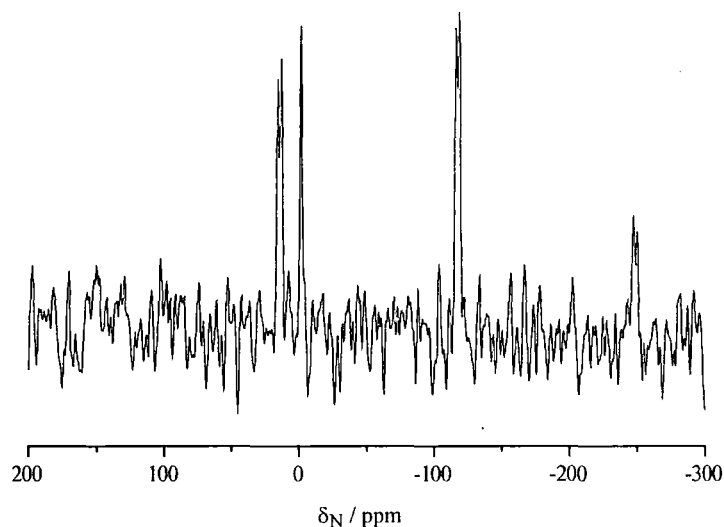
Figure 6-14 Nitrogen-15 CPMAS NMR spectrum of [Ag(py)₂]NO₃, obtained at 30.40 MHz with spinning at 4 kHz. Acquisition parameters were: contact time 2 ms, recycle delay 20 s, and number of transients 3588.

Figure 6-14 shows the proton-decoupled ^{15}N spectrum at 30.40 MHz, obtained with cross-polarisation. The ^{15}N chemical shifts, however, are not difficult to obtain even with the poor signal-to-noise ratio. One peak for the NO₃-anion is found at -1.2 ppm. Two equal intensity centreband peaks are observed at -115.8 and -118.2 ppm for the [Ag(py)₂]-cation. The splitting is due to J coupling between ^{15}N and Ag nuclei with a $| ^1J(^{107,\,109}\text{Ag}^{15}\text{N}) |$ of 76.3 Hz.

Dilutidine silver(I)-nitrate, [Ag(lut)₂]NO₃

The crystal structure of this compound is known [20] and the structural information is given in Table 6-5. A silver atom is coordinated pseudo-linearly with a pair of lutidine ligands, and the nitrate behaves as a weakly chelating ligand, where Ag...O are 2.715(8) and 2.663(7) Å. The structure is illustrated in Figure 6-15. One formula unit, in which the two lutidine ligands are crystallographically independent, is the asymmetric unit of the structure.
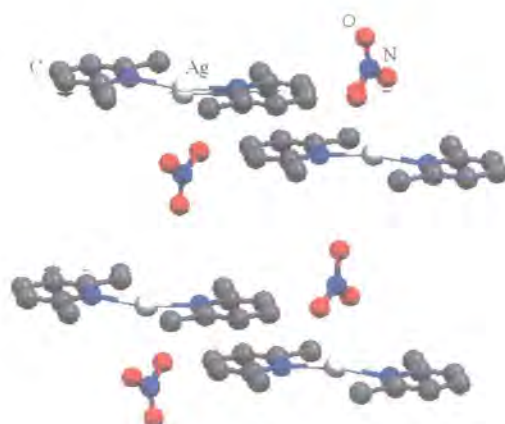
Figure 6-15 Crystal structure of dilutidine silver(I)-nitrate. The hydrogen atoms have been omitted for clarity.

Carbon-13 spectra of [Ag(lut)₂]NO₃ are shown in Figure 6-16. Figure 6-16 (a) consists of several sets of spinning sidebands. However, the spinning sidebands do not confuse the interpretation of this spectrum. The sidebands can be removed by faster spinning, but the cross-polarisation experiment becomes inefficient at higher spin rates [25-27]. The spinning sidebands may be suppressed using the Total Suppression of Spinning Sideband (TOSS) sequence. The CPMAS / TOSS spectrum is shown in Figure 6-16 (b). Non-quaternary suppression (NQS) (also known as "dipolar dephasing") was used to assist in the assignment of the signals. Clearly, we can see from Figure 6-16 the differences between the quaternary carbons (C-2,6) and the methyl group signals from the other main peaks. The values of the chemical shifts are given in Table 6-6.
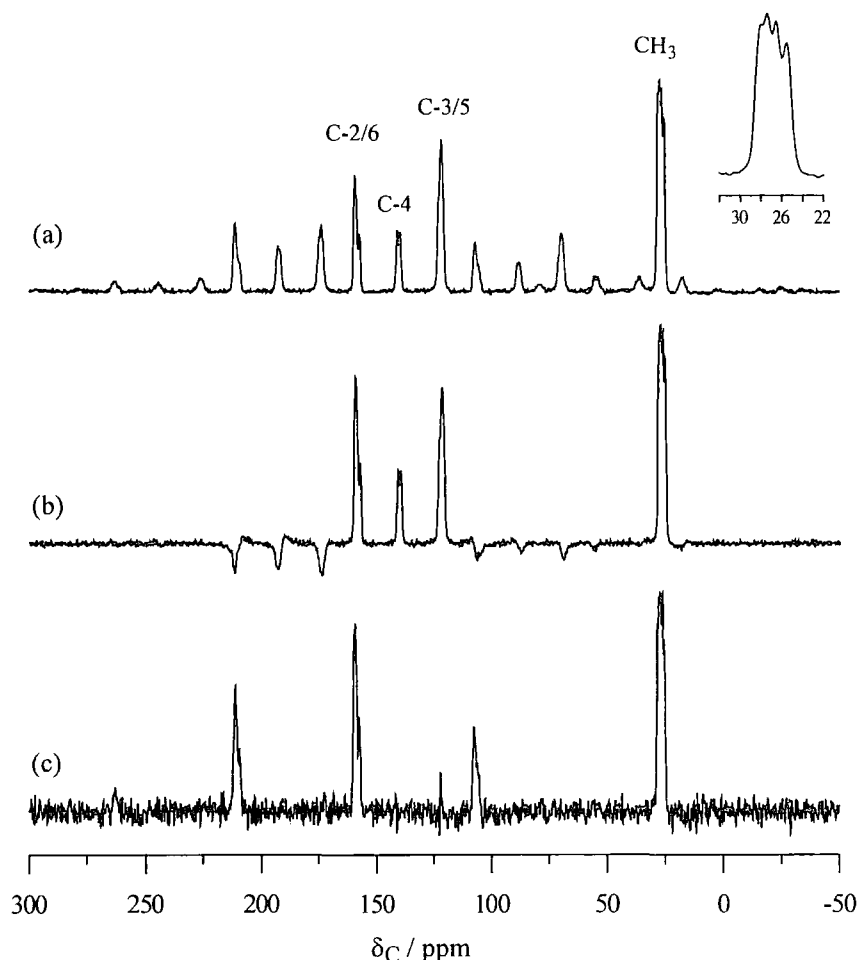
Figure 6-16 (a) Carbon-13 CPMAS NMR spectrum with (b) TOSS and (c) NQS experiments for [Ag(lut)$_2$]NO$_3$, obtained at 75.43 MHz with spinning at 4 kHz. Acquisition parameters were: contact time 1 ms, recycle delay 5 s, and number of transients: (a) 300 (b) 220 (c) 160.

The doublet line for C-4 shows that the asymmetric unit contains two half-molecules or two whole molecules of lutidine ligand. The C-3,5 peak for this compound is again very broad and has no observed splitting: it must give two lines if there are two half-molecules, or four lines if there are two whole molecules in the asymmetric unit. The structure can be confirmed from the number of the ^{13}C resonances for the methyl groups. There are at least three CH$_3$ peaks (top right of Figure 6-16). Implying that the

asymmetric unit probably has two whole molecules of lutidine ligand, in agreement with the X-ray measurements.

The nitrogen-15 CPMAS spectrum was studied at two magnetic fields (7.05 and 11.7 T). Figure 6-17 (a) shows the ^{15}N spectrum obtained at the lower magnetic field. A very sharp peak at –2.2 ppm with linewidth of 30 Hz corresponds to the nitrate group. In addition, the ^{15}N spectrum consists of doublet peaks with $\left| {}^1J({}^{107,\ 109}Ag^{15}N) \right|$ of ca. 75 and 76 Hz. The ^{15}N chemical shifts are given in Table 6-7. The values of the splittings are confirmed by running the ^{15}N spectrum at 11.7 T. Figure 6-17 (b) displays the ^{15}N CPMAS spectrum obtained at 50.64 MHz with spinning at 6 kHz. The extracted coupling constants from the doublets (ca. 77 and 76 Hz) are in agreement with those obtained from the lower field.
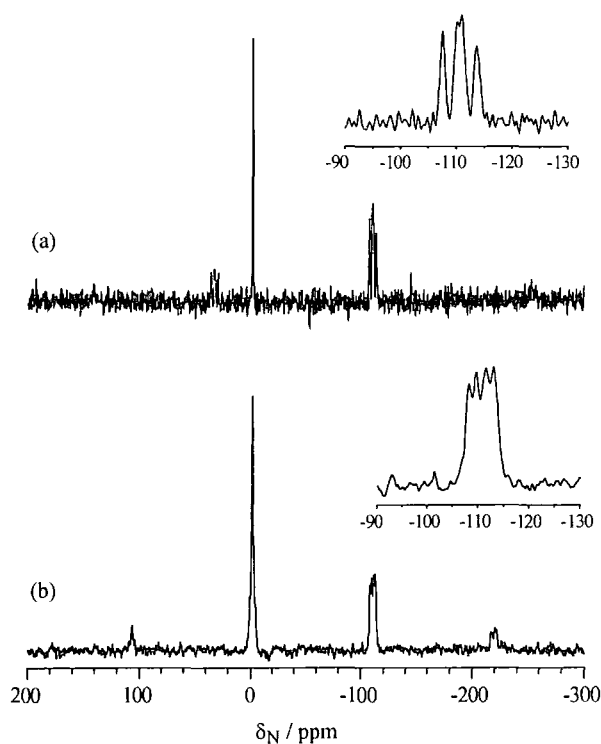
Figure 6-17 Nitrogen-15 CPMAS NMR spectra of [Ag(lut)$_2$]NO$_3$, obtained at: (a) 30.40 MHz with spinning at 4.3 kHz, (b) 50.64 MHz with spinning at 5.5 kHz. Acquisition parameters were: contact time 20 ms, recycle delay 5 s, and number of transients: (a) 15068, (b) 10764.

As can be seen from Figure 6-17 (b), the nitrate peak is quite broad at the base (when compared to this peak at the lower field). This is due to overlapping between the nitrate peak and sidebands of [Ag(lut)$_2$]-cation. This happened because the spin rate was accidentally set to the same value as the spacing between those two groups. Fortunately, this did not have an effect on the splittings (see above).

In addition, a silver-109 CPMAS spectrum was obtained at a spin rate of 6 kHz, as shown in Figure 6-18. At this spin rate, no spinning sidebands could be observed. Only a single symmetrical 1:2:3:2:1 quintet is seen implying that only one type of silver exists in the crystallographic asymmetric unit, which is consistent with the crystal structure.

The splitting of *ca.* 59 Hz in the silver spectrum arises from the one bond coupling between the silver-109 and nitrogen-14 ($I = 1$) and the ratio of $J(^{109}\text{Ag}^{15}\text{N})/J(^{109}\text{Ag}^{14}\text{N})$, $81/59 = 1.38$.
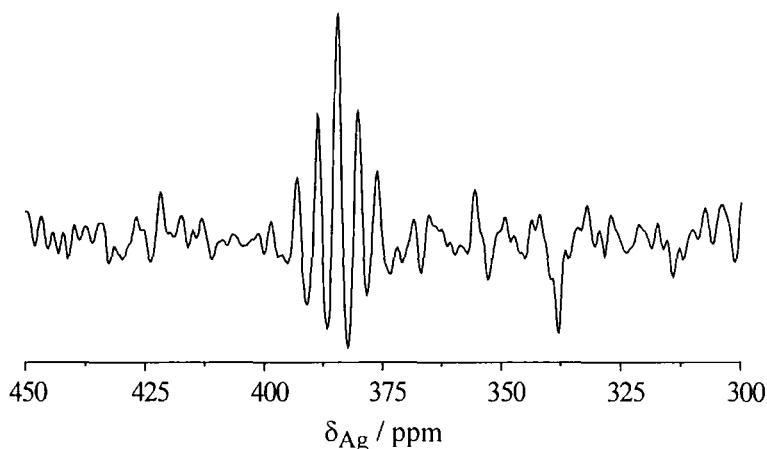
Figure 6-18 Silver-109 CPMAS NMR spectra of [Ag(lut)$_2$]NO$_3$, obtained at 13.97 MHz with spinning at 6 kHz. Acquisition parameters were contact time 20 ms, recycle delay 5 s, and number of transients 468. The 'dips' around the peaks are discussed in section 6.3.1.

It can be concluded that there is one whole group of [Ag(lut)$_2$]NO$_3$ in the asymmetric unit, in agreement with the X-ray data.

Dicollidine silver(I)-nitrate, [Ag(coll)₂]NO₃

The structure of dicollidine silver(I) nitrate is similar to dilutidine silver(I) nitrate, since silver is closely coplanar with the nitrate. X-ray analysis shows it has a water molecule per the asymmetric unit, which hydrogen atoms bond to two oxygen atoms from nitrate (one coordinated and another one not) from the nitrate group. This bonding does not induce asymmetry in the 'chelation' of the nitrate. See also Table 6-5 for other information on the structure.

The ^{13}C spectrum, obtained at 75.43 MHz, for dicollidine silver(I)-nitrate is presented in Figure 6-19. The ^{13}C peak positions and assignments are summarised in Table 6-6.
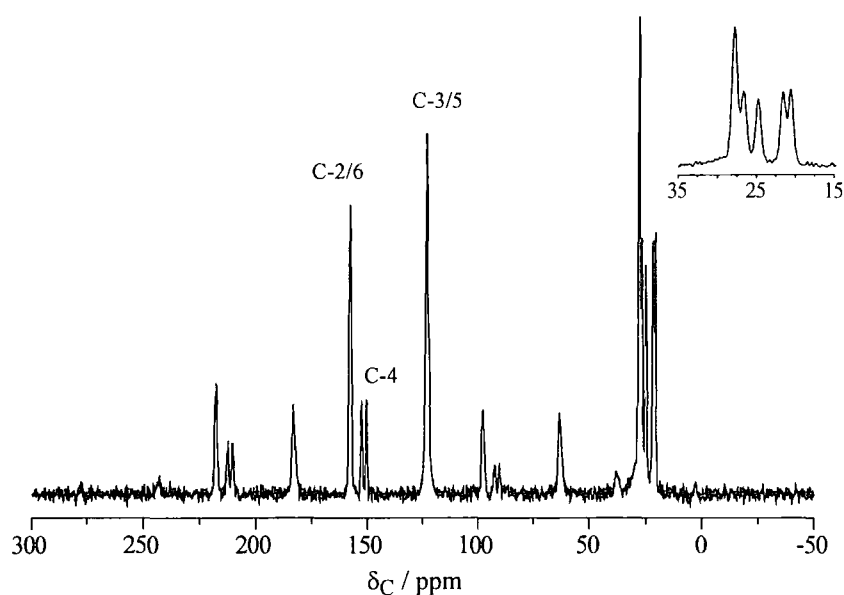
Figure 6-19 Carbon-13 CPMAS NMR spectra of [Ag(coll)₂]NO₃, obtained at 75.43 MHz with spinning at 4.5 kHz. Acquisition parameters were: contact time 1 ms, recycle delay 20 s, and number of transients 60.

Structural information can be deduced from the two lines at C-4 and the signals for the CH$_3$ group. For the latter, there are at least five resonances with the ratio of 2:1:1:1:1 (one peak consists of double intensities from the methyl group at C-4, as displayed on the top right in Figure 6-19). Thus, there should be two whole molecules of collidine in the asymmetric unit, consistent with the structure described above.

Four centreband peaks assigned to the ^{15}N for [Ag(coll)$_2$]-cations, and one peak for the nitrate were observed in the ^{15}N spectra for this compound, as shown in Figure 6-20. At higher field (7.05 T), the Hz separation of the two doublets is increased (see Figure 6-20 (b)), but the J-coupling for each doublet, obviously, remains the same. The $^1J(^{107,109}\text{Ag-}^{15}\text{N})$ splittings obtained at 30.40 MHz, $ca.$ 78 and 74 Hz, are consistent with the values extracted at 50.64 MHz ($ca.$ 79 and 71 Hz.).
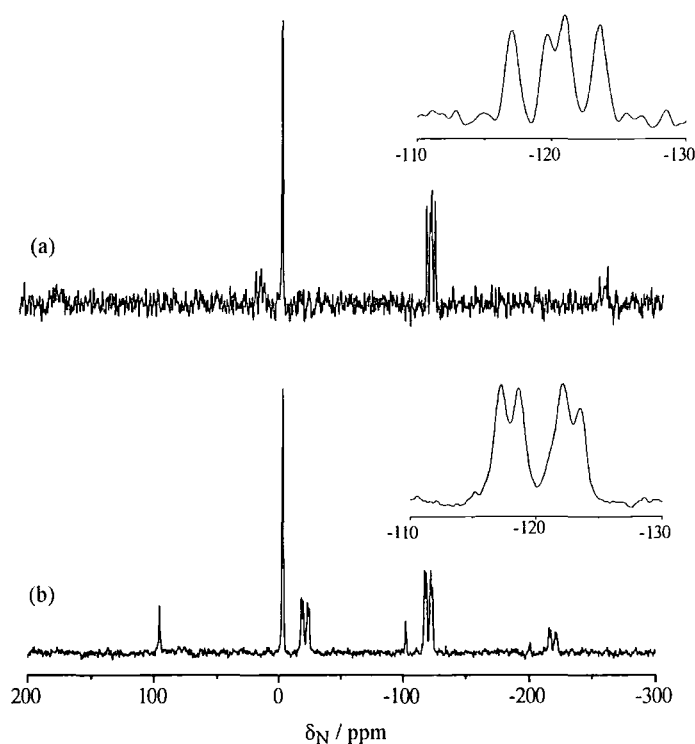

Figure 6-20 Nitrogen-15 CPMAS NMR spectra of [Ag(coll)$_2$]NO$_3$, obtained at: (a) 30.40 Hz with spinning at 4 kHz, (b) 50.64 MHz with spinning at 5 kHz. Acquisition parameters were: contact time 20 ms, recycle delay 15 s, and number of transients: (a) 3660, (b) 3772.

Di(2-picoline) silver(I)-nitrate, [Ag(2-picoline)₂]NO₃

The asymmetric unit consists of one half of a centrosymmetric dimer, one AgNO₃ : two 2-picoline [21]. One oxygen atom of each nitrate group is coordinated with two silver atoms, thus the nucleus of molecule is a planar four-membered ring. The two 2-picoline planes (each coordinated with the same silver atom) have somewhat different dihedral angles to the central ring plane (64.8 (3), 48.9(5)°), hence the two picoline molecules are not equivalent. The N-Ag-N angle of the di(2-picoline) silver(I)-cation is 140.4°, which is less than those of di(pyridine) silver(I)-cation (see Table 6-5).

The isotropic shifts of each ^{13}C signal for [Ag(2-picoline)₂]NO₃ are, as illustrated in Figure 6-21, consistent with the literature [22]. Unlike the other silver(I) complexes, C-2 and C-6 are clearly observed at different positions, as is also true for C-3 and C-5, in conformity with the unsymmetrical nature of the picoline ligand. Moreover, the C-2, C-6 and CH₃ resonance are each clearly split into doublets. One line at 125.6 ppm is assigned to C-3. However, it is unlikely on intensity grounds that there is only one signal for C-3, and in fact a second peak is observed as a shoulder of the C-5 resonance (as shown on top left in Figure 6-21). Clearly, C-3 consists of two peaks at 125.6 and 123.2 ppm (obtained by deconvolution). Thus, it is clear from the carbon-13 spectrum that two whole molecules of 2-picoline exist in the asymmetric unit. The ^{13}C chemical shifts are presented in Table 6-6.
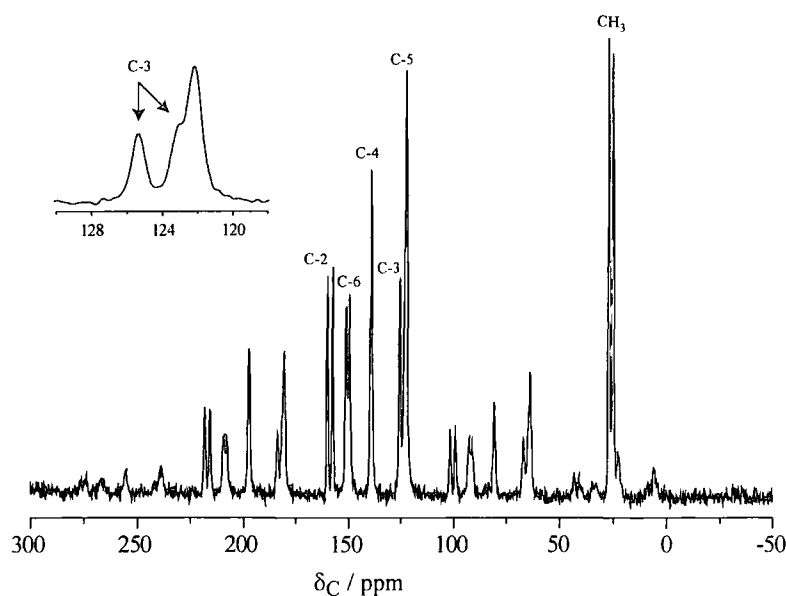
Figure 6-21 Carbon-13 CPMAS NMR spectra of [Ag(2-picoline)₂]NO₃, obtained at 75.43 MHz with spinning at 4.5 kHz. Acquisition parameters were contact time 3 ms, recycle delay 5 s, and number of transients 120.

Figure 6-22 (a) illustrates the ^{15}N CPMAS spectrum obtained at 30.40 MHz. A nitrate peak at -2.95 ppm was observed. There is also, apparently, a 1:2:1 triplet with a spacing of 55 Hz, arising from nitrogen-15 in [Ag(2-picoline)₂]-cation. This unexpected result of a triplet peak was also studied at high field (11.7 T). Unfortunately, those peaks in the ^{15}N spectrum are not well resolved. This "triplet" pattern is likely to arise from accidental near-degeneracies.
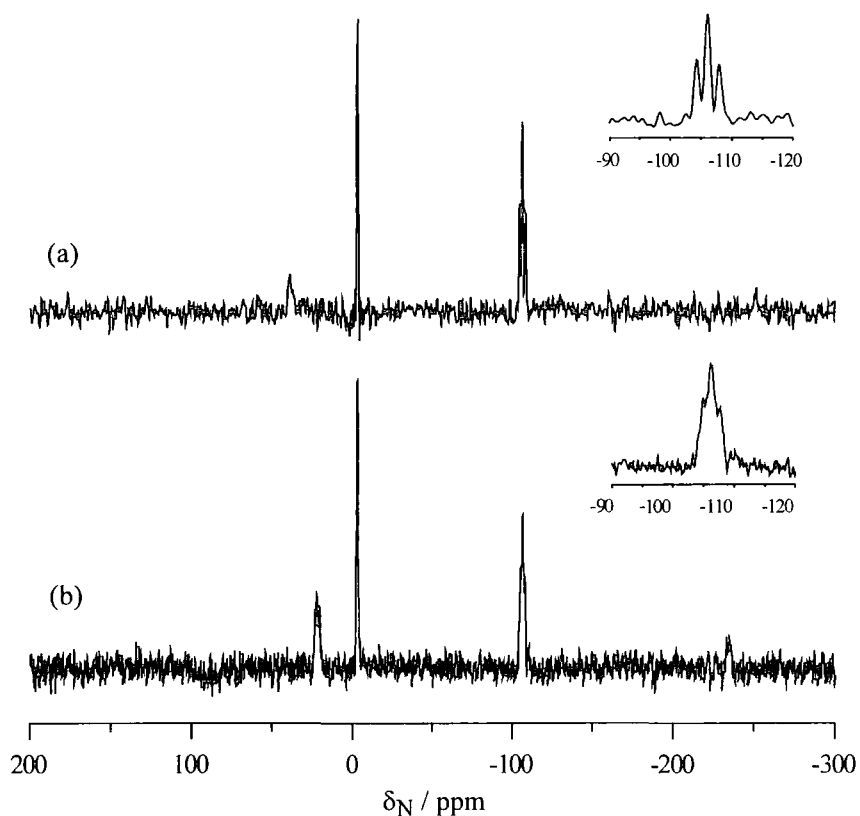
Figure 6-22 Nitrogen-15 CPMAS NMR spectra of [Ag(2-picoline)$_2$]NO$_3$, obtained at 30.40 MHz with spinning at 4.5 kHz, (b) 50.64 MHz with spinning at 6.6 kHz. Acquisition parameters were: contact time 20 ms, recycle delay 5 s, and number of transients (a) 10512, (b) 15408.

Figure 6-23 displays the ^{109}Ag CPMAS spectrum obtained at 13.97 MHz. For this compound the spectrum consists of one symmetrical quintet (1:2:3:2:1) with separations of 46 Hz due to one-bond coupling between ^{14}N and ^{109}Ag.
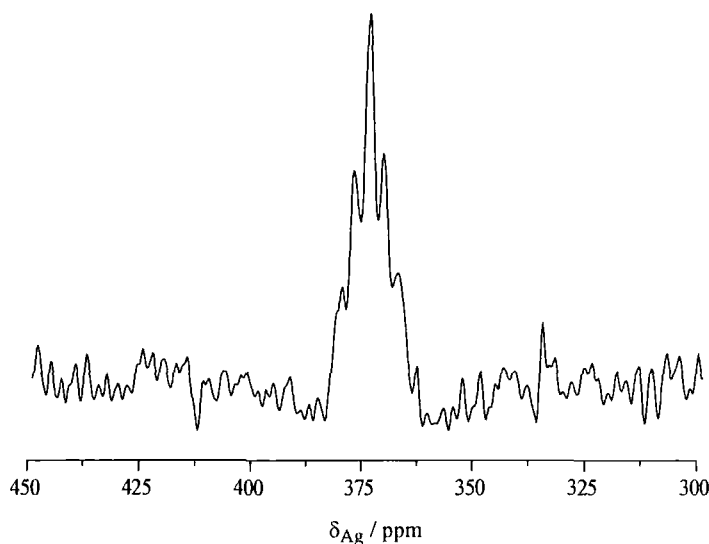
Figure 6-23 Silver-109 CPMAS NMR spectra of [Ag(2-picoline)₂]NO₃, obtained at 13.97 MHz with spinning at 6 kHz. Acquisition parameters were: contact time 8 ms, recycle delay 60 s, and number of transients 1216.

Thus, the NMR results are fully consistent with the structure described above, in which two whole 2-picoline groups, one silver atom and one nitrate group are present in the asymmetric unit.

Diquinoline silver(I)-nitrate, [Ag(quin)₂]NO₃

Diquinoline silver(I)-nitrate crystallizes as a discrete binuclear aggregate incorporating ligands, metal and anions [21]. It has two silver atoms in the asymmetric unit, in which the disposition of the pairs of ligands about two silver atoms differs. Each silver atom, Ag(1) or Ag(2), is bonded by pairs of anionic oxygen. However, this bonding is rather unusual in relation to the other silver(I)-complexes above because the two relevant oxygen atoms are from the same nitrate group rather than from two different nitrogen groups as in the other cases. The distances and bond angles are given in Table 6-5.

The ¹³C spectrum (see Figure 6-24) for this compound is very broad and poorly resolved, so distinction of the chemical shifts of each carbon in the quinoline ligand is difficult. Only the peaks for C-2 and C-9 can be analysed to obtain the chemical shifts, which are found at 154.1 and 145.6 ppm respectively.

Poor crystallinity is unlikely to be the reason for the broad peaks since the powder XRD showed sharp symmetrical peaks implying that this compound is highly crystalline.

The fact that the quinoline ligand contains nine non-equivalent aromatic carbons probably causes substantial overlapping in the spectrum.

Attempts have been made to record the ^{13}C spectrum at higher field to improve the quality of the spectrum in terms of the separations of the peaks. Surprisingly, the spectrum obtained at 125.64 MHz (not shown) provides no resolution improvement. The difficulty in recording the ^{13}C spectrum may be from the compound itself. This, however, cannot be satisfyingly explained at the moment.
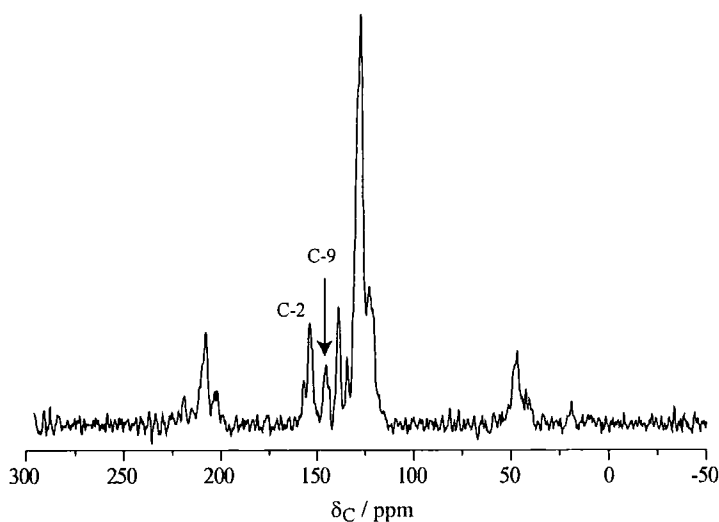

Figure 6-24 Carbon-13 CPMAS NMR spectra of [Ag(quin)$_2$]NO$_3$, obtained at 75.43 MHz with spinning at 6 kHz. Acquisition parameters were: contact time 1 ms, recycle delay 300 s, and number of transients 16.

Figure 6-25 shows the ^{15}N CPMAS spectrum, obtained at 30.40 MHz. The signal-to-noise ratio is very poor even with long recycle delay and many transients (see Figure caption). It also shows somewhat broadened signals (linewidth of *ca.* 77 Hz for nitrate peak compared to those of other silver(I)-nitrate compounds of *ca.* 29 Hz). However, it is still feasible to attribute the peak at -2.8 ppm to the nitrate group, but it is quite difficult to analyse the chemical shifts (by deconvolution) for the signals from the quinoline

ligands (see the expanded region at the top right in Figure 6-25). Moreover, the ^{15}N spectrum obtained at high field (not shown) gave no significant improvement.

A major difficulty for obtaining a good quality ^{15}N spectrum may be related to the very long relaxation time of protons since the ligand is rather rigid (no CH_3 substituents) unlike the other ligands considered (lutidine, collidine and 2-picoline). Also sensitivity of the CP experiment is lower when the number of proton atoms is not much larger than the number of nitrogen atoms (compared with collidine ligand). Consequently, it suggests that the optimum contact time and recycle delay for this compound are significantly long.

Therefore, it is not possible to conclude from the ^{15}N spectra how many nitrogen atoms are in the asymmetric unit.
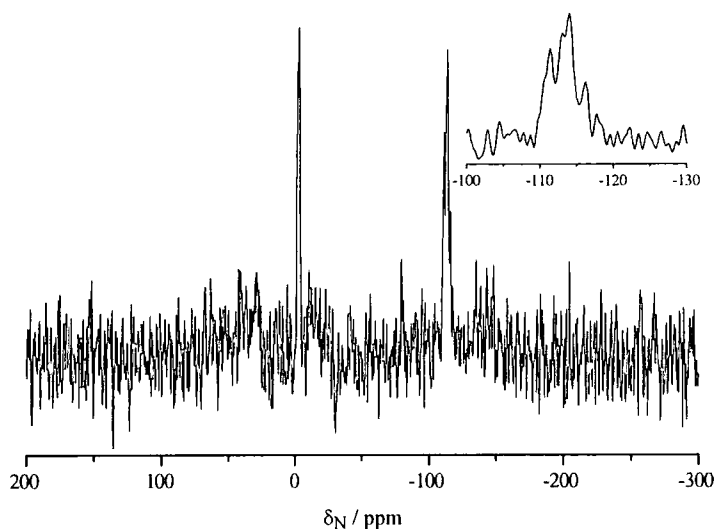

Figure 6-25 Nitrogen-15 CPMAS NMR spectra of [Ag(quin)$_2$]NO$_3$, obtained at 30.40 MHz with spinning at 4.2 kHz. Acquisition parameters were: contact time 20 ms, recycle delay 300 s, and number of transients 268.

As shown above, the ^{15}N chemical shifts for four pyridine-type ligands (pyridine, lutidine, collidine and 2-picoline) are in the range of (-105.4)–(-122.3) ppm. The chemical shifts for each compound are summarised in Table 6-7. These values differ by *ca.* 50 ppm compared to those for the uncomplexed ligands [24]. Similar shifts have been observed in solution-state and solid-state studies [28,29]. This is true of the changed chemical shift of six-membered rings when the nitrogen lone-pair hybridization is changed (the electron lone pair is no longer available).

Comparison of the ^{13}C linewidths

The motivation for this section arises from the variations in the linewidths for C-3,5 and C-2,6 of the systems studied, which all contain pyridine-type ligands, see Figure 6-12. For the purposes of comparison, all the carbon-13 spectra are shown in Figure 6-26 and the linewidths for each carbon resonance are given in Table 6-8. All spectra were obtained using the same probe and proton decoupling field strength (equivalent *ca.* 60 kHz).

The following interesting cases have been found: (1) in [Ag(py)$_2$]NO$_3$, the linewidths for C-3,5, C-2,6 and C-4 are unexpectedly broad and significantly larger than for the other compounds; (2) only the case of 2-picoline shows the expected linewidths, with those of each carbon consistent (*ca.* 72 Hz). The latter spectrum also presents clearly-resolved peaks for C-2 and C-6 (also for C-3 and C-5), in contrast to the spectra of the other compounds.
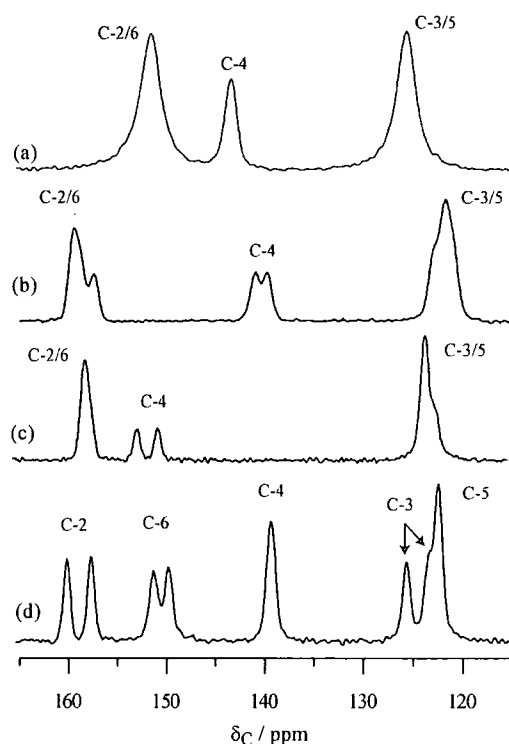
Figure 6-26 Carbon-13 spectra (aromatic regions only) of (a) [Ag(py)$_2$]NO$_3$ (b) [Ag(lut)$_2$]NO$_3$ (c) [Ag(coll)$_2$]NO$_3$ and (d) [Ag(2-pic)$_2$]NO$_3$.

Table 6-8 Carbon-13 linewidths^a in Hz of the silver(I)-nitrate complexes obtained at the 300 MHz spectrometer.

Compound	C-2/6	C-3/5	C-4	CH$_3$		
[Ag(py)$_2$]NO$_3$	180	192	106	-		
[Ag(lut)$_2$]NO$_3$	110, 96^b	149,79^b	82,91	78,68,60,74		
[Ag(coll)$_2$]NO$_3$	89^e	79,80	56,57	80^c,70,68,82,76		

	C-2	C-3	C-4	C-5	C-6	CH$_3$
[Ag(2-pic)$_2$]NO$_3$	61,60	70,64	78^d	70^d	76,82	71,74

^{a} ± 2 Hz.

^{b} linewidths of the shoulder peaks.

^{c,d} the peak has double the intensity of the other CH$_3$ and aromatic carbon peaks respectively.

^{e} the band shows unsymmetrical shape. It, however, is difficult to extract an individual peak by deconvolution.

The case of [Ag(py)$_2$]NO$_3$ will be considered first. The asymmetric unit (obtained from the X-ray study) consists of one whole pyridine ligand, suggesting that C-3 and C-5 (also C-2 and C-6) are non-equivalent. However, there is only one broad peak observed for C-3,5 and for C-2,6. Three possible reasons may result in the linebroadening: (1) the existence of molecular motion (i.e. internal rotation about the C-4 and N distance) may cause averaging of the chemical shifts (e.g. of C-2, and C-6) by the usual exchange process, with measurement being in the coalescence region; (2) the motion may increase the linewidth, via interplay with either the decoupling [30] or MAS [31]; (3) an accidental near degeneracy may cause the two lines for C-3 and C-5 (also C-2 and C-6) to overlap sufficiently so as to be unresolved.

As for cause (2): Waugh and coworkers [30,31] have shown that when $\omega_1 \tau_c \approx 1$ or $\sqrt{2}\omega_r \tau_c \approx 1$ (where ω_1 is the RF field strength for decoupling, ω_r is the MAS frequency and τ_c is the correlation time), i.e. when the time between rotational jumps is comparable to the inverse of the precessional frequency of proton decoupling, ω_1^{-1}, or MAS, ω_r^{-1}, then the effectiveness of proton decoupling or MAS will be reduced, so the resonance lines will become broad.

For the compounds in this section (see Figure 6-12), the aromatic rings may rotate about the axis which runs through C-4 and N, resulting in pair-wise exchange of C-2,6 and C-3,5. It is therefore possible that, at the temperature of the NMR experiment, the rotational rates of the aromatic ring may be in the same region as the precessional frequency of the proton RF-field or MAS, so that proton decoupling or MAS is ineffective, resulting in broadened peaks for both C-2,6 and C-3,5. Therefore, it is of interest to examine the effect of changing the temperature (which will change τ_c) on the line broadening, which will influence all the causes ((1) and (2)) depending on motion. [Ag(py)$_2$]NO$_3$ was studied at low temperature, -25, -50 and -75°C, at a spin rate of 4.5 kHz and an RF field strength of 50 kHz on the 300 MHz spectrometer. Apparently, C-3,5 and C-2,6 are not split to two lines each at low temperature (so cause (1) is unlikely), and the linewidths of ca. 190 Hz are comparable with those at ambient temperature (22°C) (so cause (2) is also unlikely). This result implies that accidental

near-degeneracy of chemical shifts is the most probable reason for broadened peaks of the pyridine complex, though some contribution from the other causes cannot be ruled out.

In the case of C-2,6, a further possibility exists. It is known that if the carbon nucleus is bonded to nitrogen, second-order quadrupolar effects may be transferred to ^{13}C spectra via the dipolar interaction, resulting in a doublet with an intensity ratio of 2:1 [32,33]. This effect may be expected to be observed for the C-2,6 peaks (only) of the pyridine-type ligands. However, 1:1 splitting for C-2,6 in the 2-picoline complex and a 3:1 splitting for C-2,6 in the lutidine complex give clear evidence that there is no observable second-order effect in either complexes. This is presumably explained by a small product of the ^{14}N quadrupolar and the C, N dipolar coupling constant. Thus, the second-order effect is unlikely to be a reason for the broadened lines for C-2,6 of the pyridine and collidine complexes. The band with an intensity ratio of $ca.$ 3:1, which occurs for C-2,6 in the lutidine complex, arises from the nature of the asymmetric unit (4 carbons for C-2,6 from two lutidine ligands), implying that the line-broadening probably arises primarily from peak overlap, with three of the resonances not resolved. The weaker of the two observed peaks is distinctly sharper than the other, which is consistent with the above interpretation.

Additionally, the cause of the line broadening for C-3,5 in collidine and lutidine complexes is probably due to peak overlapping, with intensity ratios $ca.$ of 3:1 and $ca.$ 3.5:0.5 for collidine and lutidine complexes respectively. These ratios are consistent with the carbon atoms in the asymmetric unit (see above).

In addition to above, it is noticeable that even the signal for C-4 of [Ag(py)$_2$]NO$_3$ is somewhat broader than those of C-4 for the other complexes (in each case bonding is to a proton, except in the collidine ligand). This, however, cannot be satisfyingly explained at the moment.

6.4.3   Silver Phosphate Compounds, Ag₃PO₄ and Ag₂HPO₄

Phosphorus-31 and silver-109 NMR spectra for silver(I) phosphate, Ag_3PO_4, and silver(I) hydrogen phosphate, Ag_2HPO_4, are reported in this section.

Silver(I) phosphate, Ag₃PO₄

Silver(I) phosphate has been studied by X-ray crystallography [34,35], and its structure depicted in Figure 6-27. The compound has a cubic lattice space group $P\bar{4}3n$. The structure consists of regular tetrahedra of phosphate ions (PO_4^-) forming a body-centred-cubic (b.c.c) lattice. The P-O distance is 1.539(4) Å. The Ag^+ cations are distributed among twelve sites with twofold symmetry since each Ag^+ occupies one of two possible sites on either side of the ideal site. The distance between these two possible sites is 0.23(1) Å. The Ag^+ is bonded to four oxygen atoms, which are from different phosphate groups (the Ag-O distances are 2.345(3) and 2.403(4) Å), to form an irregular tetrahedron. The O-Ag-O angles are 93.66(7)°, 145.0(5)° and 155.5(5)°. Each oxygen is bonded to three Ag^+-cations.
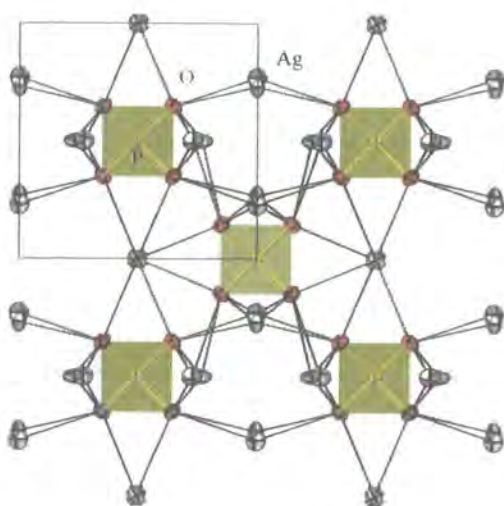

Figure 6-27 Crystal structure of silver(I) phosphate, Ag_3PO_4.

A single-pulse experiment was employed to observe the ^{31}P and ^{109}Ag spectra Figure 6-28 and 6-29 respectively. Very long recycle delays 600 s and 1000 s were used to acquire the ^{31}P and ^{109}Ag respectively. A single resonance at 29.0 ppm with linewidth of *ca.* 20 Hz is found in the ^{31}P spectrum with no observable coupling to ^{109}Ag. This is confirmed from the ^{109}Ag spectrum, which consists of only one peak at 343.2 ppm with linewidth of *ca.* 17 Hz. The NMR results indicate that there is only one type of both phosphorus and silver in the crystallographic asymmetric unit.

The observation of the ^{31}P spectrum with a small CSA (the spinning sidebands for v_r = 5 kHz are very weak) is in agreement with the crystal structure where the ^{31}P is a tetrahedral symmetry (P-O = 1.539(4) Å and O-P-O = 109.47°). No spinning sidebands are observed in the ^{109}Ag spectrum (spin rate of 6.4 kHz). (Note that silver-containing compounds generally have large shielding anisotropies, such as were found in the NMR studies for the silver(I) compounds discussed above.) This is probably due to the position of silver at a tetrahedral site in the solid even though the environment is irregular.
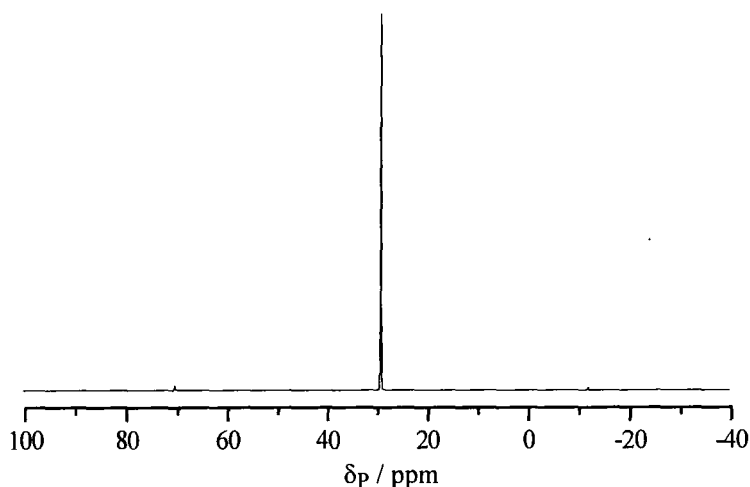

Figure 6-28 Phosphorus-31 spectrum of Ag_3PO_4, obtained at 121.42 MHz with spinning at 5 kHz. Acquisition parameters were: recycle delay 600 s and number of transients 4.
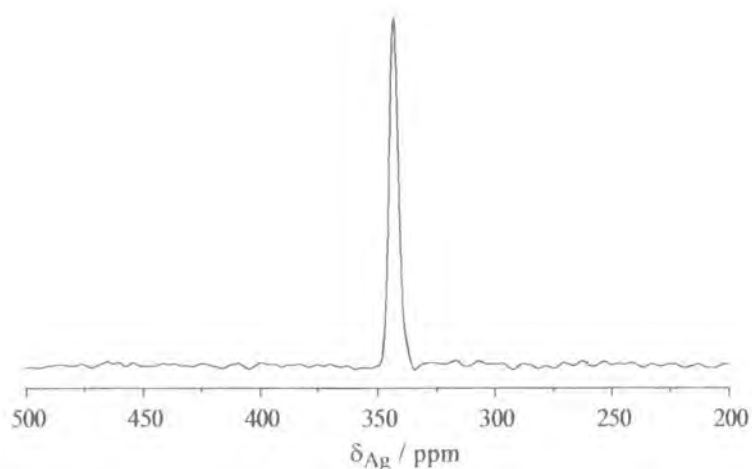
Figure 6-29 Silver-109 spectrum of Ag_3PO_4, obtained at 13.97 MHz with spinning at 6.4 kHz. Acquisition parameters were: recycle delay 1000 s and number of transients 320.

Silver(I) hydrogen phosphate, Ag_2HPO_4

An isolated molecule of Ag_2HPO_4 consists of Ag^+ cations and HPO_4^{2-} anions. The crystal structure of this compound has been reported [36]. It consists of individual PO_4 groups bridged by Ag-Ag pairs and hydrogen bonds, as shown in Figure 6-30.
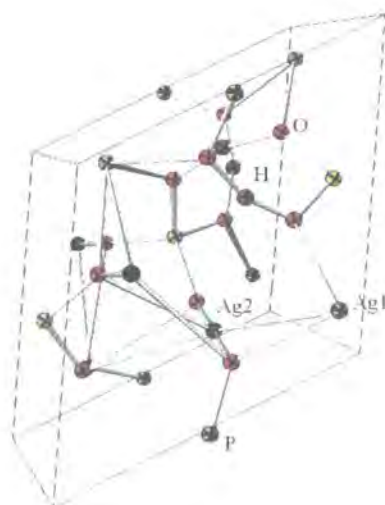

Figure 6-30 The crystal structure of silver(I) hydrogen phosphate.

The proton-decoupled ^{31}P CPMAS NMR spectrum of this compound was obtained at 121.42 MHz. The spectrum shows a single site with an isotropic shift of 15.4 ppm, as shown in Figure 6-31. Spinning sideband analysis was carried out for spectra at different speeds, and the averaged results and the reproducibility are given in Table 6-9. The results suggest that the ^{31}P system has low symmetry. This information correlates well with the findings from X-ray crystallography [36], according to which the PO_4 group has distorted tetragonal symmetry with the P-O(1) and P-O(2) of 1.513 (11) and 1.564 (10) Å respectively; the O(1)-P-O(1), O(1)-P-O(2) , O(2)-P-O(1) and O(2)-P-O(2) angles are 109.4 (5)°, 107.2 (5)°, 111.6 (5)°and 109.5 (5)°, respectively.
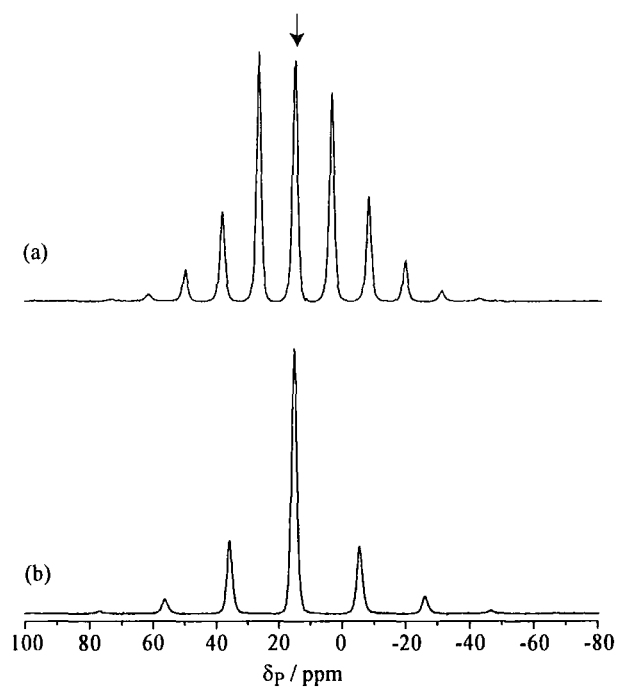

Figure 6-31 Phosphorus-31 CPMAS NMR spectra of Ag_2HPO_4, obtained at 121.42 MHz with spinning at (a) 1.4 kHz (b) 2.5 kHz. Acquisition parameters were: contact time 1 ms, recycle delay 120s, and number of transients (a) 32 (b) 20.

Table 6-9 Results of spinning sideband analyses for ^{31}P for Ag_2HPO_4. The errors quoted are those given on a statistical basis by the SSB97 computer program [17].

Spin rate / kHz	δ /ppm	Linewidth /Hz	$\sigma_{11} - \sigma_{ref}$ /ppm	$\sigma_{22} - \sigma_{ref}$ /ppm	$\sigma_{33} - \sigma_{ref}$ /ppm	$\sigma_{33} - \sigma_{iso}$ ζ /ppm	η
1.4	15.4	235	-46.0 ± 0.5	-16.8 ± 0.1	16.6 ± 0.6	32.0 ± 0.6	0.91 ± 0.01
2.5	15.4	225	-48.0 ± 0.3	-16.7 ± 0.1	18.4 ± 0.1	33.9 ± 0.3	0.92 ± 0.01
average	15.4	230 ± 7	-47.5 ± 0.3	-16.8 ± 0.1	18.3 ± 0.1	33.3 ± 0.3	0.92 ± 0.01

The proton-decoupled ^{109}Ag MAS spectrum (Figure 6-32) shows two peaks, with the same intensity, centred at 296.2 and 146.4 ppm respectively. This reveals that there are two silver sites in the asymmetric unit, in agreement with X-ray diffraction structure.
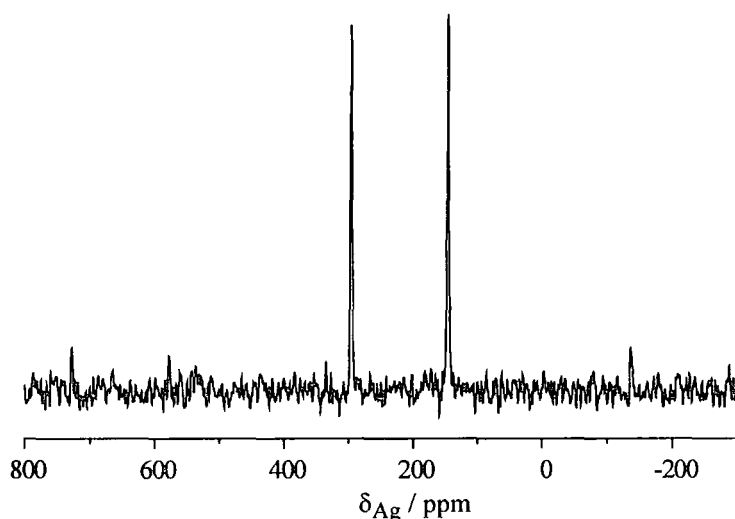

Figure 6-32 Silver-109 spectrum of Ag_2HPO_4, obtained at 13.97 MHz with spinning at 6 kHz. Acquisition parameters were: recycle delay 1000s and number of transients 440.

There is no sign of J coupling between ^{109}Ag and ^{31}P.

6.5 Conclusions

This work has illustrated the application of solid-state ^{109}Ag, ^{15}N and ^{77}Se NMR to the study of three solid diammine silver(I) compounds. Good-quality silver-109 spectra have been obtained and analysed to give shielding tensor parameters. The shielding anisotropy values, ζ, are in the range of 923-1056 ppm. The number of resonances is in agreement with the crystallographic asymmetric units known from diffraction structure results. The one-bond (^{109}Ag, ^{15}N) coupling constants are found to be in the range 64–70 Hz.

The assignment of ^{13}C chemical shifts of pyridine, lutidine, collidine, 2-picoline and quinoline in silver(I) nitrate complexes are straightforwardly obtained. In addition, $|^1J(^{109}\text{Ag}^{15}\text{N})|$ is observed in the range of 59–84 Hz. Information regarding crystallographic asymmetric units has been derived.

Structural information has been also investigated for silver phosphate compounds, Ag_3PO_4 and Ag_2HPO_4. Phosphorus-31 and silver-109 NMR were easy to observe, giving detailed information on the environments of each atom in the molecule, in agreement with X-ray crystal structures.

6.6 References

[1]   H.G. Fijolek, T.A. Oriskovich, A.J. Benesi, P. Gonzlez-Duarte, M.J. Natan, Inorg. Chem. 35 (1996) 797.
[2]   R.K. Harris, E.D. Becker, S.M. Cabral De Menezes, R. Goodfellow, P. Granger, Pure Appl. Chem. 73 (2001) 1795.
[3]   A. Sebald, NMR Basic Principles and Progress 31 (1994) 91.
[4]   M.E. Smith, Ann. Repts. NMR Spectrosc. 43 (2000) 121.
[5]   H.G. Fijolek, J.R. Grohal, J.L. Sample, M.J. Natan, Inorg. Chem. 36 (1997) 622.
[6]   H.G. Fijolek, P. Gonzalez-Duarte, S.H. Park, S.L. Suib, M.J. Natan, Inorg. Chem. 36 (1997) 5299.
[7]   L.H. Merwin, A. Sebald, J. Magn. Reson. 97 (1992) 628.
[8]   S.-I. Nakata, Y. Tanaka, T. Baba, Y. Ono, Stud. Surf. Sci. Catal. 90 (1994) 135.
[9]   T. Ramnial, C.D. Abernethy, M.D. Spicer, I.D. Mckenzie, I.D. Gay, J.A.C. Clyburne, Inorg. Chem. 42 (2003) 1391.
[10]   B.E. Mann, Ann. Repts NMR Spectrosc. 23 (1991) 141.
[11]   G.H. Penner, W. Li, Solid State Nucl. Magn. Reson. 23 (2003) 168.
[12]   U. Zachwieja, H. Jacobs, Z. Anorg. Allg. Chem. 571 (1989) 37.
[13]   U. Zachwieja, H. Jacobs, Z. Krist. 201 (1992) 207.

[14]   G.A. Bowmaker, R.K. Harris, B. Assadollahzadeh, D.C. Apperley, P. Hodgkinson, P. Amornsakchai, Accepted for publication in Mag. Reson. Chem.

[15]   F.A. Bovey, Nuclear Magnetic Resonance Spectroscopy, Academic Press, New York, 1969.

[16]   R.K. Harris, Nuclear Magnetic Resonance Spectroscopy, Pitman, London, 1987.

[17]   J.R. Ascenso, L.H. Merwin, H. Bai, In-house sideband fitting program," University of Durham.

[18]   A.C. Olivieri, J. Magn. Reson. Ser. A. **123** (1996) 207.

[19]   G.A. Bowmaker, R.K. Harris, S.-W. Oh, Coord. Chem. Rev. **167** (1997) 47.

[20]   L.M. Endelhardt, C. Pakawatchai, A.H. White, J. Chem. Soc. Dalton Trans. (1985) 117.

[21]   G.A. Bowmaker, Effendy, K.C. Lim, B.W. Skelton, A.H. White, Currently preparing for publication.

[22]   J.B. Stothers, Carbon-13 NMR Spectroscopy, Academic Press, New York, 1972.

[23]   D.H. Williams, I. Fleming, Spectroscopic Methods in Organic Chemistry, 5th ed., McGraw-Hill, London, 1995.

[24]   S. Berger, S. Braun, H.-O. Kalinowski, NMR Spectroscopy of the Non-metallic Elements, Wiley, New York, 1996.

[25]   E.O. Stejskal, J. Schaefer, J.S. Waugh, J. Magn. Reson. **28** (1977) 105.

[26]   M. Sardashti, G.E. Maciel, J. Magn. Reson. **72** (1987) 467.

[27]   R.A. Wind, S.F. Dec, H. Lock, G.E. Maciel, J. Magn. Reson. **79** (1988) 136.

[28]   J. Mason, *in Encyclopedia of NMR*, D. M. Grant, Ed., Vol. xx, pp 3222, Wiley, London, 1996.

[29]   R.J. Pugmire, *in Encyclopedia of NMR*, D. M. Grant, Ed., Vol. 9, pp 298, Wiley, London, 2002.

[30]   W.P. Rothwell, J.S. Waugh, J. Chem. Phys. **74** (1981) 2721.

[31]   D. Suwelack, W.P. Rothwell, J.S. Waugh, J. Chem. Phys. **74** (1980) 2559.

[32]   A.C. Olivieri, L. Frydman, L.E. Diaz, J. Magn. Reson. **75** (1987) 50.

[33]   R.K. Harris, A.C. Olivieri, Prog. NMR. Spectrosc. **24** (1992) 435.

[34]   L. Helmholz, J. Chem. Phys. **4** (1936) 316.

[35]   H.N. Ng, C. Calvo, R. Faggiani, Acta Cryst. **B34** (1978) 898.

[36]   P.I. Tordjman, A. Boudjada, J.-C. Guitel, R. Masse, Acta Cryst. **B34** (1978) 3723.

CHAPTER 7

RELAXATION MEASUREMENTS IN A COUPLED TWO-SPIN ^{31}P, ^{1}H SYSTEM

7.1 Introduction

In this chapter, measurements of spin-lattice relaxation (T_1) and transverse (spin-spin) relaxation (T_2) times in the sample of tin(II) phosphite (containing relatively isolated ^{31}P, ^{1}H spin pairs) were carried out to fully characterise the NMR behaviour of the system.

It is of interest to study the relaxation in the coupled two-spin ^{31}P, ^{1}H system since the relationship between relevant relaxation parameters has not been analysed in detail previously. Only a few reports [1-4] have appeared on relaxation in coupled two-spin-1/2 systems in solids, and none for the coupled two-spin ^{31}P, ^{1}H system. Ref [1-3] deal with a case of short $T_1{}^C$ (< 1 s). Thus, the intensity of the ^{13}C magnetisation can be easily fitted by single-exponential when the carbon signal is monitored whilst the proton spins remain saturated by the use of a succession of 90° pulses during the recovery time τ. Horsewill [4] *et al.* reported relaxation in solid hexafluoroacetylacetone. Fluorine and proton spin-lattice relaxation times were measured using saturation-recovery. The exponential components obtained from the ^{19}F experiment were consistent with the values from the ^{1}H experiment, in agreement with theory. Noting that the exponential components are 1.5 s and 0.12 s in this system.

7.2   Theory of relaxation in two-spin system

The relaxation dynamics of a coupled spin system have been described by the Solomon equations [5]:

$$\frac{d\langle I_z \rangle}{dt} = -R_I \left[\langle I_z \rangle - I_0 \right] - R_{IS} \left[\langle S_z \rangle - S_0 \right] \qquad (7.1)$$

$$\frac{d\langle S_z \rangle}{dt} = -R_{IS} \left[\langle I_z \rangle - I_0 \right] - R_S \left[\langle S_z \rangle - S_0 \right] \qquad (7.2)$$

where $\langle I_z \rangle$ and $\langle S_z \rangle$ are longitudinal magnetisation of the spin I (^{1}H) and S (^{31}P), respectively; I_0 and S_0 are the equilibrium values of I_Z and S_Z; $R_I = 1/T_1^{II}$; $R_S = 1/T_1^{SS}$ and $R_{IS} = 1/T_1^{IS}$. T_1^{II} is simply the proton T_1 value, and, similarly, T_1^{SS} is the phosphorus T_1 value. T_1^{IS} is the cross-relaxation time between the two coupled spins.

Setting $\left[\langle I_z \rangle - I_0 \right] = x$ and $\left[\langle S_z \rangle - S_0 \right] = y$, these become

$$\frac{dx}{dt} = -R_I x - R_{IS} y \qquad (7.3)$$

$$\frac{dy}{dt} = -R_{IS} x - R_S y \qquad (7.4)$$

The general solution is of the form

$$x = C_1 \exp(-\lambda_1 t) + C_2 \exp(-\lambda_2 t) \qquad (7.5)$$

$$y = C_3 \exp(-\lambda_1 t) + C_4 \exp(-\lambda_2 t) \qquad (7.6)$$

where C_1, C_2, C_3 and C_4 are constants. λ_1 and λ_2 are roots of the characteristic equation.

$$\lambda = \frac{1}{2} \left\{ (R_I + R_S) \pm \left[(R_I - R_S)^2 + 4R_{IS}^2 \right]^{1/2} \right\} \qquad (7.7)$$

It is clearly shown by Equations 7.5 and 7.6 that the time dependences of the z magnetisations are both bi-exponential. Note that it is only in the coefficients C_1 to C_4 that the behaviour of the two nuclides differs. In order to obtain the value of each exponent, the T_1s were studied in the next section.

7.3   Results and Discussions

7.3.1   Spin-lattice relaxation measurement in a coupled two-spin system

As previously shown above, spin-lattice relaxation for a coupled two-spin system will be double exponential. Hence measurement of T_1^X alone would require the decoupling of the other nucleus. Unfortunately this is not feasible when the relaxation times are long, because this would destroy the probe from over-heating.

It should be mentioned that there are two major problems for the T_1 measurement in $SnHPO_3$. One is that the probe used (7.5 mm HX) has a substantial proton background signal. Figure 7-1 shows the results for the proton spectra from $SnHPO_3$ and the empty rotor at a spin rate of 5.2 kHz, obtained with a single pulse experiment. This experiment was done to compare the proton intensities and to obtain the real signal after subtraction. However, an unexpected negative signal is observed after subtracting the background. It is not clear why it is negative since all acquisition parameters and the 90° pulse used to acquire the two spectra were set the same.
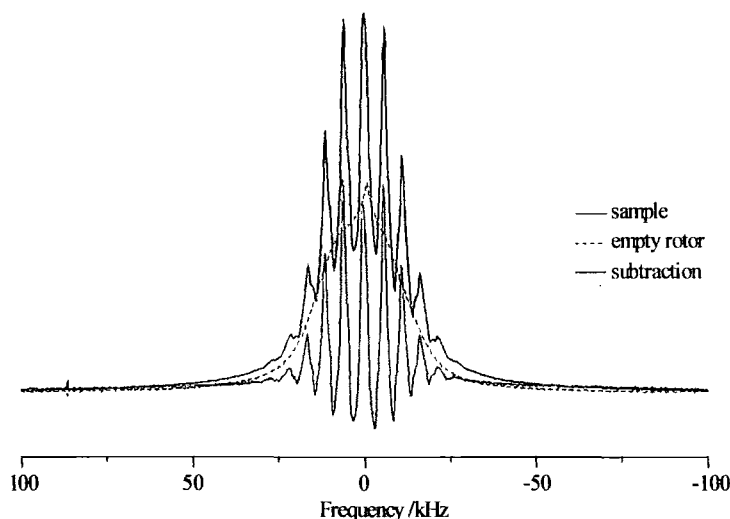
Figure 7-1 Proton spectra at 200.13 MHz obtained with a spin rate of 5.2 kHz. Spectrometer operating conditions: recycle delay is 60 s; the number of transients is 976.

Back linear projection of the initial 12 points of the FID was unable to remove the background signal at a spin rate of 5.2 kHz. Consequently, the direct measurement of $T_1{}^{H}$ for the protons may be difficult.

Another problem arises from the very long times associated with ^{1}H and ^{31}P spin-lattice relaxation. This implies that a long experiment time would be taken if the inversion-recovery pulse sequence, [180° - τ - 90° (FID) - T_d], is used. This is due to the requirement for a long recycle delay, $T_d \approx 5 \times T_1$, to allow full recovery between successive 180° pulses. This pulse sequence is only useful for short T_1's. Fortunately, there is another technique, *saturation recovery*, which can circumvent the problem of the long recycle delay. This sequence consists of a saturation chain of 90° pulses before a recovery time (τ), [(90°)$_n$ - τ - 90° (FID) - T_d]. The series of 90° pulses at the resonance frequency (e.g. proton) will saturate the proton spins, resulting in equal populations of two energy levels, $M_z = 0$. M_z will grow towards M_0 during the recovery time before the next 90° pulse, and the observed NMR signal is proportional to the growth in M_z. The recycle delay can be as short as is consistent with a reasonable duty cycle by the use of this technique.

Figure 7-2 shows the pulse sequences used to obtain T_1's. They consist of a saturation chain of 90° pulses at the proton or phosphorus resonance frequency followed by a variable recovery time. The investigation of T_1^H has been achieved by recording ^{31}P spectra via CP (see Figure 7-2 (a)) whereas T_1^P has been done by observing ^{31}P spectra using direct-polarisation (DP) (see Figure 7-2 (b)). The pulse sequence in Figure 7-2 (a) was used to avoid the background problem.

Note that it in practice was not necessary to have multiple saturation pulses since only one saturation pulse was sufficient to saturate proton (or phosphorus) magnetisations (see below).

(a)

(b)
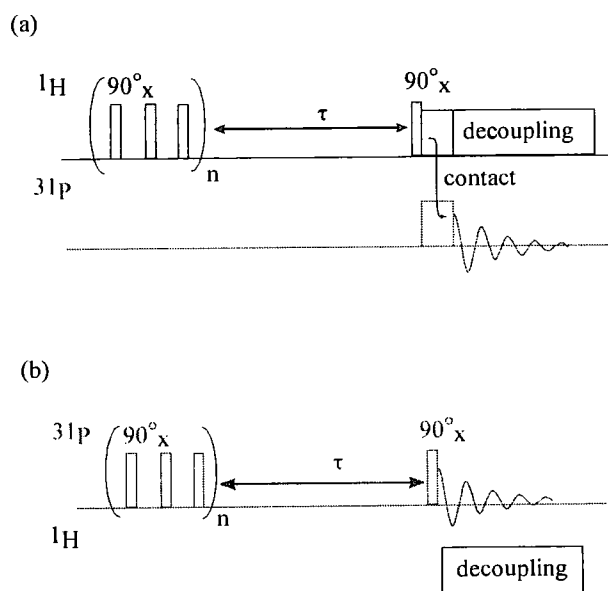
Figure 7-2 Pulse sequence (a) for pre-contact saturation recovery for T_1^H measurement via cross-polarisation and (b) T_1^P measurement via direct-polarisation. The dephasing time between each saturation pulse is 100 μs. n is the number of saturation pulses, set to 100 in this case.

Figure 7-3 shows graphs which plot signal intensity (integrals of the single phosphorus peak) against relaxation delay. The lines are fits to the double exponential functions using Origin. The fitted values are given in Table 7-1. The relaxation time constants (1/λ's) obtained for the two spins are not the same, as would be expected.

(a)

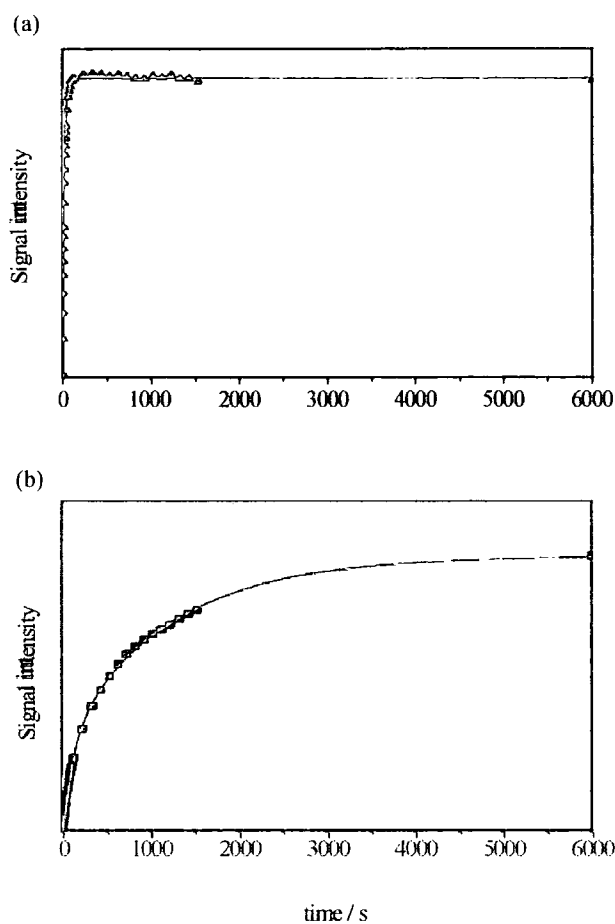
(b)

time / s

Figure 7-3 T_1^H and T_1^P curves from double exponential fits at a spin rate of 5 kHz. The signal intensity was extracted from the use of the pre-contact saturation recovery pulse sequence (see Figure 7-2). Spectrometer operating conditions: (a) contact time 5 ms; (a) and (b) recycle delay 1 s; (a) and (b) number of transients 4.

One possible reason is that the states of the phosphorus and proton magnetisations at the start of the measurement of T_1^H and T_1^P respectively are unknown, i.e. only one spin magnetisation was fixed by implementing saturation pulses (see Figure 7-2). Hence, the sequence was modified to apply saturation pulses to *both* nuclei during the preparation period, cf. Figure 7-4. This ensures that both magnetizations start from a fixed position (saturation).
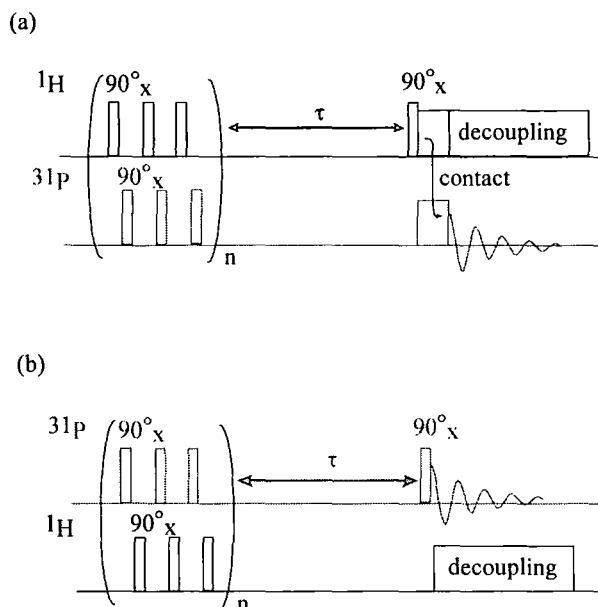
Figure 7-4 Pulse sequences for saturation of both nuclei before the relaxation period. (a) For T_1^H measurement via cross-polarisation. (b) For T_1^P measurement via direct-polarisation. The dephasing time was 50 μs and the number of saturation pulses was set to 100.

The new pulse sequences shown in Figure 7-4 were tested directly on $SnHPO_3$, checking from any effect of the number of saturation pulses on the signal intensity.

Figure 7-5 shows that there is no observable difference in the peak intensities when 100 saturation pulses are used or just one saturation pulse. It implies that no significance of the number of saturation pulses is in the measurement of T_1 in the solid-state because T_2 $<< T_1$, in contrast to the solution-state where the number of the saturation pulses is very important because of $T_2 \sim T_1$. This can be explained by considering the required values of τ compared to T_2; the magnetisations in the xy plane are dephased within only a few tens of milliseconds during the τ period after applying the single saturation 90° pulse.

Figure 7-6 show the signal intensity as a function of relaxation time for two different spin rates. The results of the T_1 measurements are shown in Table 7-2.
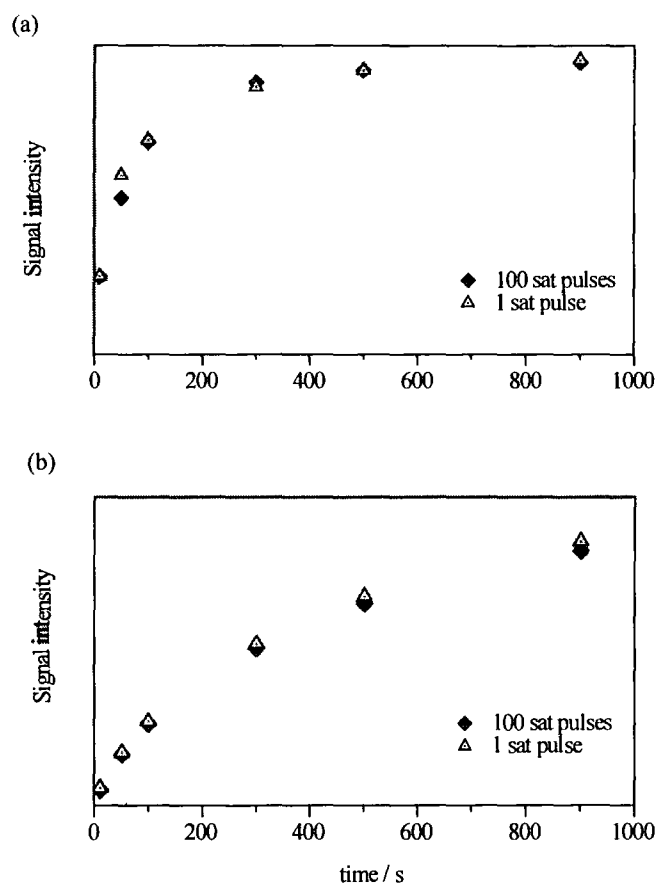
(a)

(b)

Figure 7-5 Comparison of the number of saturation pulses on the signal intensity obtained with spinning at 10 kHz under a fixed dephasing time 50 µs. (a) Using the pulse sequence for T_1^H measurement via CP and (b) using the pulse sequence for T_1^P measurement via DP. Spectrometer operating conditions: (a) contact time 5 ms; (a) and (b) recycle delay 1 s; (a) and (b) number of transients 4.
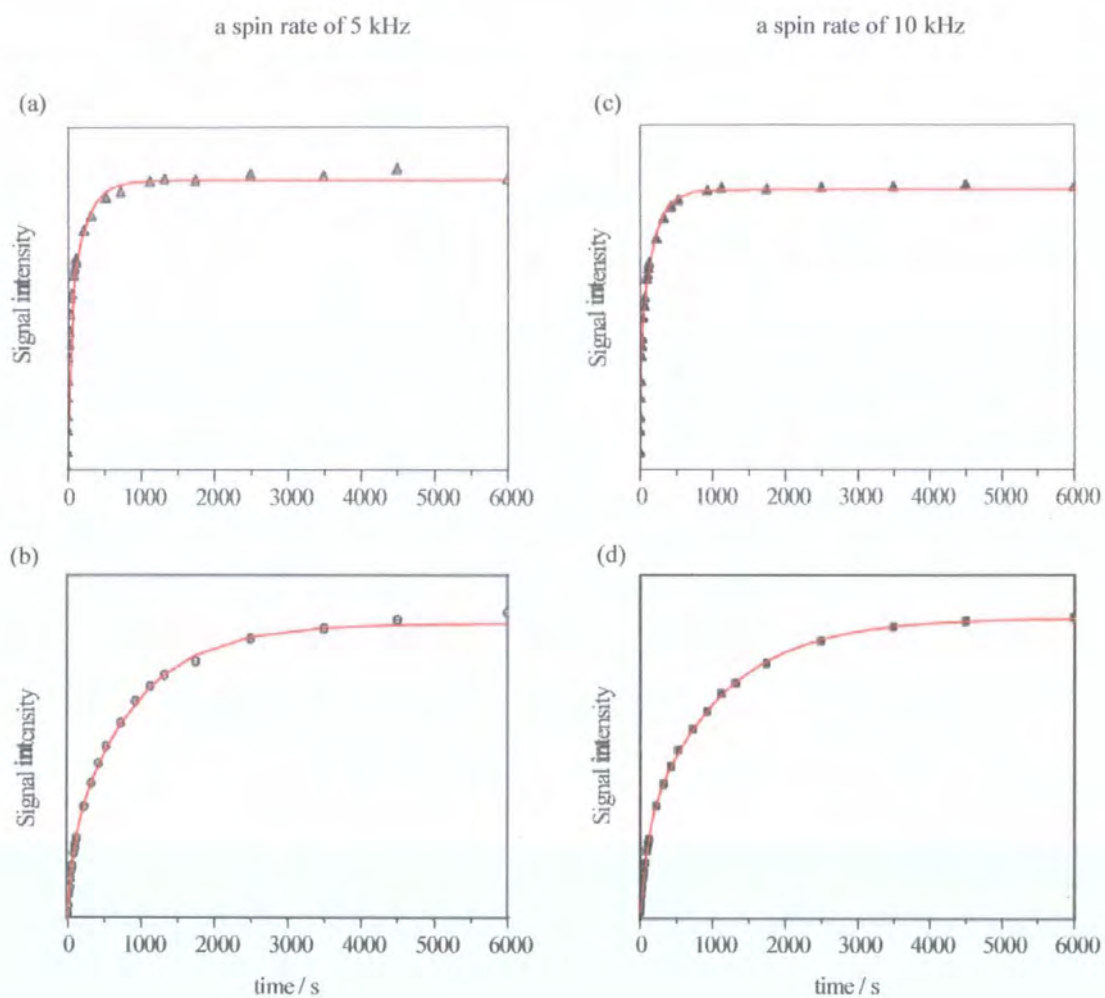
Figure 7-6 T_1^H and T_1^P curves from double exponential fits at two different spin rates: (a), (b) 5 kHz whereas (c), (d) 10 kHz. Spectrometer operating conditions: (a) and (c) contact time 5 ms; (a)-(d) recycle delay 1 s and (a)-(d) number of transients 4.

Table 7-1 [a] Result for $1/\lambda^H$ and $1/\lambda^P$ by pre-contact saturation (proton or phosphorus only) during the preparation period. These experiments were obtained at a spin rate of 5 kHz.

	$1/\lambda^H$		$1/\lambda^P$	
Component	1	2	1	2
Percentage of component / %	61 ± 2	39 ± 2	66 ± 3	34 ± 4
Relaxation time of component / s	24 ± 1	4.0 ± 0.3	1319 ± 137	143 ± 20

[a] This experiment was done on a 7.5 mm probe

Table 7-2 [a] Result for $1/\lambda^H$ and $1/\lambda^P$ by implementing saturation for both nuclei at the same time during the preparation period.

	5 kHz spinning speed				10 kHz spinning speed			
	$1/\lambda^H$		$1/\lambda^P$		$1/\lambda^H$		$1/\lambda^P$	
Component	1	2	1	2	1	2	1	2
Percentage of component / %	55 ± 2	45 ± 3	78 ± 1	22 ± 2	58 ± 2	42 ± 2	75 ± 1	25 ± 1
Relaxation time of component /s	204 ± 20	13 ± 1	885 ± 32	85 ± 8	174 ± 11	11 ± 1	1071 ± 32	103 ± 6

[a] These experiment were carried out on a 4 mm probe.

As shown above, when saturating pulses are applied to both nuclei the results of $1/\lambda$ measurements are improved (the values of $1/\lambda_1^H$ and $1/\lambda_2^H$ are increased and the fits for both $1/\lambda_1^P$ and $1/\lambda_2^P$ are also better than for the simple pre-contact saturation recovery experiment) since the proton and phosphorus magnetisations start from a known-position. However, the results at a spin rate of 5 kHz differ by 10-20% from those obtained at a spin rate of 10 kHz. It is not clear how to explain these results. Furthermore, the $1/\lambda$ values for the two nuclei are consistently different.

7.3.2 Analysis of the effects of relaxation on ^{31}P static spectra

Static ^{31}P spectra from cross-polarisation and direct-polarisation experiments with and without proton decoupling have been recorded on the 200 and 500 MHz spectrometer.

Figure 7-7 shows proton-decoupled ^{31}P CP spectra, recorded using the 7.5 mm probe (Figure 7-7 (a) and (c)) and 4 mm probe (Figure 7-7 (b)). Surprisingly, they show a dip in each spectrum instead of a normal powder pattern. Thus, it is of interest to investigate this anomalous lineshape, and the question of 'which parameters may have an effect on this dip' arises. Two factors, contact time and recycle delay, were taken into account. If the contact time is too short, the CP rate between ^{1}H and ^{31}P will be inefficient and lead to small ^{31}P signal intensity. Also, if a short recycle delay is used, the ^{1}H magnetisation will be saturated and cause CP inefficiency. Both parameters were examined on: (1) different contact times at fixed recycle delays of 120 and 600 s (2) different recycle delays at a fixed contact time of 5 ms using the 4 mm probe. However, they had no effect on the dip. (The results are in the Appendix.)

Since the dip is obviously at about the magic-angle position, the existence of the dip may be due to a dependence of CP rate on molecular orientation; CP will be inefficient if the P-H vector is aligned on the rotor axis, i.e. at the magic angle with respect to B_0.

As shown below, the dip in the spectrum obtained from 4 mm probe is deeper than those from 7.5 mm probe. The differences between the probes are only the amount of the sample and the RF field strength on proton decoupling, but there is no obvious reason why these would influence the lineshape.
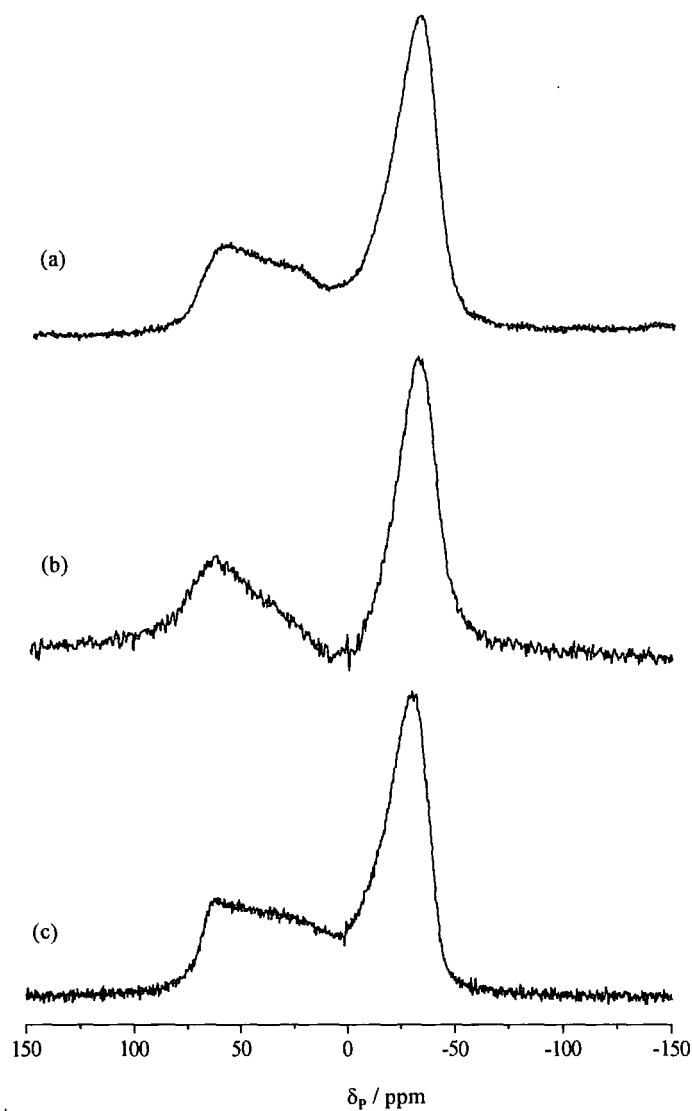
Figure 7-7 Proton-decoupled ^{31}P CP static spectra at (a), (b) 81 MHz and (c) 202.28 MHz, obtained with (a) and (c) a 7.5 mm probe (b) a 4 mm probe. Acquisition parameters were: contact time 5 ms; recycle delay 120 s and number of transients (a) 116 (b) 56 (c) 4. Proton decoupling field strengths were 50 and 83 kHz for 7.5 and 4 mm probes respectively.

Figure 7-8 shows proton-decoupled ^{31}P DP spectra, recorded on the 200 and 500 MHz spectrometers. An anomalous lineshape was observed on the 200 MHz spectrometer (see Figure 7-8 (a) and (b)) whereas a static ^{31}P DP spectrum obtained with the 500 MHz system showed a sensible CSA bandshape (see Figure 7-8(c)). It is not clear why the results from two spectrometers are different. It is also obviously seen that the lineshape distortion is less marked for the 7.5 mm than the 4 mm.

Since the first 200 MHz static spectrum showed an unexpected lineshape, attempts were made on the 200 MHz to examine the possible influences on the ^{31}P static spectrum using the 4 mm probe. Recycle delay and pulse angle were considered. However, increasing the recycle delay had no effect on the lineshape (see Figure 7-9) and also shorter pulse angles did not improve the sensitivity (see Figure 7-10).

[Note that the optimum flip angle ('Ernst angle') α given by:

$$\cos\alpha = \exp\left(-\tau_p / T_1\right) \tag{7.8}$$

where τ_p is the recycle delay, T_1 is assumed to be 1000 s for this study.]

The unusual CSA lineshape may be related to a dependence of relaxation on orientation of the shielding tensor axis in B_0. If this assumption is correct, each site will have different value of relaxation time. Therefore, it is of interest to further investigate on the T_1^P measurement (see the pulse sequence in Figure 7-4). Figure 7-11 shows the lineshape at different recovery times, τ. A comparison of two spectra at the τ of 60 and 600 s, scaling the $\sigma_\perp$ site of the 60 s spectrum to be the same as that of the $\sigma_\perp$ site of 600 s, is shown at the top in Figure 7-11. It is obvious that the relative intensities of the two sites ($\sigma_{//}$ and $\sigma_\perp$) at different times are equal. The intensities at intermediate angle to B_0 also appear to be the same, implying that the relaxation time does not depend significantly on tensor orientation.
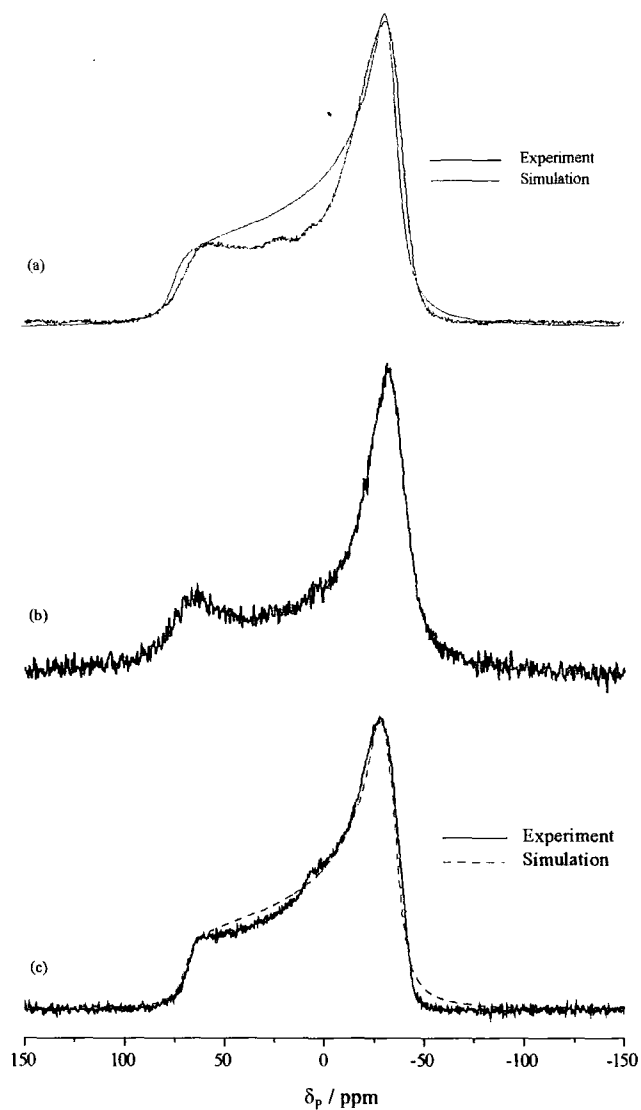
Figure 7-8 Proton-decoupled ^{31}P DP static spectra under proton decoupling at (a), (b) 81 MHz and (c) 202.28 MHz, obtained on (a) and (c) 7.5 mm probe (b) 4 mm probe. Acquisition parameters were: recycle delay 300 s and number of transients (a) 80 (b) 32 (c) 80. (a) and (c) Comparison of the computed-fitted (using STARS) and experimental ^{31}P DP spectra.
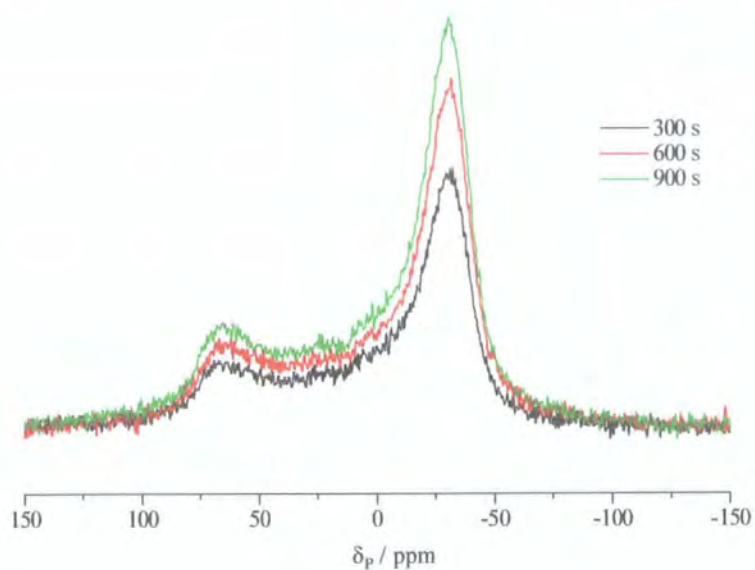
Figure 7-9 Proton-decoupled ^{31}P static spectra at 81.01 MHz for different recycle delays. The number of transients is 32 for each spectrum.
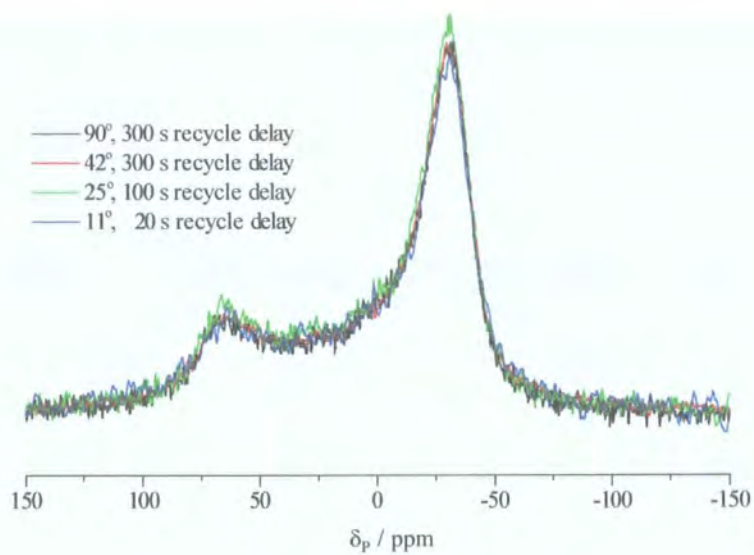
Figure 7-10 Proton-decoupled ^{31}P static spectra at 81.01 MHz for different pulse angles and recycle delays, which were calculated from an estimated recycle delay and T_1^P. The numbers of transients are 32 for recycle delay 300 s, 96 for recycle delay 100 s and 480 for recycle delay 20 s.
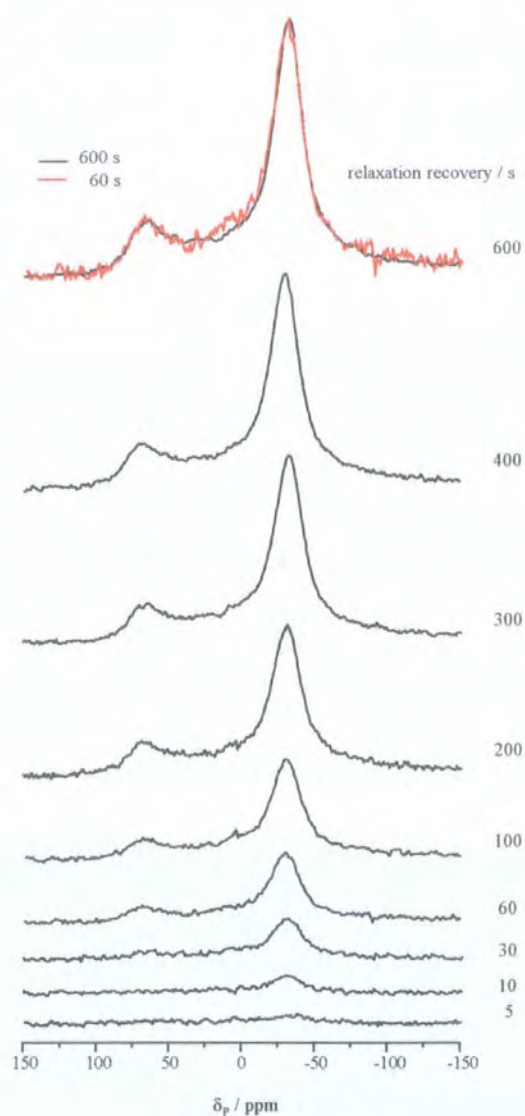
Figure 7-11 ^{31}P DP static spectra at 81.01 MHz under proton decoupling for different recovery times, obtained with the 7.5 mm probe. Each spectrum was obtained with 32 transients. Line broadening of 50 Hz was applied to each spectrum. The top (superimposed) spectra are a comparison of intensities at 60 and 600 s by scaling the 60 s spectrum at particular angle (perpendicular $\sigma_\perp$) to B_0.

7.3.3 ^{31}P spin-spin relaxation measurements

The simple Hahn-echo experiment has been used to measure T_2^P, to determine the true ^{31}P linewidth in $SnHPO_3$. The pulse sequence used is shown in Figure 7-12.
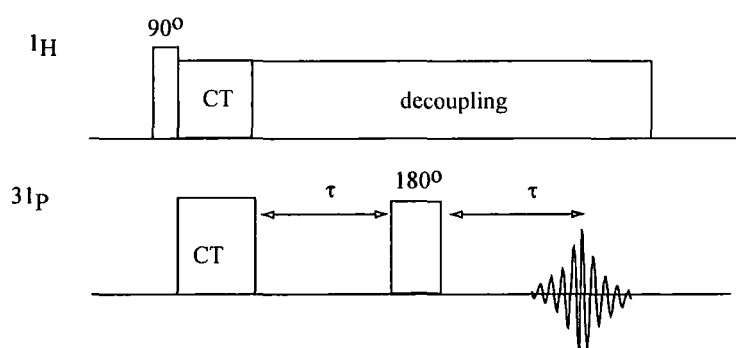
Figure 7-12 Pulse sequence for CP for by a simple Hahn-echo.

The signal intensity decays obtained at each refocusing time (2τ) together with single exponential fits are illustrated in Figure 7-13. The values for T_2^P under the different conditions used (spin rate and decoupling) are shown in Table 7-3. Although the decay at 14 kHz with proton decoupling did not fit well to a single exponential compared to the other results, the T_2^P values are consistent with each other within the errors. The intensities at a spin rate of 14 kHz are less than at a spin rate of 6 kHz due to the inefficiency of cross polarisation at high spin rates.
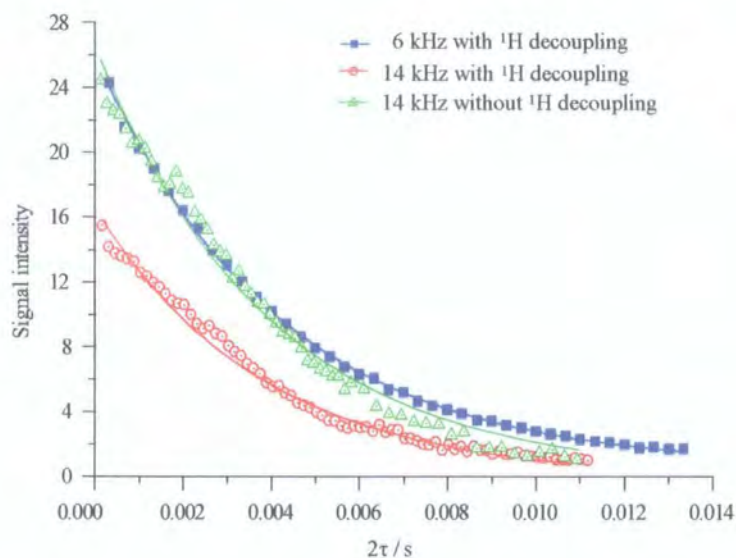
Figure 7-13 T_2^{P} curves using single exponential fits at two different spin rates. Acquisition parameters were: contact time 5 ms and number of transients 4.

Table 7-3 T_2^{P} and linewidth data for SnHPO$_3$ determined using the single Hahn echo pulse sequence.

Spin rate / kHz	T_2^{P} / ms	$\left(1/\pi T_2^{p}\right)/$ Hz	Experimental linewidth^a / Hz
6, with proton decoupling	4.1 ± 0.1	78	157
14, with proton decoupling	4.1 ± 0.2	78	147
14, without proton decoupling	3.9 ± 0.3	81	N/A^b

^{a} estimated error ± 5 Hz.
^{b} experimental linewidth is very broad due to coupling with protons.

The intrinsic ^{31}P linewidths from the proton-decoupled and proton-coupled phosphorus spectra are similar (see Table 7-3). This implies that the heteronuclear dipolar interaction is completely refocused (along with heteronuclear J coupling or chemical shift, i.e. refocusing occurs (see Chapter 2)) by Hahn-echo experiment. This is very different from ^{13}C behaviour in organic samples where the spin-echo does not refocus effects of couplings to the protons. In this case, however, the ^{31}P, ^{1}H spin system is well isolated (on the time scales of the spin-echo experiment) and so spin diffusion among protons is not significant. This presumably allows the heteronuclear interaction to be fully refocused.

7.4 Conclusions

Isolated ^{31}P, ^{1}H spin systems in SnHPO$_3$ present complications for relaxation processes in solid-state NMR. The measurement of T_1 has been investigated and it is found that the exponents for ^{1}H and ^{31}P are different and there is no clear explanation for the relaxation behaviour of SnHPO$_3$ at this stage. One possible reason for the difficulty of this system is a very long T_1^P since spin diffusion may become prominent resulting in an influence on the system.

However, the T_2^P measurement is less complicated than the T_1 measurement because spin diffusion is negligible in this study. The results are straightforward to analyse. It is relatively successful for this investigation, and the intrinsic ^{31}P linewidth is found to be 79 ± 2 Hz.

Unexpected CSA bandshapes have been found in ^{31}P CP and DP static spectra. The anomalies in ^{31}P CP powder pattern may be ascribed to CP inefficiency at magic angle. However there is no obvious reason for the distorted lineshape in the ^{31}P DP powder pattern.

7.5 References

[1]   A. Findlay, R.K. Harris, Magn. Reson. Chem. **28** (1990) S104.

[2]   A. Findlay, R.K. Harris, J. Magn. Reson. **87** (1990) 605.

[3]   J. Zhou, R. Fu, J.Z. Hu, L. Li, C. Ye, Solid State Nucl. Magn. Reson. **7** (1997) 291.

[4]   A.J. Horsewill, I.B.I. Tomash, Solid State Nucl. Magn. Reson. **2** (1993) 61.

[5]   I. Solomon, Phys. Rev. **99** (1955) 559.

CONCLUSIONS AND FURTHER WORK

This work has been important in order to provide information about NMR properties in tin(II)- and silver(I)-containing compounds, i.e. chemical shifts and coupling constants, which have not been extensively studied using solid-state NMR techniques. Valuable information about shielding tensor parameters has been also obtained for ^{119}Sn and (in some cases) ^{31}P for the tin(II)-containing compounds whereas those for ^{109}Ag and ^{31}P in some of silver(I)-containing compounds. Hence, the relationship between NMR parameters and molecular structure (where the crystal structures have been known) has been explored, and new insights have been gained into the structures (in cases with no previously-reported structures).

Isolated (^{31}P,^{1}H) spin pairs in SnHPO$_3$ have been also studied. The system provides both opportunity and difficulty, about which various details have been discussed: the determination of P,H internuclear distances, the measurement of relaxation times and the unexpected behaviour under ^{31}P CW decoupling. The reliability of the P,H internuclear distance has been successfully demonstrated. A better understanding of the complicated behaviour under ^{31}P CW decoupling has been obtained, which relates to the effect of second-order recoupling between the heteronuclear dipolar-coupling tensors and the shielding ^{31}P tensor. Unfortunately, a study of relaxation times did not lead to a good understanding of the behaviour of a coupled two-spin ^{31}P,^{1}H system in SnHPO$_3$ at this stage. The complexity of this system may be related to the very long T_1^P.

In addition to the above, there are several experiments that would be interesting to explore in the further work on the topics included here, as follows:

- Investigate the effect of the CPMG pulse sequence on intrinsic linewidths of ^{119}Sn in SnHPO$_3$ and SnHPO$_4$. This experiment may help to explain the discrepancy between results obtained using Hahn-echo pulse sequence and CPMG pulse sequence.

o   Obtain ^{109}Ag spectra for [Ag(py)$_2$]NO$_3$, [Ag(coll)$_2$]NO$_3$ and [Ag(quin)$_2$]NO$_3$ to report the chemical shifts and also coupling constants.

o   Re-crystallised [Ag(py)$_2$]NO$_3$ and [Ag(quin)$_2$]NO$_3$ to obtain new ^{13}C spectra and then compare their linewidths the other silver(I)-complexes, e.g. [Ag(lut)$_2$]NO$_3$ and [Ag(2-pic)$_2$]NO$_3$. This experiment is worth doing since there is no obvious reason why the linewidths for ^{13}C in [Ag(py)$_2$]NO$_3$ are very broad. It is also desirable to improve the quality of ^{13}C in [Ag(quin)$_2$]NO$_3$ to analyse the chemical shifts.

•   Investigate new decoupling methods to decouple nuclei with large CSAs under magic-angle spinning.

•   Study coupled ^{1}H and ^{31}P spectra in SnHPO$_3$ at higher spin rates (more than 22 kHz) to explore the value of the splitting, since there are discrepancies in the results obtained in this thesis even at a spin rate of 22 kHz.

APPENDIX A

Conferences attended

o   '*15th International Meeting on NMR Spectroscopy*' 8-12 July 2001, Royal Society of Chemistry, University of Durham, UK

●   '*16th European Experimental NMR conference*' 9 – 14 June 2002, Prague, Czech Republic

●   '*The 3rd Alphine Conference on Solid-State NMR*' 14-18 September 2003, Chamonix-Mont Blanc, France

Publications

●   'Solid-state NMR studies of some tin(II) compounds'. Pornsawan Amornsakchai, David C. Apperley, Robin K. Harris, Paul Hodgkinson and Philip C. Waterfield, Accepted for publication in *Solid-State Nuclear Magnetic Resonace*

●   'NMR studies of ^{31}P,^{1}H spin pairs in solid tin(II) phosphite and tin(II) hydrogen phosphate'. Pornsawan Amornsakchai, Paul Hodgkinson and Robin K. Harris, Accepted for publication in *Molecular Physics*

●   'Solid-State ^{109}Ag CPMAS NMR Spectroscopy of some Diammine Silver(I) Complexes'. Graham A. Bowmaker, Robin K. Harris, Behnam Assadollahzadeh, David C. Apperley, Paul Hodgkinson and Pornsawan Amornsakchai, Accepted for publication in *Magnetic Resonance in Chemistry*

Poster presented

⊙ 'Multinuclear Studies of Solid Compounds Containing Tin and Silver'

'*16th European Experimental NMR conference*' 9 – 14 June 2002, Prague, Czech Republic.

⊙ 'Solid-state NMR Studies of Tin(II) Phosphite'

'*The 3rd Alphine Conference on Solid-State NMR*' 14-18 September 2003, Chamonix-Mont Blanc, France

APPENDIX B

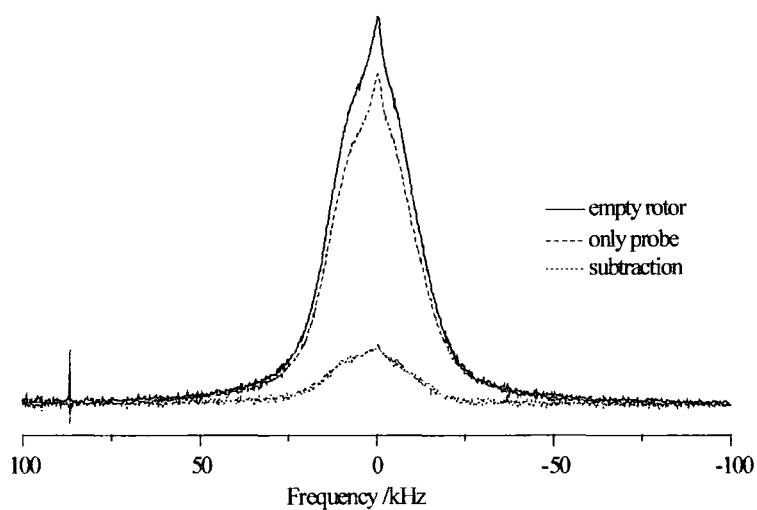## Additional spectra and graphs for Chapter 7

Figure I Proton spectra of a static empty rotor and 7.5 mm probe at 200.13 MHz. Spectrometer operating conditions: The recycle delay is 10 s; the number of transients is 160.
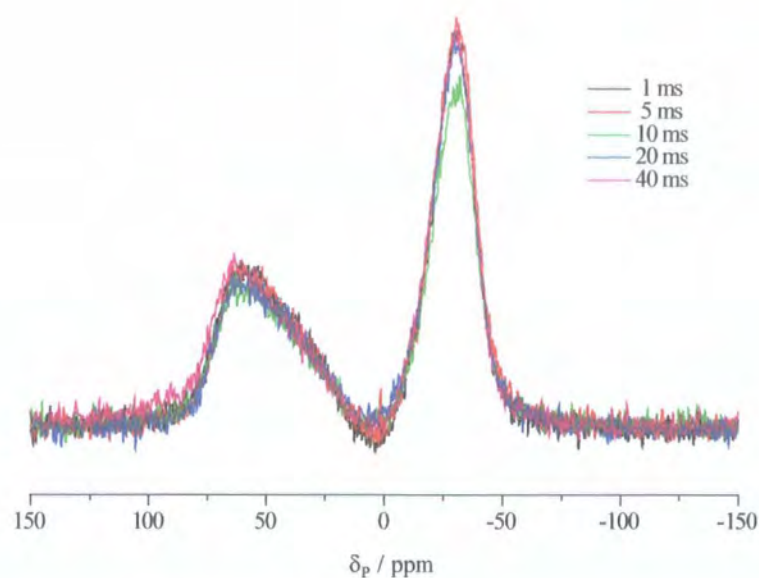
Figure II Proton-decoupled ^{31}P CP spectra at 81.01 MHz for different contact times at fixed recycle delay 120 s. The number of transients is 56 for each spectrum.
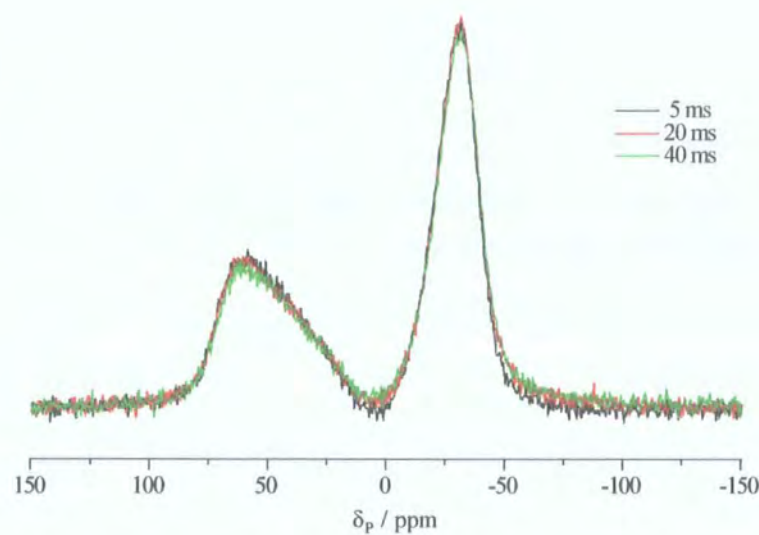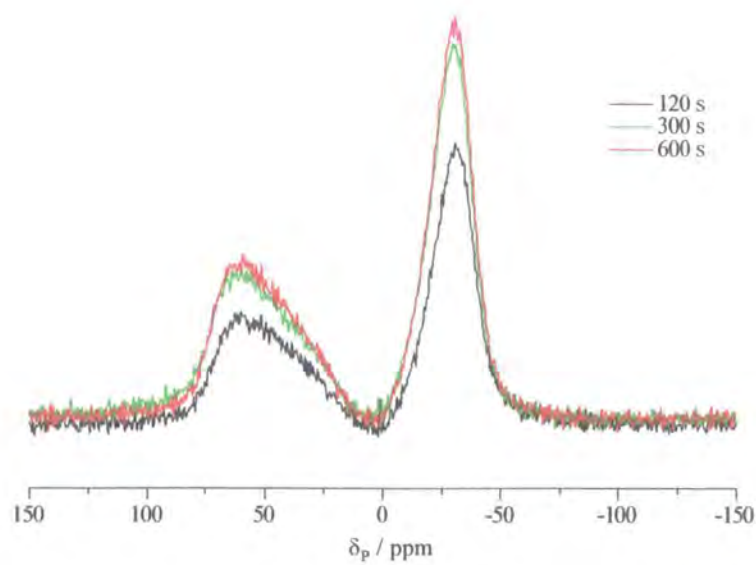

Figure III Proton-decoupled ^{31}P CP spectra at 81.01 MHz for different contact times at fixed recycle delay of 600 s. The number of transients is 32 for each spectrum.

Figure IV Proton-decoupled ^{31}P CP spectra at 81.01 MHz for different recycle delays at a fixed contact time of 5 ms. The number of transients is 56 for each spectrum.

(a)

(b)
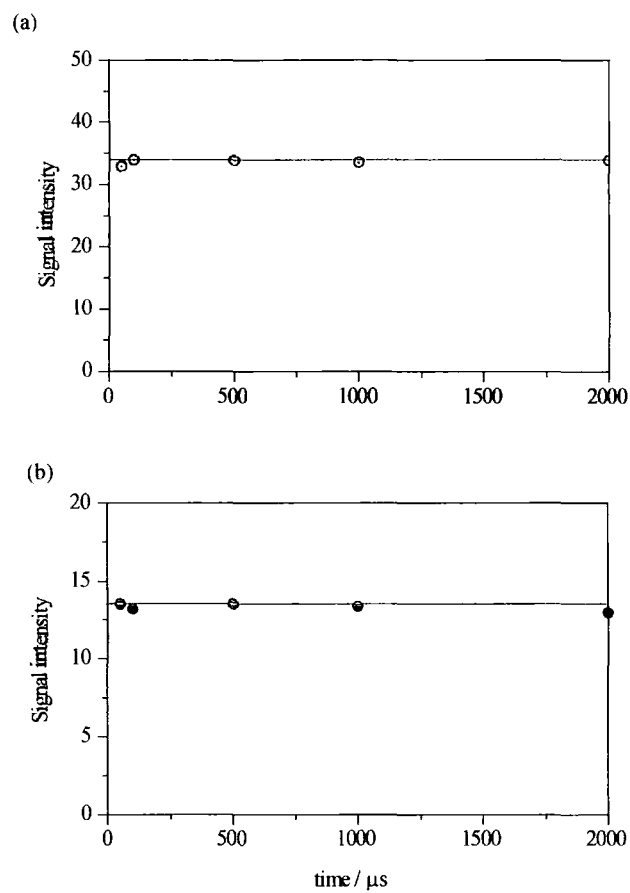
Figure V Comparison of the signal intensity at different dephasing times obtained with spinning at 10 kHz under the fixed number of saturation pulses at 100. The signal intensities are measured on (a) T_1^H via CP (b) T_1^P via DP. Spectrometer operating conditions: (a) contact time 5 ms; (a) and (b) recycle delay 1 s; (a) and (b) number of transients 4.

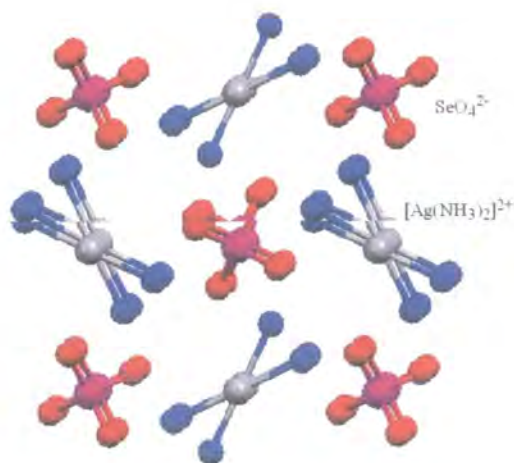# APPENDIX C

Additional crystal structures for Chapter 6

Figure VI Perspective view of the structure of [Ag(NH₃)₂]₂SeO₄ along the *c*-axis. The hydrogen atoms have been omitted for clarity.
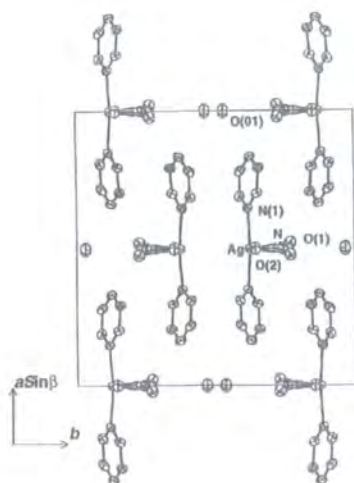

Figure VII Crystal structure of [Ag(py)₂]NO₃
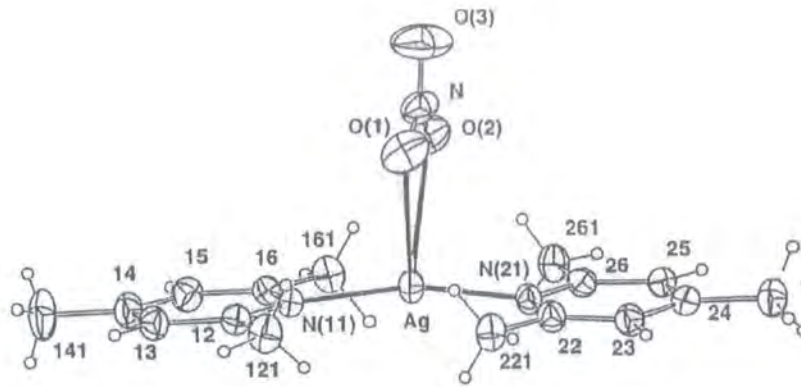
Figure VIII Crystal structure of [Ag(coll)$_2$]NO$_3$
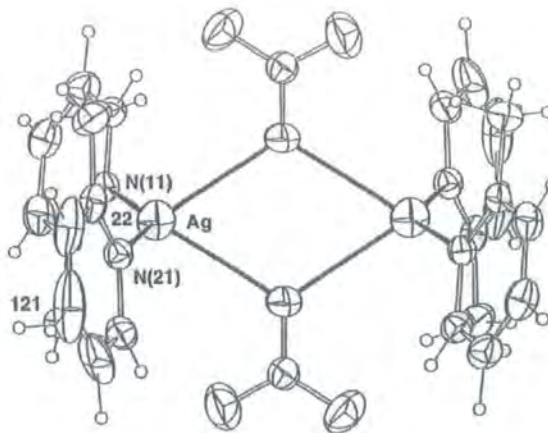
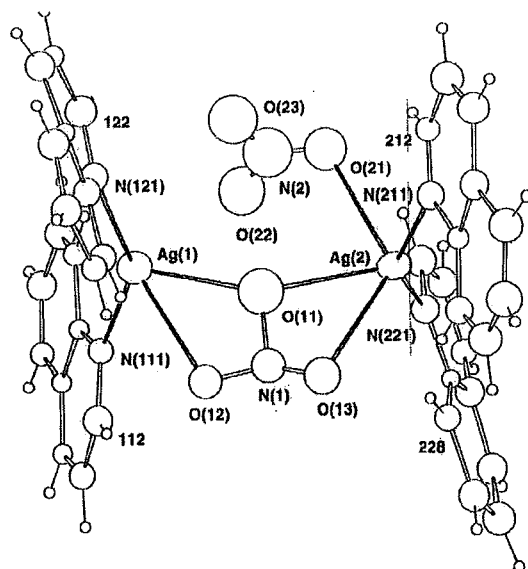**Figure IX** Crystal structure of [Ag(2-pic)$_2$]NO$_3$

Figure X Crystal structure of [Ag(quin)₂]NO₃

APPENDIX D

SIMPSON input file for proton spectrum under CW heteronuclear decoupling

```
# direct polarisation under cw decoupling
spinsys {
   channels 1H  31P
   nuclei    1H  31P
   dipole    1 2  -16800 0 0 0
   shift     1 0  5500 0 0 0 0
   jcoupling 1 2   680 0 0 0 0 0
}

par {
   spin_rate          12000
   gamma_angles       15
   sw                 spin_rate*gamma_angles
   crystal_file       rep168
   np                 2048
   start_operator     I1x
   detect_operator    I1p
   proton_frequency   200e6
   variable rf        80000
   method             gcompute
   verbose            1101
}

proc pulseq {} {
   global par
   maxdt 1
   pulse  1e6 0 0 $par(rf) 0
}

proc main {} {
   global par
   set f [fsimpson]
   faddlb $f 400 0
   fsave $f $par(name).fid
   fzerofill $f [expr 4*$par(np)]
   fft $f
```

```
        fsave $f $par(name).spe
}
```

The simulation was implemented using 168 different crystallite orientations (α_{CR} and

β_{CR}) and 15 equally spaced γ_{CR} angles: where C is a crysatllite-fixed coordinate system

and R is the rotor-fixed coordinate system.

SIMPSON input file for phosphorus static spectrum

```
# Static Direct-Polarization experiment with cw decoupling.
spinsys {
    channels    1H 31P
    nuclei      1H 31P
    dipole      1 2 -16800 0 0 0
    shift       2 0  13890 0 0 0 0
    jcoupling   1 2   680 0 0 0 0 0
}

par {
    spin_rate          0
    gamma_angles       1
    sw                 10000
    crystal_file       zcw232
    np                 512
    start_operator     I2x
    detect_operator    I2p
# proton_frequency     500e6
    method             direct
    verbose            1101
    variable rf        50000
}

proc pulseq {} {
    global par
    reset
    pulse [expr 1e6/$par(sw)] $par(rf) 0 0 0
    store 1
    reset
    acq $par(np) 1
        # maxdt
}
proc main {} {
```

```
    global par
    set f [fsimpson]
    faddlb $f 600 0
    fsave $f $par(name).fid
    fzerofill $f [expr 4*$par(np)]
    fft $f
    fsave $f $par(name).spe
}
```